INFORMATION TO USERS

This manuscript has been reproduced from the microfilm master. UMI films the text directly from the original or copy submitted. Thus, some thesis and dissertation copies are in typewriter face, while others may be from any type of computer printer.

The quality of this reproduction is dependent upon the quality of the copy submitted. Broken or indistinct print, colored or poor quality illustrations and photographs, print bleedthrough, substandard margins, and improper alignment can adversely affect reproduction.

In the unlikely event that the author did not send UMI a complete manuscript and there are missing pages, these will be noted. Also, if unauthorized copyright material had to be removed, a note will indicate the deletion.

Oversize materials (e.g., maps, drawings, charts) are reproduced by sectioning the original, beginning at the upper left-hand corner and continuing from left to right in equal sections with small overlaps. Each original is also photographed in one exposure and is included in reduced form at the back of the book.

Photographs included in the original manuscript have been reproduced xerographically in this copy. Higher quality 6" x 9" black and white photographic prints are available for any photographs or illustrations appearing in this copy for an additional charge. Contact UMI directly to order.

UMI

A Bell & Howell Information Company
300 North Zeeb Road, Ann Arbor MI 48106-1346 USA
313/761-4700 800/521-0600

COMBINED USE OF CLAST-SIZE MEASUREMENTS AND WAVE-TANK EXPERIMENTS TO ESTIMATE PLEISTOCENE TSUNAMI SIZE AT MOLOKAI, HAWAII

by

Andrew Lathrop Moore

A dissertation submitted in partial fulfillment of the requirements for the degree of

Doctor of Philosophy

University of Washington

1999

Approved by _____
Chairperson of Supervisory Committee

Program Authorized to Offer Degree GEOLOGICAL SCIENCES

Date 4 MARCH 1999

Doctoral Dissertation

In presenting this dissertation in partial fulfillment of the requirements for the Doctoral degree at the University of Washington, I agree that the Library shall make its copies freely available for inspection. I further agree that extensive copying of this dissertation is allowable only for scholarly purposes, consistent with "fair use" as prescribed in the U.S. Copyright Law. Requests for copying or reproduction of this dissertation may be referred to University Microfilms, 1490 Eisenhower Place, P.O. Box 975, Ann Arbor, MI 48106, to whom the author has granted "the right to reproduce and sell (a) copies of the manuscript in microform and/or (b) printed copies of the manuscript made from microform."

Signature 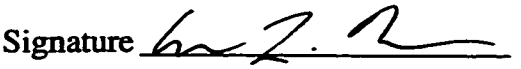

Date 3 March 1999

University of Washington

Abstract

Combined use of clast-size measurements and wave-tank experiments to estimate Pleistocene tsunami size at Molokai, Hawaii

by Andrew Lathrop Moore

Chairperson of the Supervisory Committee: Affiliate Professor Brian F. Atwater
Department of Geological Sciences

Wave-tank experiments allow the size of a Pleistocene tsunami to be estimated from its deposits on the south coast of Molokai. The tsunami, approaching the shore as a turbulent bore, may have been close to 20 m high and probably was no more than 75 m high.

The deposit, which rests on basalt bedrock, alluvium, and soil, consists mainly of basalt boulders but also contains carbonate pebbles and cobbles derived from coral reefs. It extends along 7 km of coastline, as much as 2 km inland, and up to 72 m above present sea level. Carbonate clasts in the conglomerate get smaller with elevation and distance from shore, whereas basalt clasts display no vertical or lateral trend in size. The abundance of carbonate clasts also decreases with elevation. Only a tsunami could have moved large grains as much as 2 km inland, and produced the simple trends in carbonate clasts while imparting no size trend to basalt. The likely age of the tsunami, from previous U-Th and ESR dating, is 100,000-200,000 years B.P.

I measured the movement of particles in turbulent bores, these being close approximations of shallow-water tsunamis. Using a 15-m wave tank with a dam-break gate, I sent the bores onto a 1:10 slope holding cube-shaped particles. I measured advection lengths for eight bore heights, five particle sizes, and four particle densities. The data plot as a linear trend on the non-dimensional axes L/h and w/u, where L is advection length, h is bore height, w is particle settling velocity, and u is depth-averaged velocity within the bore. Inclusion of a first-order approximation of Stoker's (1948) analysis of bore velocity yields an expression for bore height as a function of bore velocity and depth of water into which the bore travels. This relationship allows for estimation of bore height from particles moved by ancient tsunamis.

Because the advection length term (L/h) for the Molokai deposit is almost 100 times larger than the settling velocity term (w/u), estimates of the Molokai bore height depend almost entirely on advection length. I obtained the 75-m height by assuming advection from a full-glacial shoreline 125 m below present sea level, and the 20-m height by assuming advection from an interglacial shoreline near the present one.

TABLE OF CONTENTS

LIST OF FIGURES

LIST OF TABLES

LIST OF SYMBOLS

A particle cross-sectional area

C_D drag coefficient

C_M inertia coefficient

c_0 speed of a shallow water wave in water of depth h_0

D intermediate grain diameter

D_i diameter of the grain size for which i% of a population is finer

d flow depth

f friction factor

F_d drag force

Fr Froude number

F_w submerged weight of a particle

g acceleration of gravity

h bore height

h_0 depth of still water into which bore travels

k_s height of roughness elements

L average advection length

L_r inundation distance

P Rouse number $\left(=\frac{w}{\kappa u_*}\right)$

R runup height

Re	Reynolds number
S	slope
t	time
u	depth-averaged velocity
$\dot{u}$	acceleration $\left(=\frac{\mathrm{d}u}{\mathrm{d}t}\right)$
u_*	shear velocity $\left(=\sqrt{\frac{\tau_0}{\rho}}\right)$
V	particle volume
w	particle settling velocity
α	constant multiplier on f (Chapter 2)
β	exponent on f (Chapter 2)
Φ_i	diameter, in phi units $(\Phi=-\log_2 D)$, of the grain size for which i% of a population is finer
κ	von Karman's constant (=0.408)
μ	fluid kinematic viscosity
ν	fluid dynamic viscosity $\left(=\frac{\mu}{\rho}\right)$
ρ	fluid density
ρ_s	particle density
σ_i	inclusive graphic standard deviation (Folk, 1974)
τ_0	bottom shear stress

τ_* dimensionless shear stress

$\dot{\xi}$ bore propagation speed

ACKNOWLEDGMENTS

Brian Atwater, Jody Bourgeois, Catherine Petroff, and Dave McTigue served as committee members; Jody Deming and Ann Nelson were its graduate faculty representatives.

Harry Yeh, Bruce Nelson, and Steve Porter reviewed parts of this dissertation. Eric Cheney helped me keep perspective.

Dave Lewis and Simon Snell helped as field assistants on Molokai. Tracy Drury, Erik Shjarback, and Belqies Jalalyar helped as lab assistants in the wave tank. Tony McKay helped me instrument the wave tank, and Dick Terry let me help build it. I especially thank Halldór Árnason for helping me build the wave tank, run the experiments, and understand the results.

No acknowledgments would be complete without thanks to all of my officemates in Harris and the Barn who have been my family for as long as I can remember.

INTRODUCTION

The ability to recognize the gravelly deposits of tsunamis and to use them in estimating the tsunami's size would be an important step in establishing tsunami history for gravel-rich shorelines such as fringing reefs. To date, however, the study of gravelly debris has been limited to using its maximum elevation to establish inundation limits for a particular tsunami (Moore *et al.*, 1994; Makino, 1977). This dissertation shows that gravel can yield additional information on the size and source of the tsunami that deposited it.

As an example I use a conglomerate on the south coast of Molokai, Hawaii, that Moore *et al.* (1994) interpreted as the deposit of a tsunami. Well exposed and extensive, the deposit may be well described. Many particles in the deposit are clearly marine in origin, making estimates of their provenance possible. An objection raised by critics of Moore *et al.* (1994) is that the wave required to produce the Molokai conglomerate is too large to have been produced by the landslides Moore *et al.* claim as the source for the wave (Johnson and Mader, 1994). This conclusion is based, however, on equating the conglomerate's maximum elevation with the original height of the wave. In this dissertation, I propose a method by which grain-size data from the deposit can be used to estimate the size of the wave.

APPROACH

It is difficult to relate the effects of a tsunami to the size of its waves. Runup, the maximum height above sea level that a tsunami reaches, is probably the most collected field measurement following a tsunami. The extensive use of runup data is probably because of the relative ease of data collection and the widespread use of runup to produce coastal inundation maps for hazard planning. However, it is difficult to relate tsunami runup to wave height or velocity because the numeric simulations required involve some of the more difficult aspects of computer simulation, including moving boundary conditions, wave breaking, and movement onto a dry bed. The dependence of runup on local variations in roughness (such as vegetation and topography) also complicates computer simulations, because data on these local variations must be accurately transferred to the model. The use of runup measurements is also problematic because a few data points may describe a large area. The maximum height water reaches can also be affected by local topography not accounted for in computer models, resulting in anomalously high or low runups.

Problems with using runup to deduce wave parameters get worse for prehistoric tsunamis. Many commonly used runup indicators—salt crusts, wrack lines, dead vegetation—rarely survive in geologic records. Other indicators, such as stripped soil, are not unique to tsunamis. Even those indicators which might be preserved and which are commonly associated with tsunamis, such as sand sheets, rarely extend to the maximum

level of inundation and can be eroded after deposition, complicating runup determination. Lastly, information on local variations in vegetation and topography is often not preserved.

Several geologists have used grain-size data from tsunami-laid sand sheets to estimate the size of ancient tsunamis (Moore and Mohrig, 1994; Moore, 1994; Reinhart, 1991). Their methods have several advantages over runup-based research. First, the use of grain-size trends averages out small-scale fluctuations, yielding a more general measurement than runup indicators, which provide data for only a single point. Grain-size trends can also provide evidence for post-depositional erosion and can help differentiate the direction and size of multiple waves in a tsunami. Methods based on grain size can also yield estimates of flow velocity, flow depth, and in some cases, wave period.

One drawback to adapting sand sheet methods to the study of gravelly tsunami debris is that all of the methods used previously hinge on an understanding of the behavior of particles in a flow. Understanding of cobble and boulder movement is still less than that for sand. A second problem is that it has been difficult to compare results for ancient tsunamis against those for modern events. Grain size and density data are available for only a few modern deposits (Minoura *et al.*, 1997; Moore *et al.*, 1996; Nishimura and Miyagi, 1995; Shi *et al.*, 1995). Even in these cases, the flow velocity of the waves is generally unknown.

A partial solution to problems in characterizing natural tsunamis is to use data from tsunamis simulated in wave tanks rather than from field waves. Tank waves can be heavily instrumented, allowing for precise data on flow depth and flow velocity to be collected. The use of scaled boulders in the flow allows for information on the behavior of large objects in tsunamis to be studied. Waves of varying size can be produced as needed, allowing for calibration across a wide range of tsunamis. The shoreline topography can be simplified, minimizing focusing and diffusion from local effects and giving the results a more general applicability to natural waves.

Such an approach has its disadvantages, however. The use of experimental data, while providing a general model for simple slopes, bed roughnesses, particles, and waves, cannot reproduce the particular conditions (such as irregular topography and variations in bed roughness due to vegetation or geology, and the behavior of groups of particles rather than single particles) that existed during any given tsunami. These parameters may also vary with time as the tsunami alters both topography and bed roughness. Lastly, natural tsunamis occur as a series of waves, sometimes striking the coast from more than one direction. Such complexity is hard to model in a wave tank.

EXPERIMENTS

The experiments were designed as a first attempt at describing how tsunamis might sort gravelly sediment. I chose to simplify or make constant several factors that

may have a significant effect on sorting, but which couldn't be altered with the experimental setup I devised.

PARTICLE SHAPE AND COMPOSITION

For all experiments, I chose to use cubes or orthogonal shapes. These particles have sharp edges to serve as detachment points for the wake, as do natural particles, making them a better choice than spheres. A simple geometry also allows parameters like the cross-sectional area in the direction of flow to be estimated. A disadvantage to using cubes, however, is that the particles have a large surface area in contact with the bottom, possibly increasing the force required to move the particle initially; it also makes the particles prone to slide.

Most of the particles were made of aluminum. Aluminum is cheap, easily machined, and has a density (2.71 g/cm^3) similar to that of silicate rock. To extend the range of particle weights available and to decouple density from grain size, I used several other materials—acrylic, lignum vitae, and magnesium. Acrylic (1.12 g/cm^3) and magnesium (1.78 g/cm^3) were chosen to cover as broad a range of densities as possible while using only those materials easily machined with available facilities. Lignum vitae (1.56 g/cm^3) was added later to fill a gap in the data between acrylic and magnesium.

To investigate the role of shape and orientation, I also performed a series of experiments not reported in this dissertation using orthogonal shapes in different

orientations. These particles have the same advantages as cubes—sharp edges and simple geometry—but the same disadvantages as well. Future experiments should investigate the effect natural particles (with a known density and shape) have on the results.

SUBMERGENCE

I chose to place the particles at the waterline in an attempt to simulate particles on a beach. The amount of water over each particle also affects advection length, however. I performed some experiments, not reported here, on the effect of particle submergence on advection length—it is an important parameter and will need more investigation.

SLOPE AND BED ROUGHNESS

Slope and bed roughness were kept constant. Although both of these factors are probably important to gravel sorting by tsunamis, I chose only a slope applicable to the Molokai case, and a general bed roughness. The effect of both of these parameters should be investigated. I chose cubes for the model particles, and made most of them from aluminum.

MULTIPLE WAVES AND WAVE RUNDOWN

A tsunami is not a single wave, but rather a series of many waves. Although a tsunami deposit is the result of all the waves in a tsunami, I chose to investigate the results of only one wave. The experimental setup did not allow for more than one wave to

be produced, nor could it account for how each particle might act during the rundown of the wave. Particles in a natural tsunami deposit may run down with the return flow, or may remain fixed, buried within the deposit. The particles in the experiments usually traveled down slope with the flow, often wedging between the beach and the side wall. Because this effect was artificial, I chose to consider the advection length to be the longest distance moved by the particle rather than its terminal resting place.

Wave tank experiments cannot reproduce natural tsunamis, nor are they intended to. Wave tank experiments can provide some insight into the factors that affect gravel sorting by tsunamis, however, and their relative importance. The experiments described in this dissertation are a first attempt at quantifying the process of particle sorting by bores, keeping many factors constant and constraining others to approximate the situation on Molokai. To make these results more general, and to include more factors, further experiments on the effect of slope, bed roughness, and particle type will be required.

CHAPTER 1: LANDWARD FINING IN A SUSPECTED TSUNAMI DEPOSIT ON MOLOKAI, HAWAII

INTRODUCTION

Coral-bearing deposits up to 72 m above sea level on the south coast of Molokai (herein called the Molokai conglomerate) have been ascribed to a series of Pleistocene marine highstands (Stearns, 1978; Lum, 1972; Jones, 1993; Grigg and Jones, 1997) and to a tsunami caused by a catastrophic submarine landslide to the southeast about 240 ka (J.G. Moore *et al.*, 1994). Grain size trends within the deposit may help to distinguish between these contrasting interpretations. A single tsunami should produce landward fining, as noted in onshore sandy deposits of some modern tsunamis (Bourgeois and Reinhart, 1989; Shi *et al.*, 1995; Nishimura and Miyaji, 1995; Minoura *et al.*, 1997). The deposits of several marine highstands, by contrast, are likely to produce a more complex pattern, with separate grain size populations from each highstand. Similarly, compositional trends within the deposit should be simpler for a single tsunami than for reworked multiple marine terraces.

In this paper I describe simple grain size and compositional trends in the Molokai conglomerate which point to a tsunami as the simpler explanation.

GEOLOGIC SETTING

The island of Molokai (Figure 1a) is composed principally of two basaltic shields, the older West Molokai Volcano (youngest lavas dated to 1.52 Ma by Naughton *et al.*, 1980) and the younger East Molokai Volcano (youngest lavas dated to 1.35 Ma by McDougall, 1964). A third volcano, Kalaupapa, formed long after the main shield building phase of the two main shields had ended (youngest lavas dated to 340 ka by Clague *et al.*, 1982). Both volcanoes are truncated on the north, forming some of the highest sea cliffs in the world. To the south, however, slopes are moderate (6° to 15°), and are especially gentle (as little as 2° to 3°) where East Molokai lavas ponded against West Molokai (Macdonald *et al.*, 1990).

LATE QUATERNARY UPLIFT

The origin of the Molokai conglomerate depends on its history of uplift. By some accounts, the Molokai conglomerate accumulated within a few vertical meters of the shore; it represents the deposits of several shorelines formed through the interaction of land-level changes on Molokai and eustacy. Alternatively, Molokai has been tectonically stable for hundreds of thousands of years, and subsided before that, so that the height of the Molokai conglomerate must be due to great waves.

The inference of uplift began with Stearns (1978), who identified two emerged shoreline deposits on Molokai, at 65 m and 170 m. Although he did not date the deposits, Stearns felt that the deposits were associated with a combination of changes in Pleistocene eustatic sea level and land level changes on Molokai itself. This idea is

supported by a model whereby lithospheric flexure associated with the hotspot under Hawaii produced approximately 50 m of uplift on Molokai in the past 250 ka (Watts and ten Brink, 1989). Grigg and Jones (1997) interpreted the Molokai conglomerate as shoreline and storm deposits elevated by such uplift. Their evidence includes a trend of increasing electron-spin resonance age with elevation in the deposit (Figure 2). They did not include, however, uranium-thorium age data of J.G. Moore *et al.* (1994), which destroy the trend.

Evidence for a tectonically stable Molokai comes from Kalaupapa, a small volcano on the north coast of Molokai (Figure 1b). Although the shoreline of Kalaupapa during shield building is now 50 meters below sea level, lava tubes on the exposed flanks of the volcano show no evidence that they have ever been submerged (J.G. Moore, 1987). From this negative evidence Moore (1987) inferred that Molokai had been tectonically stable since the eruption of Kalaupapa, 340 to 570 ka. Moreover, J.G. Moore and Campbell (1987) determined the age of the end of subsidence for several Hawaiian islands by dating the youngest drowned reef for each island studied. They concluded that subsidence ceased on Lanai, an island younger than Molokai, by 320 ka. Because eustatic sea level has probably been no more than about 5 meters above present sea level since 400 ka (Hearty and Kindler, 1995), marine conglomerates tens of meters above present day sea level cannot be associated with marine highstands if Molokai is tectonically stable.

DEPOSIT ARCHITECTURE AND AGE

The Molokai conglomerate mantles the southwest flank of East Molokai and extends onto the saddle between the two shields (Figure 1b). Though most commonly exposed in shallow (2-3 meter deep) drainages, the deposit can be found in outcrop and as float on surrounding hillsides to a maximum of 72 m above present-day sea level along about 7 km of the south coast of Molokai (Figure 1c). The deposit generally tapers landward from a maximum thickness of 3 m. It typically lacks bedding or grading, although J.G. Moore *et al.* (1994) noted indistinct bedding and imbrication at a few of the sites they studied.

The Molokai conglomerate has yielded a range of ages (Figure 2) most consistent with deposition of the conglomerate between 200,000 and 100,000 years ago. J.G. Moore *et al.* (1994) estimated the deposit to be 240,000 years old, based on U-Th dating of corals found in the deposit. More recent dating by Grigg and Jones (1997) shows that the deposit is composed of corals with different ages, although none dated is younger than ~130,000 years old (Figure 3). Because the deposit must be younger than the corals it contains, the maximum age can be estimated from the -2σ age of the youngest dated coral, in this case, about 200,000 ka. No corals are present from the stage 5 highstand (Figure 3), although stage 5 deposits are common in the Hawaiian islands (Jones, 1993). This suggests that the Molokai conglomerate was deposited before stage 5, which ended about 100,000 years ago.

COMPOSITION

At the most shoreward sites the conglomerate is almost entirely carbonate (Figure 4d). The deposit becomes progressively more basaltic with distance from shore (Figure 4a-c). The carbonate within the deposit consists primarily of branching coral and coralline algae, with gastropod shells, echinoid spines, and carbonate mud rip-up clasts present locally. Basalt clasts, which range from angular to subrounded, show no preferred orientation other than localized imbrication. The clasts are surrounded by sandy lime mud cemented with equant calcite grains typical of vadose cement. The degree and type of cement appear constant throughout the deposit.

PARTICLE SIZE

METHODS

I measured particle size in the boulder conglomerate at 34 sites (Figure 1c) selected for exposure size and quality. At each exposure, grain size was measured on a 10 cm by 10 cm grid, following the method of Kellerhals and Bray (1971). This method produces histograms of numbers of particles in each size fraction, with results equivalent to sieving by weight (given a uniform density for basalt and for carbonate, respectively). Each site was measured until 100 carbonate grains were recorded or until no more outcrop could be found. Each grain's composition was noted and its visible long and short axes were recorded to the nearest millimeter (Appendix A). I excluded grains smaller than 1 mm on the long axis.

In most cases cementation prevented me from observing the actual axes; I measured only the visible axes, which can result in underestimation of grain size. In thin sections, apparent long and intermediate axes closely approximate the actual intermediate and short axes, respectively (Kellerhals *et al.*, 1975). Because any outcrop surface can be considered a roughly planar cut through the deposit, I used the apparent long axis as roughly equal to the actual intermediate axis (and hence the particle diameter, D) for the Molokai conglomerate.

For each location, I separated grains into size classes based on their apparent long axis, from –10 Φ to 0 Φ in ½-Φ intervals ($\Phi = -\log_2 D$, where D is the grain diameter in millimeters). As with sieving, grains at size-class boundaries were assigned to the larger size class (for example, a 16 mm grain was assigned to the –4 Φ class, not to the –3.5 Φ class). I then divided the number of grains in each bin by the total number of grains to produce a fractional grain size curve. From the corresponding cumulative grain size curve, I determined median grain size and graphical standard deviation, σ_i (Folk, 1974), where:

$$\sigma_i = \frac{\Phi_{16} - \Phi_{84}}{4} + \frac{\Phi_5 - \Phi_{95}}{6.6} \qquad (1)$$

I used this standard deviation to determine standard error.

RESULTS

The grain-size distribution for a single grain type (carbonate or basalt) at each site is roughly log-normal (Figure 5). Because log-normal distributions are typical of natural sediments (*e.g.*, Folk, 1974), the method of Kellerhals and Bray (1971) is appropriate for the Molokai conglomerate. Log-normal distributions also allow for the estimation of parameters, such as standard deviation, that require a normal distribution. Commonly, however, basalt is coarser than the carbonate (Figure 5), making the combined distribution bimodal.

Median grain-size data of the apparent long axes from the 34 sites show no grain-size trend for basalt (Figure 6a) but overall landward fining for carbonate (Figure 6b). Although the carbonate data are somewhat scattered, data from within a single stream valley (dark squares, Figs. 1b, 4d, 6a and 6b) show less variability than for the entire area.

INFERENCES ABOUT DEPOSITION

The Molokai conglomerate is best explained as the deposit of a single tsunami. Tsunami deposits commonly show landward fining (Minoura *et al.*, 1996; Atwater and Moore, 1992; Dawson *et al.*, 1990), although there are cases where no landward fining has occurred (Moore *et al.*, 1996). No such landward fining has been reported for marine terraces, and storm deposits commonly show no grain size trends (Leatherman *et al.*, 1977). When coupled with the fact that the deposit is unique within at least the last

250,000 years on Molokai, and stretches inland farther than any modern storm deposit in Hawaii, tsunami becomes the most likely explanation for the deposit.

Landward fining occurs in many tsunami deposits because the grains are commonly carried in suspension from a restricted source (a source of distinctive material available from a nearby erodible location, for example a beach, dune, tidal channel, or tide flat). As the flow decelerates or crosses non-erodible surfaces (like vegetated tidal marshes), particles fall to the bed, the larger particles closer to the source because they have higher settling velocities and thus spend less time in transit. Particles moved in suspension from a restricted source should display landward fining if the Molokai deposit were to have been produced by a tsunami. However, if the deposit formed from two or more emerged shorelines, there should be a fining trend associated with each shoreline.

Sorting occurs only in carbonate clasts on Molokai because only they have a restricted source. On Molokai, carbonate grains come from the fringing reef or the beach, whereas basalt clasts are ubiquitous offshore, on beaches, and throughout uplands. Because their source is not restricted, basalt clasts should show no grain-size trend if a tsunami were to have created the Molokai deposit. The presence of a simple trend in carbonate clast sizes also argues against the presence of substantial, high-elevation marine terraces on Molokai. If terraces were present, their grains would combine with those from the modern beach, creating landward fining trends from each terrace rather than a single trend.

Simple calculations show that the carbonate clasts were carried in suspension. If the largest basalt clast (apparent long axis=710 mm) measured in the deposit was just moving, and if the critical dimensionless shear stress (τ_*) was 0.6, the shear velocity (u_*) of the flow would be 2.8 m/s. Given this shear velocity and the settling velocity of the largest measured carbonate (apparent long axis=220 mm), the largest carbonate has a Rouse number of 1.02, where Rouse number is defined as:

$$P = \frac{w}{\kappa u_*} \qquad (2)$$

(P is Rouse number, w is particle settling velocity, κ is von Karman's constant, and u_* is shear velocity). Full suspension occurs at Rouse numbers less than about 0.8, indicating that most carbonate grains in the deposit moved primarily as suspended load.

SUMMARY

The coral-bearing conglomerate on the south coast of Molokai displays simple trends in grain size and composition consistent with deposition in a single event and inconsistent with an origin as multiple marine terraces. The observation that age increases with elevation reported by Grigg and Jones (1997) is not apparent when the age data reported by Moore *et al.* (1994) are included, suggesting that the correlation of Grigg and Jones may not be real.

Whatever mechanism is invoked for deposition of the Molokai conglomerate, it must be capable of imparting simple trends to the deposit while carrying debris to

elevations at least 72 meters above sea level and more than 2 kilometers inland, if sea level was not higher at the time. A storm is unlikely to have created the Molokai conglomerate for two reasons; the unit is unique within the last 240,000 years on Molokai, and no modern storm has moved debris to the distances and elevations seen on Molokai. A single tsunami, probably generated by one of the large submarine landslides off the Hawaiian islands, is the most likely mechanism.

Figure 1. Index maps. **a**, Location of Molokai in the Hawaiian Islands. **b**, Generalized geology of Molokai and location of the study area on Molokai. **c**, Location of grain size measurements in the study area. Sites marked with a square are from a single stream gulch as recorded in Figures 2d, 5 and 6b, c. Numbered sites refer to photographs in later figures.

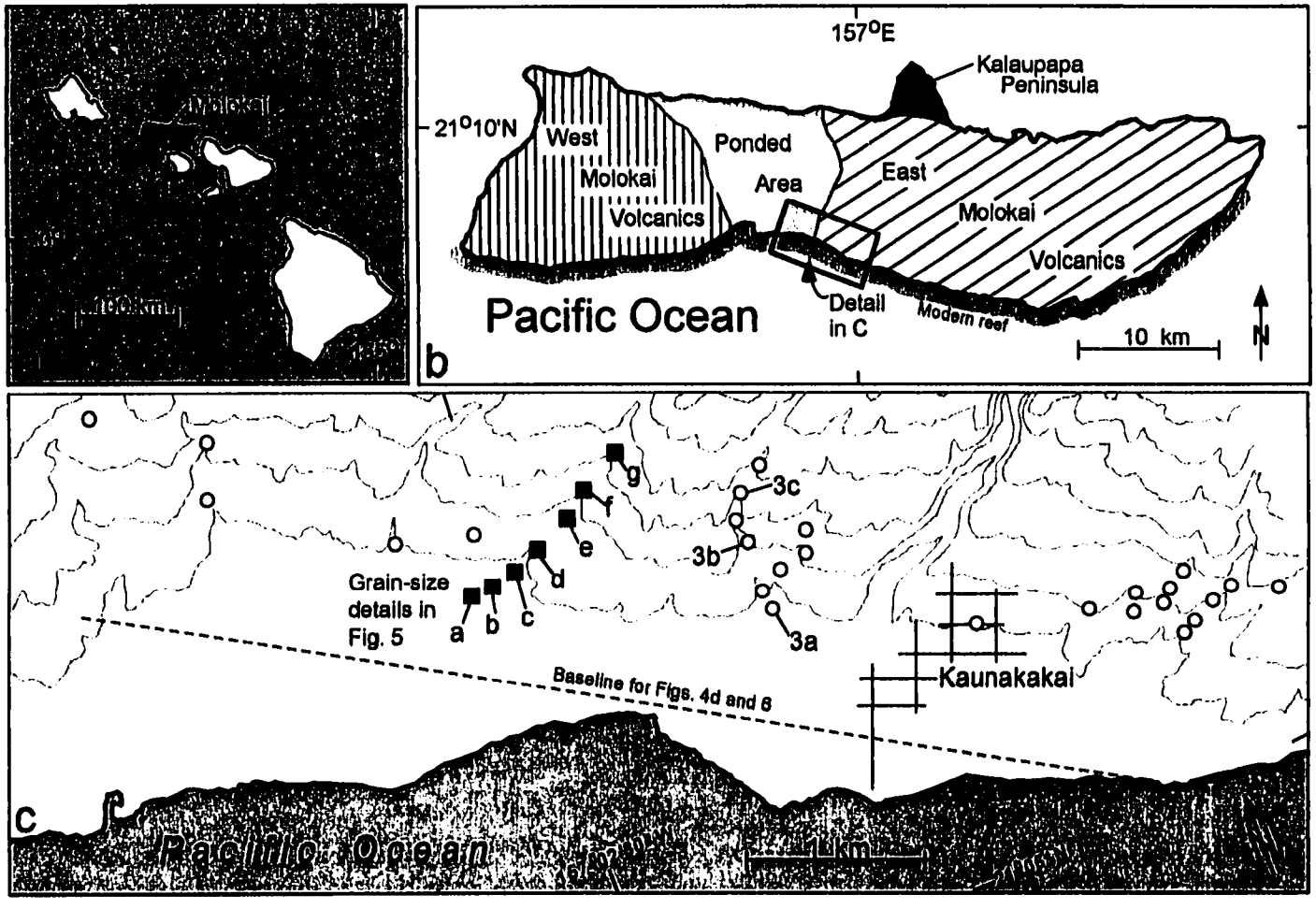
157°E
21°10'N
Kalaupapa Peninsula
West Molokai Volcanics
Ponded Area
East Molokai Volcanics
Detail in C
Modern reef
10 km
N
Pacific Ocean
b
Grain-size details in Fig. 5
a
b
c
d
e
f
g
3a
3b
3c
Baseline for Figs. 4d and 6
Kaunakakai
Pacific Ocean
1 km
c

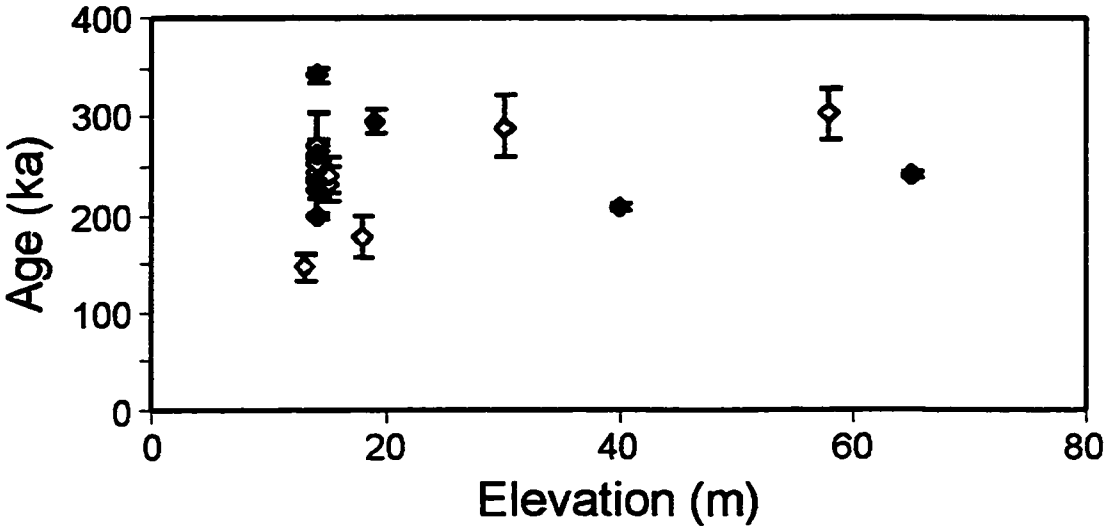

Figure 2. Ages and elevations of carbonate clasts in the Molokai conglomerate. Open diamond sites are electron-spin resonance ages from Grigg and Jones (1997); black diamond sites are U-Th ages from Moore *et al.*, (1994). Error bars are two sigma uncertainties reported by the authors.

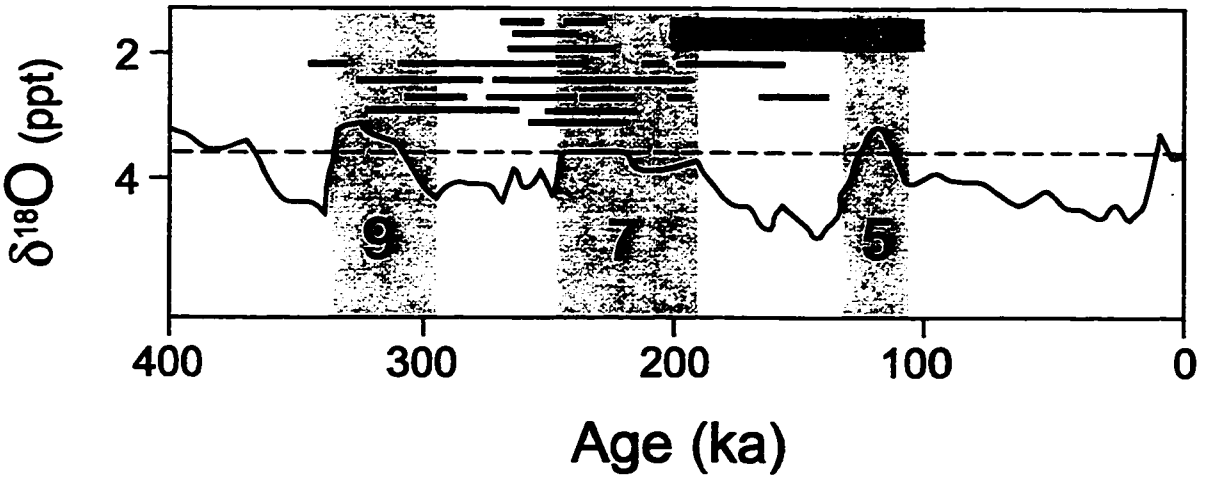

Figure 3. Relationship between numeric ages of corals in the Molokai conglomerate and low values of $\delta^{18}O$, a proxy for sea level ($\delta^{18}O$ curve after Shackleton et al., 1988). Gray bars are ESR ages and reported 1σ error bars from Grigg and Jones (1997). Black bars are U-Th ages and reported 1σ error bars from Moore *et al.* (1994).

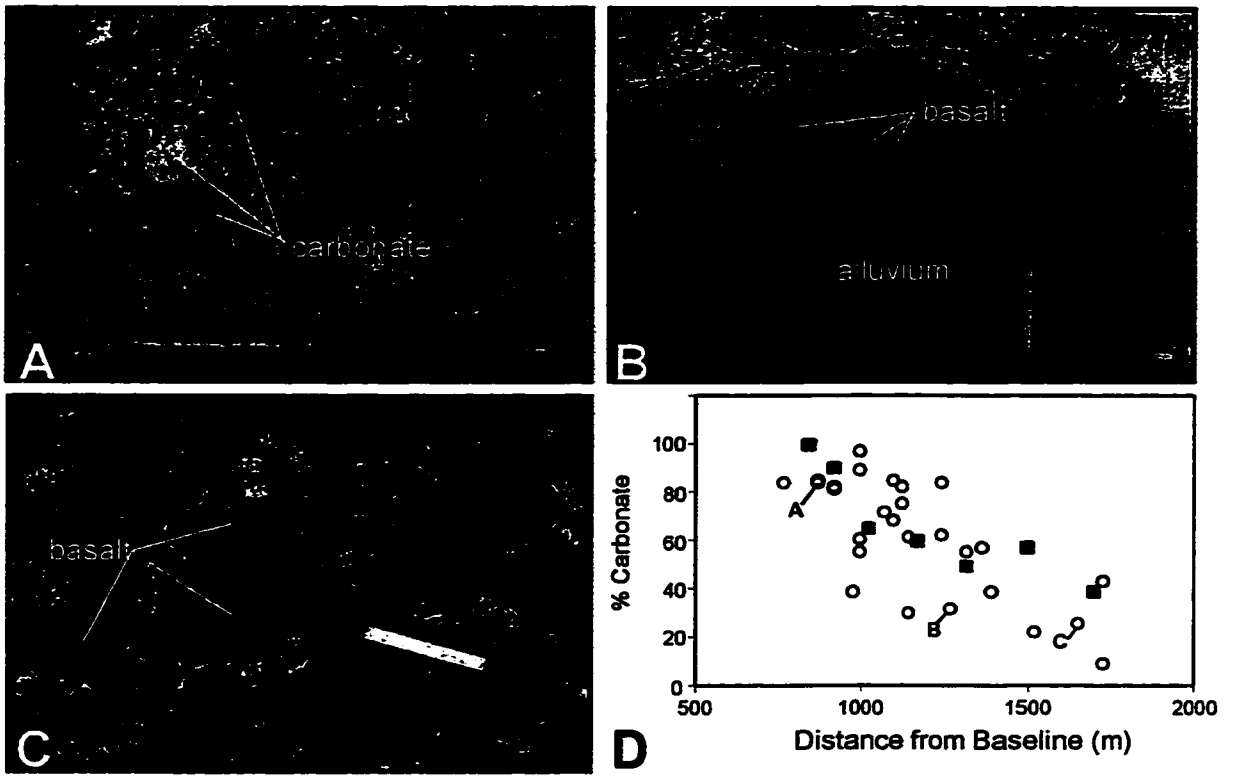

Figure 4. Conglomerate composition. **a,** Carbonate-rich conglomerate typical of low elevation sites. Coral debris is abundant, whereas basalt is almost completely absent. **b,** Mixed carbonate/basalt deposit overlying older alluvium. Note the absence of bedding or other sedimentary structures. This mixed assemblage is typical of most of the deposit. **c,** Basalt rich location typical of upland sites in the boulder conglomerate. **d,** Change in the composition of the boulder conglomerate with distance from the baseline shown in Figure 1c. Dark squares refer to sites within a single stream drainage shown in Figure 1c.

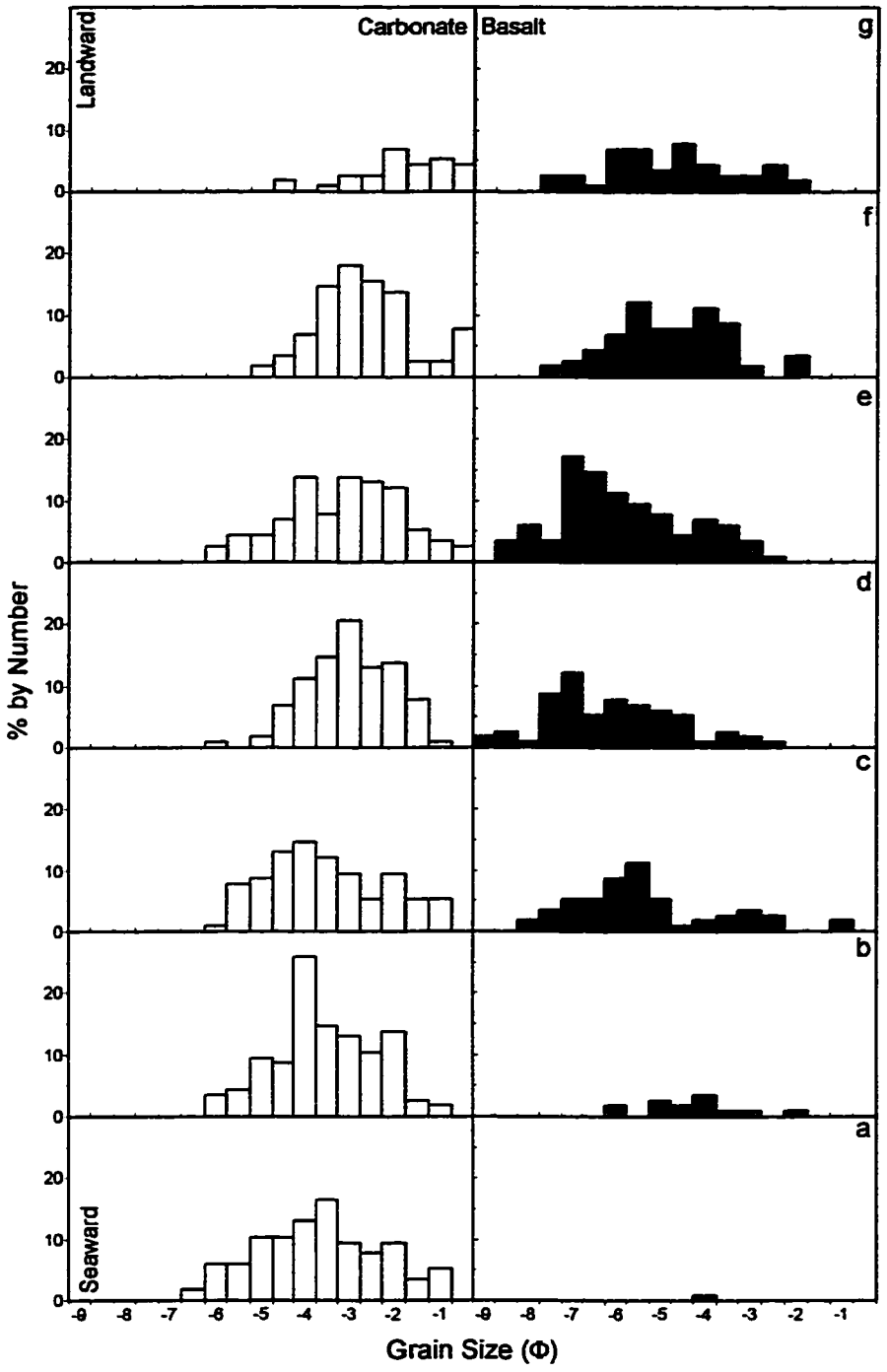

Figure 5. Grain-size histograms for study sites from a single valley (squares in Figure 1c). Shaded portions of the graph are basalt; unshaded are carbonate. $\Phi \equiv -\log_2 D(mm)$.

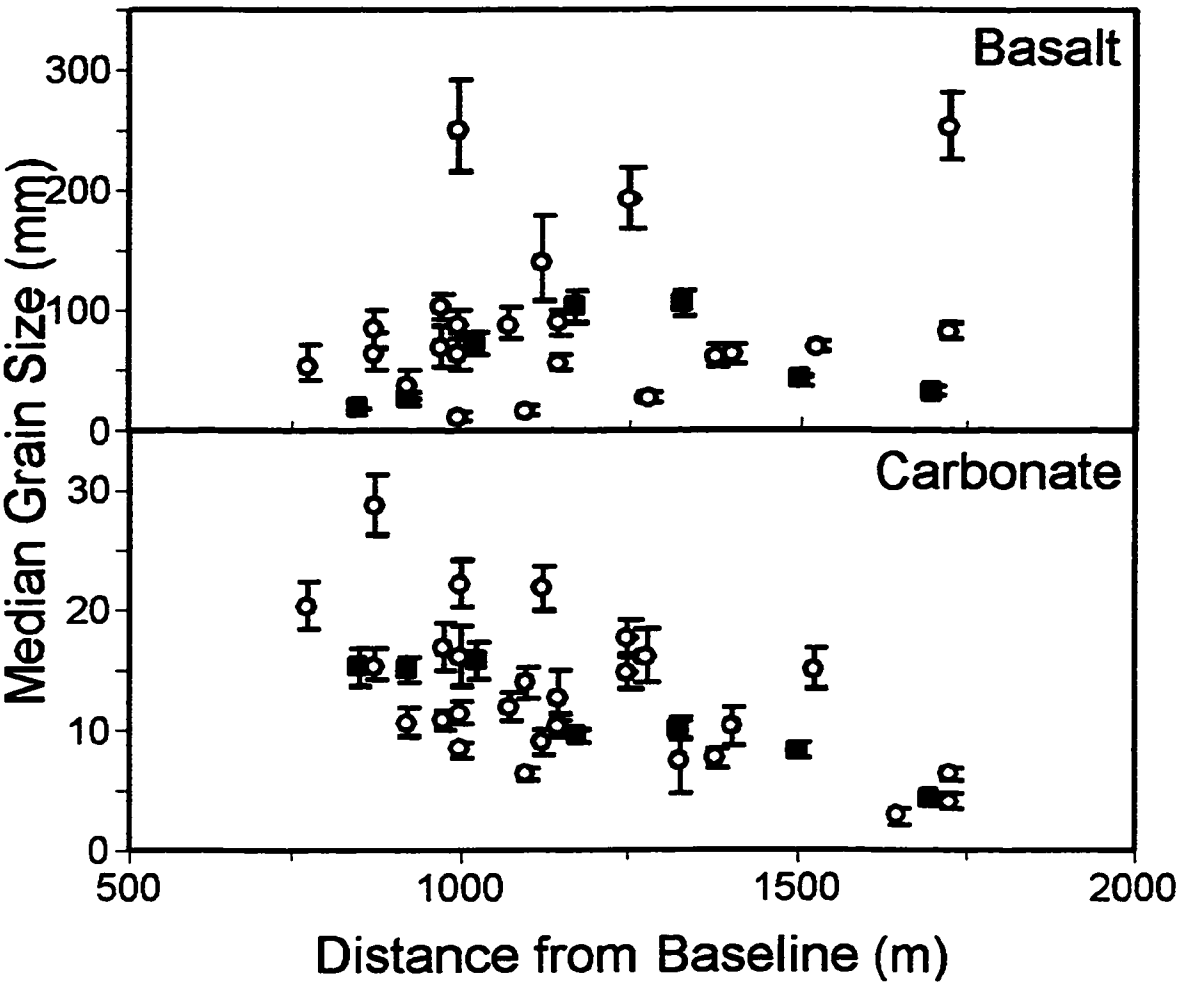

Figure 6. Changes in median grain size (of the apparent long axis) with distance from the baseline in Figure 1c. Error bars are one standard error and were determined in phi units, resulting in asymmetry when converted to millimeters. **a**, Median grain size of basalt. **b**, Median grain size of limestone. Dark squares refer to data from within a single stream drainage as shown in Figure 1c. Raw data from which median grain sizes were determined are available in Appendix A.

CHAPTER 2: PARTICLE ADVECTION BY TURBULENT BORES ONTO A SLOPING BEACH

INTRODUCTION

A common feature of areas struck by tsunamis is the presence of blocks of debris, such as building rubble or coral reef debris, that were moved by the waves (Yamashita, 1995; Nakata and Kawana, 1985; Makino, 1981). This bouldery material may be the only geologic record of ancient tsunamis in coastal areas where sand sheets were not deposited. The tsunami history of some tsunami-prone areas may be clarified by quantifying the relationship between the distance traveled by blocks of debris and the size of the wave that moved them.

Most studies of tsunami sedimentation have focused on sand sheets (*e.g.*, Pinegina and Bourgeois, 1998; Moore *et al.*, 1996; Shi *et al.*, 1995; Moore, 1994; Reinhart, 1991). These studies have quantified the change in grain size within the deposit, and attempted to use this change to determine flow characteristics of the depositing wave. Attempts to model deposition of sandy debris have been chiefly analytic, with little data from experiments or modern tsunamis to help validate their models (*e.g.*, Moore and Mohrig, 1994; Moore, 1994, Reinhart, 1991).

Fewer tsunami studies have dealt with deposition of cobbles, boulders, and large blocks of debris. These studies have principally involved measurement of the size and location of tsunami-moved rocks and building debris. Among the few attempts to

determine flow characteristics from large debris, most have involved the balance of forces on a single large block (Bourgeois *et al.*, 1988; Noji *et al.*, 1985), and not the average advection of similar objects.

Studies of recent tsunamis have provided few data for studying cobble and boulder transport. Most of the tsunamis studied extensively by international survey teams in the past decade have been too small to have moved enough gravel to demonstrate depositional patterns like landward fining in large grain sizes. Even in those cases where more than isolated particles of gravel have been moved (such as the 1996 Irian Jaya tsunami), the gravel has not been transported far enough for fining to be discernable (Figure 7). Although some historical tsunamis have moved gravel debris a great distance (including the 1960 Chile tsunami, the 1883 Krakatau tsunami, and the 1771 Meiwa tsunami), little more than anecdotal evidence remains of the movement of this material.

Here I circumvent lack of field data by using results from scaled tsunamis simulated in a wave tank. The use of objects representing scaled boulders in the flow allows for observation of the behavior of large objects moved by tsunamis. The wave tank can be heavily instrumented, allowing for the collection of precise data on flow depth and flow velocity. Waves of varying size can be produced as needed, allowing for observation across a range of incident tsunamis. The shoreline topography can also be simplified, minimizing focusing and diffraction from local shoreline features, thus giving the results applicability beyond any one local area.

I simulated tsunamis as bores. While natural tsunamis need not behave as turbulent bores, bores are commonly used to simulate tsunamis in the lab because of their ease of generation and hydraulic similarity to tsunamis (Ramsden, 1993; Yeh, 1991). Both authors created bores with a dam-break gate, allowing for the sudden gravitational collapse of water impounded behind the gate. I show that, for a fixed slope and roughness, the average distance traveled by large objects depends on the depth and velocity of the flow and on the size and density of particles. I also present a scaling argument for use in estimating the size of natural tsunamis from the position of large debris they left behind.

ANALYTIC CONSIDERATIONS

VISCOUS EFFECTS

Viscous effects can be neglected in tsunami wave tank experiments, even at large scale factors (Yeh, 1991, Yeh *et al.*, 1989, Ramsden, 1993, Miller, 1956). To maintain dynamic similarity in any fluid model, both Froude number and Reynolds number must be kept equal between the model and the prototype. Here Froude number is defined as:

$$Fr = \frac{u}{\sqrt{gd}} \qquad (3)$$

where Fr is the Froude number, u the depth-averaged flow velocity, g the acceleration of gravity, and d the flow depth. The Reynolds number is defined as:

$$Re = \frac{ud}{v} \qquad (4)$$

where Re is the Reynolds number, v the dynamic viscosity, and u and d defined as for Froude number. For extremely turbulent systems Reynolds number becomes sufficiently large that similarity is achieved simply by requiring that the Reynolds number be large enough to place the flow in the turbulent regime.

The Reynolds number for even a small tsunami approaching land is very small. Take a 100 cm bore with a flow velocity of 100 cm/s, in water at 20°C (yielding a dynamic viscosity of 0.01 cm^2/s). These conditions yield a Reynolds number of $1x10^6$, which is fully turbulent for $d/k_s<500$ on a Nikuradse diagram (Figure 8). This d/k_s ratio corresponds to a bed roughness of 2 mm or larger. Larger waves will become fully turbulent for even smaller bed roughness heights. An error of no more than 10% in friction factor is accrued if the the model falls in the transition zone, rather than the fully turbulent zone. Including transistional Reynolds numbers increases the range of d/k_s to $d/k_s<2500$, which corresponds to a roughness height of 0.4 mm in the example above.

To maintain Reynolds scaling the flow need only be in the fully turbulent or transition zones for the experimental bores. Experimental values for d range from 6.6 cm to 8.9 cm, whereas k_s remains constant and is taken as D_{90} for the grit on the sloping beach, 0.125 cm. In the experiments d/k_s ranges from 52.8 to 71.2. Measured velocities ranged from 110 cm/s (for flow depth of 6.6 cm) to 185 cm/s (for flow depth of 8.9 cm). For these model velocity/depth combinations, and a water temperature of 20°C, the flow

plots in the fully turbulent regime on a Nikuradse diagram (Figure 8). For all model experiments the flow remains fully turbulent, and viscous forces can be neglected.

FORCE SCALING

The two forces mainly responsible for determining the advection length of a particle are the force on the particle in the direction of transport, and the submerged weight of the particle. The submerged weight of the particle (F_w) is simply determined as:

$$F_w = (\rho_s - \rho_f)gV \qquad (5)$$

where ρ_s is the density of the particle, ρ_f is the density of the fluid, g is the acceleration of gravity and V is the volume of the particle.

For bores, velocity in the direction of travel is much greater than vertical or cross-stream velocity components. The force acting on a particle in the direction of transport can be simplified to the force acting on a particle in the direction of travel, here defined as the x-direction (Figure 9). The x-direction force on a particle has been expressed by O'Brien and Morison (1952) to be the sum of a drag term proportional to the square of the velocity, and an inertial term proportional to the instantaneous acceleration:

$$F_D = \frac{1}{2}\rho_f C_D A u^2 + \rho_f C_M V \dot{u} \qquad (6)$$

where C_D is the drag coefficient, A is the projected area of the particle in the flow direction, u is the depth averaged flow velocity, $\dot{u}$ is the instantaneous acceleration, and C_M is the inertia coefficient.

For fully turbulent flow viscous forces are negligible, so I can provisionally assume that advection length scales with the ratio of the buoyant weight of the particle and the in-line force on the particle:

$$\frac{(\rho_s - \rho_f) g V}{2\rho_f C_D A u^2 + \rho_f C_M V \dot{u}} \qquad (7)$$

The inclusion of an inertial term in the in-line force equation, however, makes this assumption difficult to use because coefficient of inertia is difficult to estimate for natural particles. Both drag coefficient and coefficient of inertia are strongly time-dependent for bores, although drag coefficient becomes stable after the initial passage of the bore front.

My experiments show that cubes are not moved during the maximum acceleration of a bore, but rather during the maximum velocity, suggesting that drag force and not inertial force dominates movement. Although the bore front is a region of strong acceleration, Noji *et al.* (1985) report that the force exerted on a cube by a bore reaches a maximum at the maximum velocity, rather than the maximum acceleration. Additionally, I noted in the experiments that the particles are entrained after passage of the bore head, in a region of the bore with relatively stable velocity. As shown in Figure 10, a 32 mm

aluminum particle located approximately 2 meters from the dam break gate is struck by a bore of height 4 cm flowing into still water of depth 2 cm. The bore was chosen to be close to the minimum required to move the cube so that maximum resolution between the time of maximum fluid acceleration, the time of maximum fluid velocity, and the time of initial particle movement could be obtained. Fluid velocity reaches a stable value approximately 3.5 seconds after release of the dam break gate. First motion of the particle was observed 3.9 seconds after release of the gate. Because a finite amount of time is required to establish velocity profiles in the flow, and consequently full hydraulic drag on the cube, first motion occurs well after the zone of acceleration at the bore head. I therefore neglect the inertial term, and simplify the force group to:

$$\frac{2(\rho_s - \rho_f)gV}{\rho_f C_D A u^2} \qquad (8)$$

For a steady unidirectional flow, Equation 8 simplifies to the square of the ratio of particle settling velocity (w) and flow velocity:

$$\left(\frac{w}{u}\right)^2 \qquad (9)$$

from which I simplify a dimensionless relative velocity, w/u.

I also define a relative length scale, L/h, where L is the average distance traveled by particles of the same size and density, and h is the bore height that entrains the particles. These two dimensionless groups (L/h and w/u) should provide a basis for plotting the effect of particle parameters and flow parameters on advection length.

EXPERIMENTAL EQUIPMENT AND PROCEDURES

The experiments were made in a 20-m long wave tank fitted with a pneumatically activated gate 7 meters from the head tank (Figure 11). The tank is 60 cm wide and 45 cm deep, with a stainless steel bottom plane to within ±1 mm and an overall slope of $4x10^{-4}$ in the downstream direction. The tank walls are plate glass 1.3 cm thick. The lift gate is of stainless steel 0.64 cm thick, and rides in an ultra-high molecular weight (UHMW) plastic trackway fitted into the walls of the tank. The gate is lifted by a 6.4 cm diameter pneumatic piston driven by 70 psi air. The piston can lift the gate at 2 m/s, allowing the gate to clear the top of the tank in 0.2 seconds.

The tail end of the tank had a wooden beach with a slope of 0.1. From the floor of the tank to 0.2 cm elevation the beach was faired to the tank floor with silicone sealant (Dow RTV-108). From 5 cm to 0.2 cm elevation, the beach consists of rough stainless steel. From 5 cm to the maximum beach height at 35.4 cm, the beach was roughened with coarse sand (D_{50} = 0.84 mm, σ_i = 0.436 Φ) cemented to the wooden beach. The top of the beach ends 1.6 m from the end of the tank to provide an overflow area and to prevent water from sloshing out of the tank.

The position of the water surface was recorded with two capacitance wave gauges consisting of 0.31 cm diameter stainless steel rods coated with plastic tubing and sealed at the bottom with a plastic plug. One was placed 2.21 m downstream from the lift gate, the other 5.87 m from the gate, just "seaward" of the beach toe. The wave gauges hold their calibration in air or water, but are sensitive to temperature and the proximity of a

boundary, with a 2°C change in temperature changing the wave gauge reading by the equivalent of a 1 mm change in the water surface. The gauges were manually calibrated for temperature and wave height, then left in position for the duration of experiments. The resolution obtained by the wave gauges was ±0.05 mm over their 20 cm height.

Water temperature was recorded with a thermistor immersed between the dam break gate and the head tank. Because the thermistor's response time is slow, it was placed in the still water behind the gate, rather than next to each wave gauge. Output from the thermistor was routed through a strain gauge amplifier, which increased the resolution of the gauge, but decreased its range. The final resolution was ±0.007 °C.

Data acquisition of the wave gauges and thermistor was controlled by a microcomputer equipped with a 12-bit analog-to-digital converter. The converter was set to sample at 100 Hz and to accept a voltage range from 0 to 10 V with a sampling accuracy of ±2.5 mV.

A side-looking acoustic Doppler velocimeter (ADV) measured water velocity. The ADV samples at 25 Hz, and is capable of precision to ±0.1 cm/s. Because air entrainment on the probe tips of the ADV makes the signal noisy at high flow velocities, a clay fairing was used to guide air away from the probe tips. This fairing extended approximately 1 cm upstream of the arms of the ADV probe (7.6 cm in diameter) and approximately 5 cm downstream from the arms. As a result, flow on the "back" side of the ADV (the side away from the ADV sampling volume) was locally disturbed, so that it was considered necessary to remove the ADV from the immediate vicinity of the

particles. The ADV was mounted along with the wave gauge 2.21 m downstream from the lift gate. The probe was placed so that the sampling volume was at the minimum possible distance from the bed (6 cm), so that even small bores could be measured by the ADV, and 8 cm from the tank wall to avoid side wall interference.

The advection distance of each particle was recorded with a super-8 video - recorder mounted on a moveable bracket over the tank. The camera was oriented so that its plane of view was parallel to the beach. Marks placed every centimeter along the centerline and each edge of the beach provided calibration for the camera view.

I made experiments with cubes of four different densities (S.G.=1.12, 1.56, 1.78, and 2.71) at a single particle size (D=16 mm). I also made experiments with five particle sizes (D=8 mm, 12 mm, 16 mm, 20 mm, and 24 mm) at a single density (S.G.=2.71). For each run, a variable amount of water (ranging from 25 cm to 42.5 cm) was placed between the head tank and the gate, and 2 cm of water between the gate and the beach. Five particles were placed along the beach, with their centers 10 cm apart and their upstream edges placed at the waterline, to minimize the effects of partial submergence on the results. Before the gate opened, 30 seconds of temperature data were recorded, and the video recorder started. Activating the gate started data collection on the ADV and wave gauges. Each experimental setup (water impoundment, particle size, and particle density) was repeated six times, so that 30 advection lengths for each setup were recorded. Results are tabulated in Appendix B.

Cubes were used to model natural particles for a variety of reasons. First, natural particles are rarely smooth enough to undergo the sharp reduction in drag coefficient experienced by spheres at high Reynolds numbers. This is because, unlike spheres, natural particles have sharp points or rough surfaces to cause the flow around the particle to separate. Cubes also have sharp edges, which serve to force the flow around the particle to separate. As a result, cubes mimic the drag characteristics of natural particles better than spheres do. Second, the geometry of a cube is simple, so that calculation of parameters such as the cross-sectional area presented to the flow or particle volume is easy when compared to more complex shapes. Third, previous experimenters have used cubes to model natural particles (Noji *et al.*, 1985), making my experiments more directly comparable to those of others. Lastly, particles with a more rounded shape tended not to stay in one location on the beach, but to roll downslope before arrival of the bore.

RESULTS

Despite variability in advection length for given particle and wave parameters (Figure 12; Appendix B), the median advection length shows a strong correlation with both bore velocity and bore height (Figure 13a & b). Similarly, if bore parameters are held constant, the advection length correlates with particle size and density (Figure 14a & b). These trends confirm that advection length is a linear function of particle and bore parameters.

Because particle settling velocity depends largely on particle size and density, the data in Figures 12 & 13 can be condensed with the use of two dimensionless groups: a

length group (advection length, L, over wave height, h), and a velocity group (particle settling velocity, w, over flow velocity, u). The data plot along a straight line with w/u and L/h as the horizontal and vertical axes, respectively (Figure 15). Here w is computed following Dietrich (1982), u is the velocity measured from the ADV, L is the median advection length, and h is the bore height at the forward wave gauge.

INTERNAL CONSISTENCY OF RESULTS

The experimental results are internally consistent. In addition to showing that particles with the same settling velocity, but different diameter or density, fall on the trend, the data suggest that the value of the L/h and w/u intercepts are consistent with their physical meaning. These values are experiment-specific, but can be shown to vary with slope and bottom roughness, such that the trend for any site should be a straight line running from the ratio of inundation distance to bore height on the vertical axis to the critical velocity ratio for particle movement on the horizontal axis.

Although it seems intuitive for the results to become asymptotic as they approach either axis, the data suggest that the trend is linear. As w/u approaches zero, either grain diameter becomes very small or grain density approaches fluid density until at w/u=0 the particle becomes equivalent to a water molecule in the flow. Water has a finite advection length as well, equal to the inundation distance. For w/u=0, L/h becomes inundation distance normalized by initial bore height. Yeh *et al.* (1989) give a simple expression for the runup height by the complete conversion of bore velocity head to elevation head:

$$R = \frac{u^2}{2g} \qquad (10)$$

where R is runup height. Equation 10 is easily incorporated into the dimensional analysis by taking $R=L_r S$ and $u^2=Fr^2gh$:

$$\frac{L_r}{h} = \frac{Fr^2}{2S} \qquad (11)$$

where L_r is the maximum inundation distance and Fr is the Froude number. Equation 11 suggests that the value of L/h at $w/u=0$ is a function solely of initial Froude number, and beach slope.

The experimental data are consistent with the idea that when the particle has an infinitely small settling velocity, its advection length approaches the inundation length. The experiments show that water just runs over the top of the sloping beach (354 cm from the toe of the slope) for an initial bore height of 5.7 cm, resulting in $L/h=62.1$, close to the best-fit line intercept of 61.65 (Figure 15). If the Yeh expression with the measured velocity of 165 cm/s is used, however, a runup ratio of only 15.3 results. This may be because the runup expression in Equation 10 is frictionless. Inclusion of a functional dependence on friction factor of form:

$$\alpha f^{\beta} \qquad (12)$$

where f is the friction factor, and α, β are unknown constants, into Equation 10, allows Equation 10 to be written as:

$$\frac{L_r}{h} = \frac{F^2}{2\alpha f^{\beta} S} \qquad (13)$$

As *L/h* approaches zero, the flow becomes inadequate to move particles of a given settling velocity. At *L/h*=0, *w/u* is simply the ratio of settling velocity to depth averaged bore velocity at initiation of motion. This point was verified for my experiments by using the best-fit line x-intercept (*w/u*=0.65, Figure 15) to determine the velocity required to initiate motion of a 32 mm aluminum cube. For this velocity (*u*=60 cm/s), experiments with 32 mm cubes produced *L/h* values from 3 to 6. These values are within the range of error of the best-fit line.

For large particles in turbulent flows, Shields (1936) indicates that the dimensionless critical shear stress required for entrainment of a particle in a bed of similar particles becomes constant. In this case:

$$\tau_* = \frac{\tau_0}{(\rho_s - \rho)gD} = \chi \qquad (14)$$

where τ_* is dimensionless shear stress, τ_0 is bottom shear stress, and χ is a constant. Equation 14 can be rewritten by substituting $u_*^2=\tau_0/\rho$ to:

$$u_* = \sqrt{\chi\left(\frac{\rho_s - \rho}{\rho}\right)gD} \qquad (15)$$

The settling velocity of a cube can be determined analytically to be:

$$w = \sqrt{\frac{2}{C_D}\left(\frac{\rho_s - \rho}{\rho}\right)gD} \qquad (16)$$

Equations 15 and 16 can be combined to yield:

$$\frac{w}{u_*} = \sqrt{\frac{2}{\chi C_D}} \qquad (17)$$

which implies that the ratio w/u_* remains fixed when dimensionless shear stress is constant. Flow velocity, however, is related to shear velocity through friction factor, which is, in turn, a function of the relative height of roughness elements on the bed. For large bores, such as broken tsunami waves, this effect may be minimal, because the effective roughness-element height will be small relative to the height of the incoming wave where trees and buildings are absent. Secondly, more recent refinements to Shields' work (Wiberg and Smith, 1987) have shown that the entire Shields curve shifts in response to changes in the ratio between the size of the moving particle and the bed roughness height (D/k_s). The present experimental results suggest this effect may also be minimal for bore transport, because a threefold change in relative roughness caused by using different particle sizes does not noticeably affect the trend of the data. Although Wiberg and Smith show changes caused by order-of-magnitude changes in D/k_s, some overall change in the data should be visible for the threefold change in D/k_s represented by the data. Also, the modern tsunami data suggest minimal change due to relative roughness effects, because the point at which a trend line through the modern tsunami

data strikes the *w/u* axis falls close to the experimentally derived value (*w/u*=0.8) (Figure 16). These results suggest that the *w/u* ratio may remain fairly constant for changes in relative roughness.

The results indicate that any natural site should produce a unique linear trend on axes of *w/u* for the horizontal and *L/h* for the vertical, running from normalized runup length on the *L/h* axis intercept to the critical velocity ratio on the *w/u* axis intercept. The point at which each linear trend strikes the *w/u* axis appears to be fixed, whereas the intercept with the *L/h* axis appears variable, and a function of friction factor, slope, and initial Froude number.

COMPARISON WITH MODERN TSUNAMIS

I compare the experimental data with data collected from three modern tsunamis: the 1992 Nicaragua tsunami, the 1996 Irian Jaya tsunami, and the 1998 Papua New Guinea tsunami.

NICARAGUA

On September 2, 1992, a large earthquake (M_w=7.5-7.6) occurred along the Middle America Subduction Zone about 100 km southwest of Managua (Abe *et al.*, 1993; Satake *et al.*, 1993). The earthquake generated a devastating tsunami with field-measured tsunami elevation (above mean sea level) indicators found as high as 5 to 6 meters above sea level (Abe *et al.*, 1993; Satake *et al.*, 1993). Near El Popoyo (and elsewhere), eyewitnesses reported hearing noise as the wave approached the coast,

suggesting that it may have approached as a bore. As the wave flooded coastal lowlands, a brick house was destroyed, spreading brick debris downstream from the building. Later surveys by Joanne Bourgeois (unpublished data) determined the location of this debris and estimated the flow depth of the wave to be 2.2 m (above local ground level) based on impact damage to trees. I used the median advection length of this debris and the estimated flow depth in all calculations. Because no independent velocity estimates are available, I have assumed a Froude number of 1 (if, as evidence suggests, the wave acted as a bore, hydrodynamically defined to have Froude number near 1), and estimated flow velocity from flow depth at the crest of a low beach berm.

IRIAN JAYA

On February 17, 1996, a great earthquake (M_w=8.1) occurred on the New Guinea Subduction Zone near Biak Island (Imamura *et al.*, 1997). The maximum measured tsunami elevation above mean sea level was 7 m on Biak. On Owi Island, 7 km southeast of Biak, eyewitnesses reported that a small wave broke on a coral reef, then advanced as a bore 100 meters across the reef flat to the shore, where small (D=20 mm) pieces of coral were deposited (flow depth estimated at 1.55 m as measured by impact damage on palm trees). I used the median grain size at four locations on Owi Island to determine advection length. As in the Nicaragua case, because no independent estimates of velocity were available, and because the wave advanced as a bore, I assumed a Froude number of 1 for the purpose of estimating velocity.

Papua New Guinea

On July 17, 1998, a large earthquake (M_w=7.2) occurred near the north coast of Papua New Guinea near the town of Sissano. Although the earthquake was relatively small, coastal communities were devastated by a wave with flow depths estimated as high as 3.4 meters. Near Sissano, a large coral block (intermediate axis=75 cm) was moved 80 meters across a reef flat by a bore that broke on the outer edge of the reef, according to eyewitness accounts (Boyd Benson, unpublished data).

Comparison

When data from modern tsunamis are plotted with experimental results, the field data uniformly plot above the experimental data trend (Figure 16). Points lying above the trend indicate that the model has overestimated the size of the wave and can be considered a limiting maximum. This discrepancy might be due to a difference in slopes: the natural particles moved across relatively flat ground, whereas the experimental particles moved up a 1:10 slope. If the slope of the modern tsunami cases is assumed to be 1° (the slope of each case must be estimated because the topography is complex) and adjusted using Equation 11, the modern tsunami data plots on the experimental data (Figure 17). Because a separate friction factor correction was not required for three different cases, L_r/h may be only a weak function of friction factor in most natural situations.

COMBINATION OF EXPERIMENTAL AND FIELD DATA

The experimental data may be combined with data from tsunami deposits to yield expressions for bore height and velocity. The experimental data yield a best-fit line of the form:

$$\left(\frac{L}{h}\right)=-a\left(\frac{w}{u}\right)+b \qquad (18)$$

which involves two constants (a and b), two field-measurable quantities (L and w), and two unknowns (u and h). An analysis by Stoker (1944) for bores traveling into water of finite depth can be used to decouple u and h:

$$\frac{u}{c_0}=\frac{\dot{\xi}}{c_0}-\frac{c_0}{4\dot{\xi}}\left(1+\sqrt{1+8\left(\frac{\dot{\xi}}{c_0}\right)^2}\right) \qquad (19)$$

where u is the velocity within the bore, c_0 is the shallow water wave speed in the still water landward of the bore ($c_0^2=gh_0$, where h_0 is the depth of the still water), and $\dot{\xi}$ is the speed of the moving bore front, given implicitly by Stoker (1948) as:

$$-c_0^2\dot{\xi}=c^2\left(u-\dot{\xi}\right) \qquad (20)$$

Making the substitutions $\dot{\xi}=c^2u/(c^2-c_0^2)$, $c_0^2=gh_0$, $c^2=gd$, $d=h_0+h$, Equation 19 simplifies to:

$$u = \frac{d - h_0}{h_0}\sqrt{\frac{d - h_0}{d}}c_0 = \frac{h}{h_0}\sqrt{\frac{h}{d}}c_0 \qquad (21)$$

where h_0 is the depth of still water in front of the bore, d is the depth of water behind the bore, and h is the height of the bore. For large waves in shallow water, h/d is close to 1, so the square root term drops out, leaving a first order approximation:

$$u = \frac{c_0 h}{h_0} = \sqrt{\frac{g}{h_0}}h \qquad (22)$$

Substituting Equation 22 back into Equation 18 yields an expression for h:

$$h = \frac{L}{b} + \frac{aw\sqrt{h_0}}{b\sqrt{g}} \qquad (23)$$

IMPLICATIONS FOR SORTING IN TSUNAMI DEPOSITS

The data in Figure 15 show that the experimental bores are capable of sorting sediment. The degree to which sorting occurs, however, may be influenced by a number of parameters, including particle size, particle density, source, roughness elements, slope, and D/k_s.

PARTICLE SIZE AND DENSITY

The results suggest that advection length is relatively insensitive to changes in grain size. Taking an analytical expression for settling velocity of spheres:

$$w = \sqrt{\frac{4}{3}\frac{1}{C_D} gD\left(\frac{\rho_s}{\rho} - 1\right)} \qquad (24)$$

it becomes apparent that w increases as the square root of both D and submerged specific weight, so that either D or submerged weight must increase four times to double settling velocity. For example, the trend line developed from the experiments suggests that a 10 m bore advects a 5 cm quartz sphere, on average, 500 m up a 1:10 slope, whereas a 25 cm sphere is advected 335 m. The difference decreases further if sediment density is reduced. For the same grain sizes, but a specific gravity of only 1.7, the median advection distances are increased to 540 m and 445 m for 5 cm and 25 cm spheres, respectively.

SOURCE REGION

Grain size trends having a flat slope with respect to advection length are especially sensitive to changes in the width (in the direction of advection) of the particle source area. The experiments used a point source, but changing the source to a band (such as a beach) would increase the scatter in the trend. This effect may be minimal for large, dense, particles, which tend to show steeper trend lines, but may be especially pronounced for small, less dense, particles. Additionally, if the band from which the particles come is large relative to the advection length of the particles, trends may be totally obscured.

SINGLE PARTICLE VS. MEDIAN ADVECTION LENGTHS

In addition to systematic changes caused by slope and source region, sorting trends will be obscured by the scatter in advection lengths of identically sized particles.

My experiments show that the normalized standard deviation (the standard deviation in advection lengths divided by the median advection length) for identical particles is approximately 0.1, suggesting that particles will be found in a broad cluster around the median. Although this scatter will not alter sorting in median grain size based on large populations of particles (since for a large number of observations, the median will be known precisely), it will obscure trends inferred from small numbers of large objects (because the median will not be known precisely). This effect will be heightened for particles with different shape but similar diameter. To combat this problem, studies of grain size distribution in tsunami deposits should not rely on maximum size, or maps of object size, but should instead determine median grain size within the deposit at any point. Estimates of flow depth or velocity derived from single object advections should include at least 10% uncertainty from advection length scatter.

The results suggest that although bores do sort sediment, trends in gravelly tsunami deposits may be hard to recognize where the wave flowed up a steep slope, or where the source region is diffuse. This effect is especially pronounced for small, low-density particles, like coral or bricks, where changes in diameter do not cause large changes in settling velocity. Where the source area is broad relative to the size of the wave (*i.e.*, where the particles cannot be considered to have had a point source), grain size trends may become so obscured as to be indistinguishable.

SUMMARY

The advection distance of objects struck by turbulent bores is a function of the settling velocity of the object, the height of the bore, flow velocity within the bore, and the location of advection. Calibration of this function for any site should enable engineers to estimate how far objects will travel when struck by a given bore height, and geologists to estimate the size of ancient tsunamis by measuring advection lengths.

I modeled the movement of particles in turbulent bores by fitting a 15 m wave tank with a dam-break gate, and using this apparatus to send bores onto a 1:10 slope holding cube-shaped particles. My experiments consisted of making eight different bore heights and measuring the movement of five different cube sizes and four different densities.

The data plot as a linear trend on the non-dimensional axes L/h and w/u, where L is advection length, h is bore height, w is particle settling velocity, and u is velocity within the bore. The intercept of this trend with L/h represents the ratio of bore inundation distance to bore height, whereas the intercept with w/u represents the largest ratio of particle fall velocity to flow velocity which can be moved in the wave tank. Both these intercepts were experimentally confirmed.

Although the trend is site-specific, this trend should change somewhat predictably. The location of the L/h intercept is a function of friction factor and slope, increasing with decreasing slope and friction factor. The modern tsunami examples suggest that the location is only weakly dependent on friction factor, and is predominantly a function of slope. The modern tsunami data suggest that the location of

the *w/u* intercept is probably less mobile, but is a function of the relative roughness for large particles.

Inclusion of a first-order approximation of Stoker's (1948) analysis of bore velocity yields a simple expression for incident bore height as a function of the slope and *L/h* intercept of the trend line, the settling velocity and advection length of the particle of interest, and the depth of water into which the bore travels. This relationship allows for the estimation of wave height from particles moved by ancient tsunamis.

Figure 7. Photograph of corals moved by the 1996 Irian Jaya tsunami on Owi Island, Indonesia (1°14′S, 136°12.5′E). Corals are bleached, suggesting that their source was the beach 10 meters to seaward of the photo and not a nearby fringing reef. Although numerous, these particles have not traveled far enough for grain size changes to be discernable. Dark band running from upper left to lower right is woody debris collected behind a low berm.

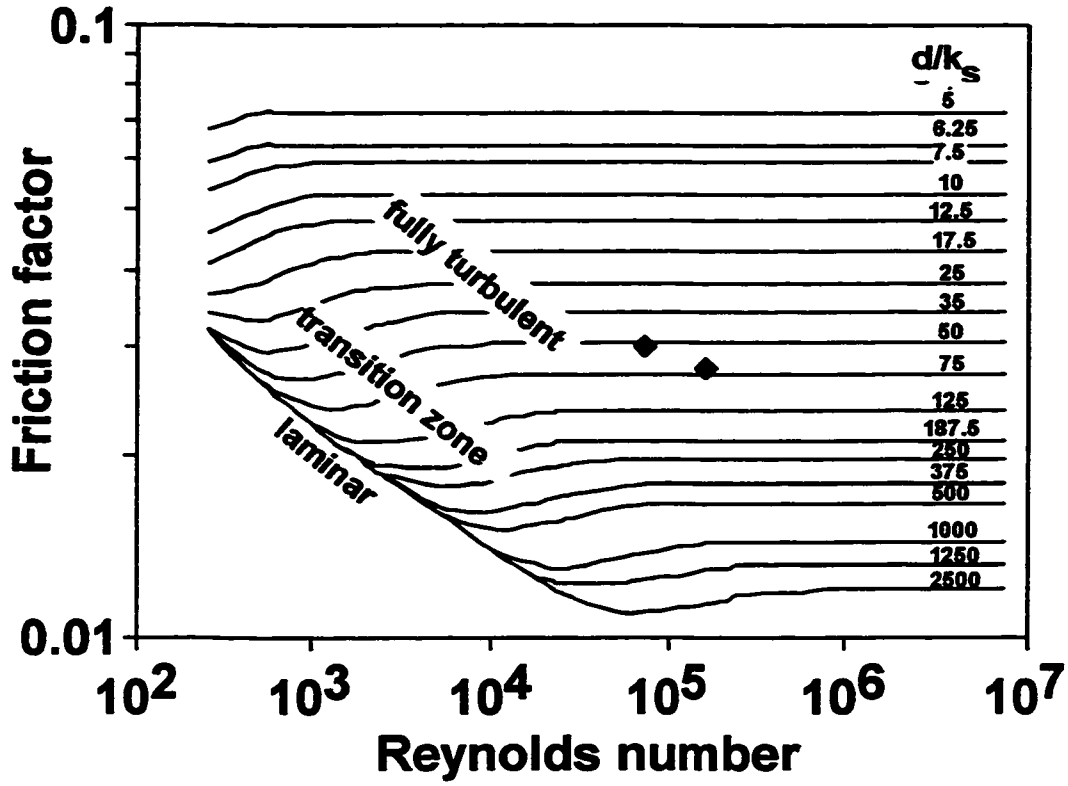

Figure 8. Nikuradse diagram (after Brownlie, 1981) with extremes of the experimental data plotted. Black diamonds represent extremes of the experimental data, and plot in the fully turbulent zone, showing that the viscous effects of the wave tank can be neglected. Here, d is the flow depth (taken to be the bore height) and k_s is the height of roughness elements on the bed.

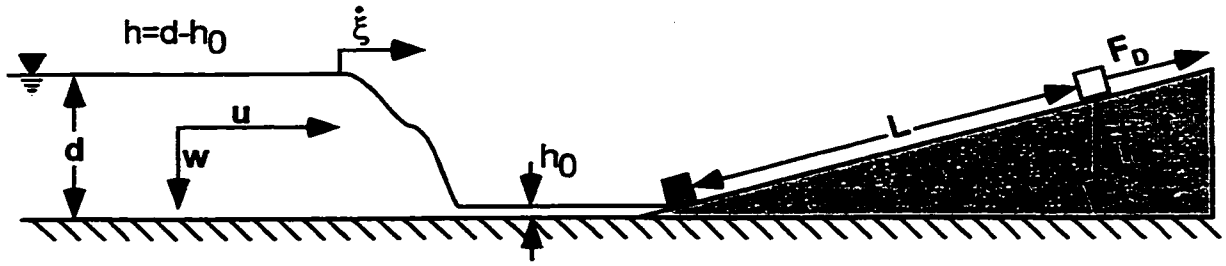

Figure 9. Definition sketch for wave-tank experiments.

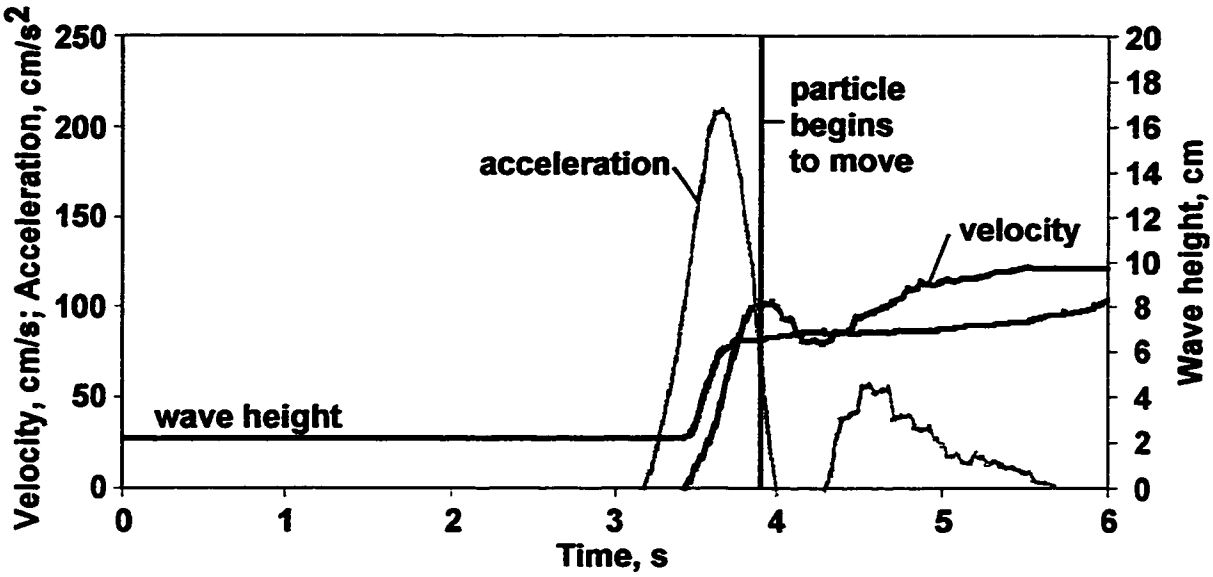

Figure 10. Time of initial particle motion relative to flow velocity and acceleration. The particles move in a local velocity maximum in the turbulent front of the bore, rather than in a local acceleration maximum.

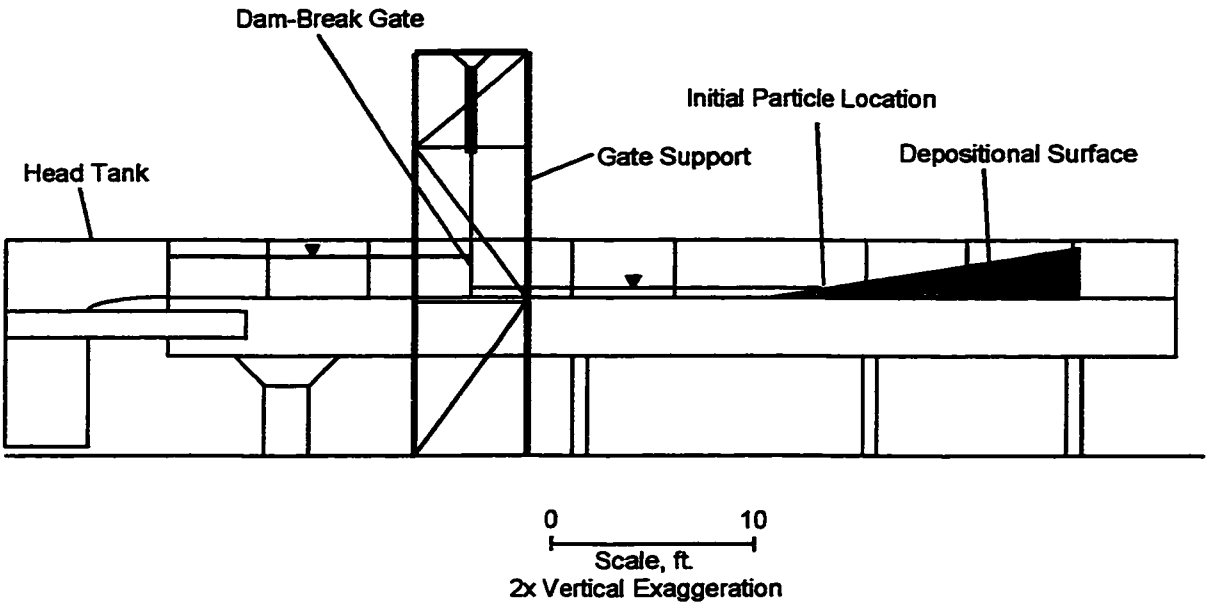

Figure 11. Schematic drawing of the wave tank used for the experiments. For all experiments, the depth of water between the gate and the depositional surface was 2 cm and the maximum possible advection length was 354 cm.

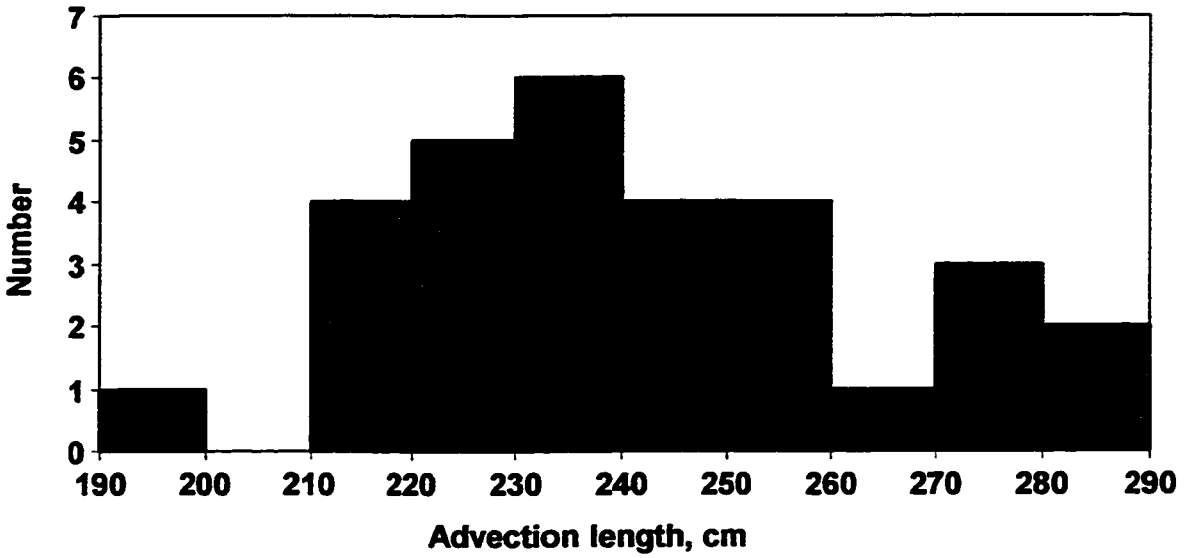

Figure 12. Histogram of measured advection lengths for 16mm aluminum cubes moved by a 6.5 cm high bore with peak horizontal velocity of about 155 cm/s.

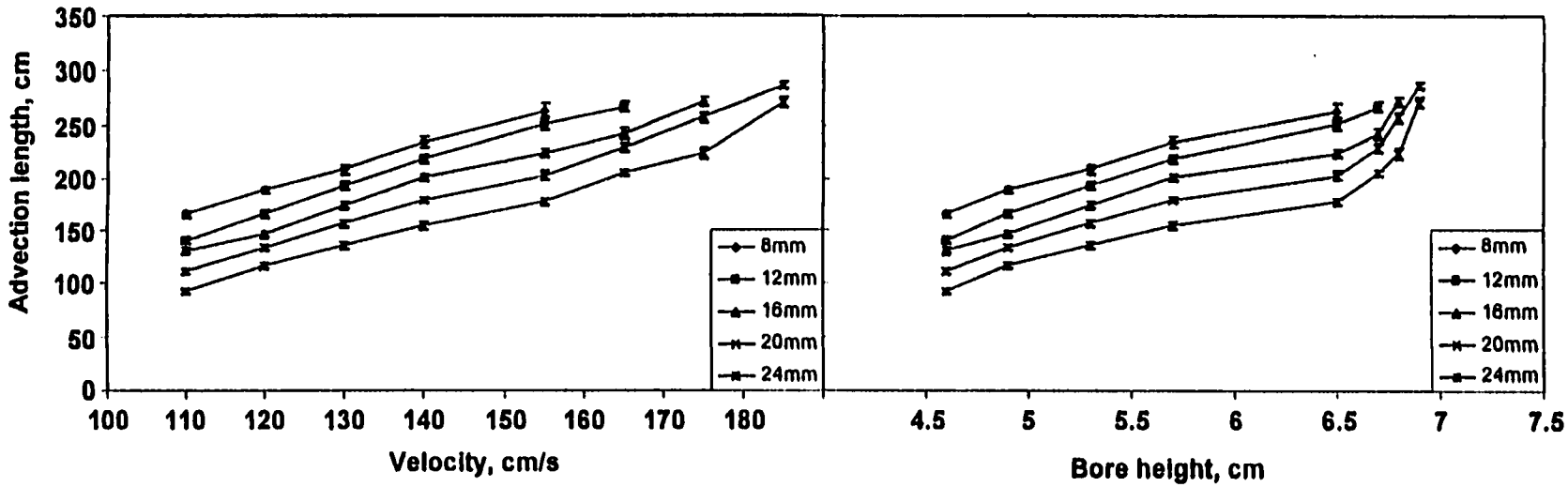

Figure 13. **a,** Median advection length vs. bore peak velocity for aluminum cubes. **b,** Median advection length vs. bore height for aluminum cubes. Each point is the average of 30 particle advections (Appendix B).

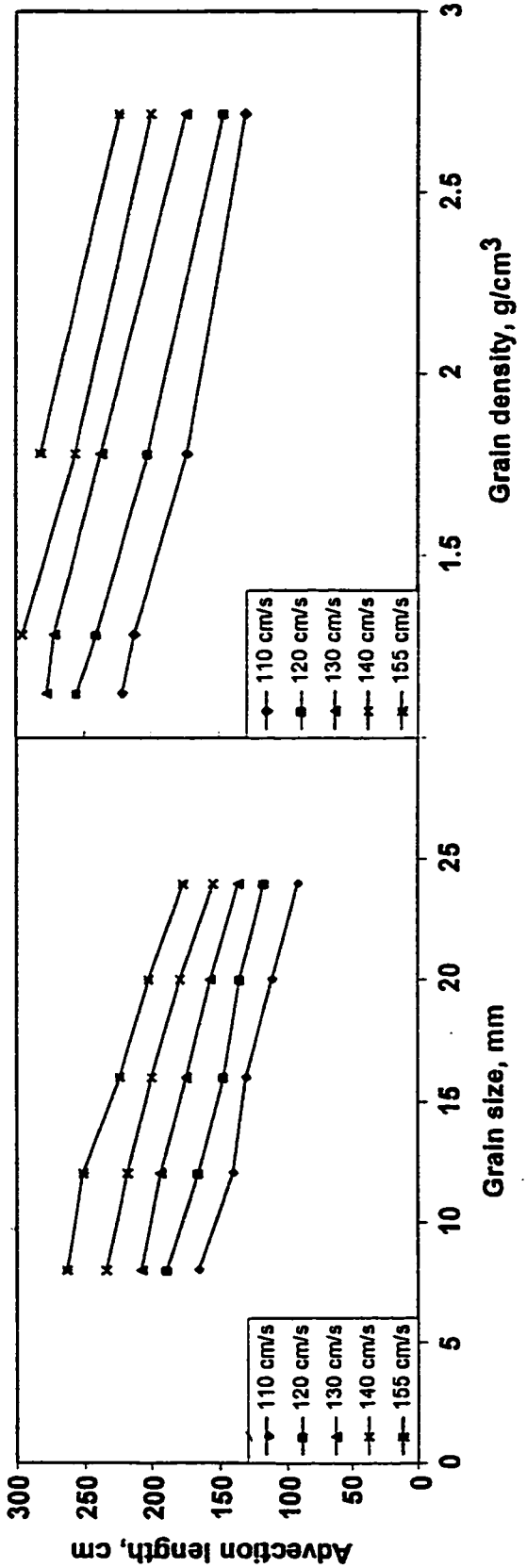

Figure 14. a, Median advection length vs. grain size for aluminum cubes. **b,** Median advection length vs. grain density for 16 mm cubes. Each point is the average of 30 particle advections (Appendix B).

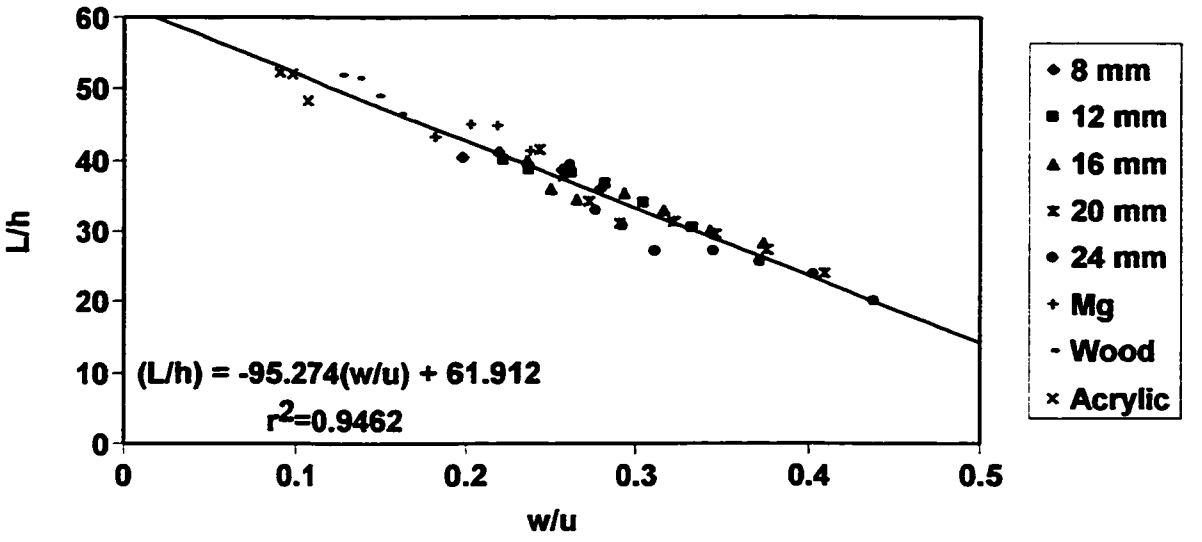

Figure 15. Median advection length (L) normalized to bore height (h) vs. settling velocity (w) normalized to measured flow velocity (u).

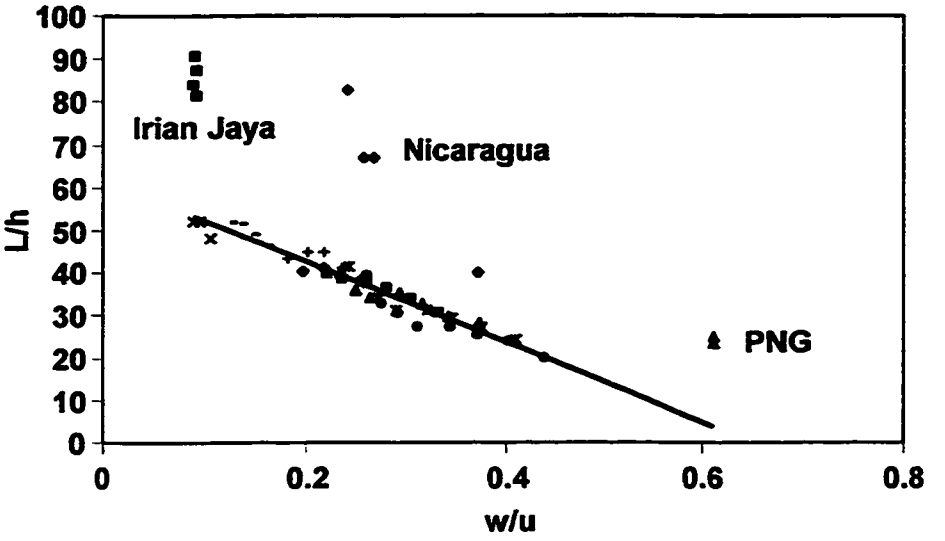

Figure 16. Advection data from natural tsunamis plotted on same axes as experimental data. L is the median advection distance, h the bore height (as determined by flow-depth indicators measured by field surveys), w the particle settling velocity (calculated using Dietrich, 1982), and u the depth-averaged flow velocity (calculated assuming $u^2=gh$). Data used for modern tsunamis are summarized in Appendix C.

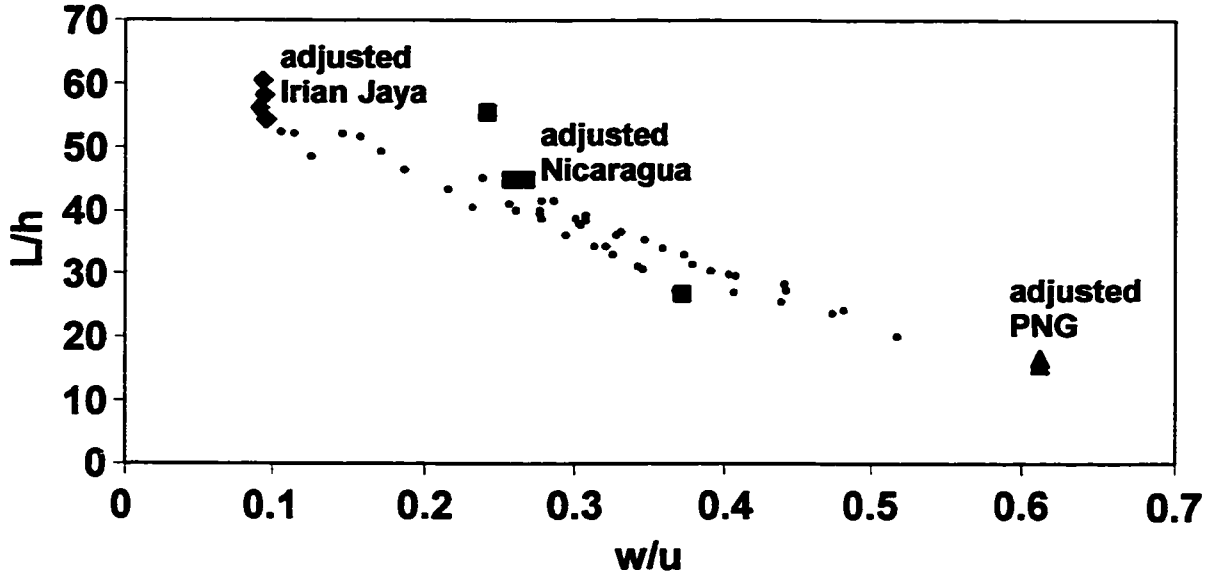

Figure 17. Modern tsunami data adjusted for slope (by recalculating the advection length each benchmark particle would have traveled up a 1:10 slope using Equation 11) and plotted on same axes as experimental data (small dots).

CHAPTER 3: SIZE ESTIMATE OF A POSTULATED TSUNAMI ON MOLOKAI, HAWAII

INTRODUCTION

Giant submarine landslides are widespread on the flanks of many oceanic volcanoes (Holcomb and Searle, 1991). Perhaps the best described of these are the giant landslides on the submarine flanks of the Hawaiian Islands (J.G. Moore *et al.*, 1989). The Hawaiian landslides can cover up to 23,000 square kilometers and extend down slope more than 200 km, placing them among the largest landslides on Earth.

Landslides into oceans commonly generate tsunamis (*e.g.* Latter, 1981; Pararas-Carayannis, 1979; Miller, 1960; Neumann Van Padang, 1930; Omori, 1907). Even fully submarine landslides are thought to have generated tsunamis as shown by a Quaternary tsunami associated with the Storegga slides (Bondevik and Svendsen, 1993; Long *et al.*, 1989), the 1929 Grand Banks tsunami (Hasegawa and Kanamori, 1987, and the 1992 Flores Island tsunami (Yeh *et al.*, 1993). Although aqueous submarine landslides may be inefficient at generating tsunamis (LeBlond and Jones, 1995; Jiang and LeBlond, 1992, 1993, 1994), the landslides associated with oceanic islands commonly have subaerial headwalls, making them more effective at generating tsunamis than are totally submarine slides (including the landslide-generated wave in Lituya Bay, Alaska, in 1958 (Miller, 1960)).

Postulated tsunami deposits reported on the Hawaiian islands of Lanai and Molokai have been ascribed to the movement of submarine landslides (J.G. Moore and G.W. Moore, 1984; G.W. Moore and J.G. Moore, 1989; J.G. Moore *et al.*, 1994; Moore, 1997). The deposits commonly consist of a grain-supported conglomerate made up of a mixture of coral fragments and basalt in a matrix of cemented soil and carbonate mud. The deposits extend from near sea level to at least 150 m on Lanai and 80 m on Molokai. The source of these deposits is surmised by J.G. Moore to have been shallow-marine sediments transported by runup from the large waves generated by submarine landslides originating from the flanks of the Hawaiian Islands.

These interpretations have been challenged on three fronts. First, according to Grigg and Jones (1997), the conglomerates formed at or near sea level, and reached their present level because of uplift. Second, there may be insufficient coral in front of Lanai to produce the deposit on that island—a problem that does not hold for Molokai (Richard Grigg, personal communication). Third, even a giant submarine landslide is incapable of generating wave heights large enough to reach the highest elevations to which coral was moved, according to numerical modeling by Johnson and Mader (1994).

In this paper I estimate tsunami height on Molokai from the grain size of the deposit. Johnson and Mader (1994) assumed that wave runup (the elevation to which water climbs as the wave strikes shore) is roughly equivalent to the incoming wave height, and that the maximum elevation of the tsunami deposit is equivalent to the runup. Studies of modern tsunamis show these heights to be different. I assume that the coral

fragments picked up by the tsunami were derived from a single source area, probably a carbonate beach or fringing reef. Using field evidence, we estimated the distance the particles traveled. This distance, together with their settling velocity, can be used to estimate wave height, if combined with results of experimental studies using scaled bores. These studies show a simple relationship between particle parameters (advection length and settling velocity) and flow parameters (flow velocity and bore height) (Figure 15) for a fixed slope (Chapter 2). I apply this relationship to estimate advection length and settling velocity.

Because advection length is so dependent on the location of the shoreline, which is difficult to estimate, I consider two scenarios, one where advection takes place from a full glacial shoreline, and one where advection takes place from an interglacial shoreline. I maximize all other parameters with the full glacial scenario, so that it can reasonably be considered a maximum estimate. My best geological estimates of all parameters are combined with the interglacial shoreline to produce a most geologically reasonable estimate.

APPROACH AND ASSUMPTIONS

I use the experimental results from Chapter 2 to estimate the size of the tsunami required to produce the Molokai conglomerate. The experimental work gave an expression for bore height as a function of measurable variables:

$$\frac{L}{h} = \frac{-aw}{u} + b \qquad (25)$$

where h is the bore height, L is the median advection length of groups of particles, w is the settling velocity of the particles, and a and b are functions of the model results applicable to the region. A first-order relationship between flow depth, u, and bore height, h, is also given in Chapter 2:

$$u = \sqrt{\frac{g}{h_0}}h \qquad (26)$$

where g is the acceleration of gravity and h_0 is the depth of still water into which the wave travels (Figure 9). Combining these two equations yields:

$$h = \frac{L}{b} + \frac{aw\sqrt{h_0}}{b\sqrt{g}} \qquad (27)$$

Equation 27 shows the tsunami bore height as a function of variables that can be estimated either from the field data collected on Molokai or from the experimental data. I substitute appropriate values into Equation 27 for each of the field sites reported in Chapter 1, then tabulate the wave height estimated from each site.

Three assumptions go into my estimate of the tsunami wave height. (1) The Molokai conglomerate was produced by a tsunami. I have discussed the reasons behind this assumption in Chapter 1. (2) The tsunami acted as a bore. This assumption is required to use the results of the experimental data. Tsunamis commonly advance as bores after shallowing abruptly, such as striking a fringing reef. Molokai has a

pronounced reef (Figure 1c), making it likely that a tsunami advancing toward the coast of Molokai would do so as a bore. (3) The carbonate material in the Molokai conglomerate came from a beach. If sea level were high, the material may be either from the beach or from the fringing reef, although the range of particle ages reported in Chapter 1 (Figure 2) makes a beach origin more likely, because it seems unreasonable for so competitive an environment as a reef to leave patches of varying age lying available to be moved by tsunami. This source would be the same if sea level were low, and the argument from Chapter 1 that the particles come from highstand reefs were true. Here sea level would be low, but the particle advection lengths would be the same. All experiments from Chapter 2 were run with the particles at the water line, however, so this scenario is not applicable to my data. Lastly, as an extreme, sea level could have been at a low, with particles coming from the low-stand waterline. Although this scenario seems unlikely, I report wave heights for two cases, one where sea level is at its Pleistocene lowest (-125 meters), and one where sea level is at a high stand (0 meters).

PARAMETER ESTIMATES

Each of the parameters in Equation 27 can be estimated from the Molokai field data or from the wave tank experiments. I consider each estimate in a separate section, and tabulate the estimates I used for determining bore height (Table I).

For each parameter I make two estimates: one to give an upper bound for wave size, the other to give a number that is more reasonable geologically.

SETTLING VELOCITY

Settling velocity can be estimated from the graph of median grain diameter vs. distance from an arbitrary baseline given for the Molokai deposit in Chapter 1 (Figure 6). In the Molokai deposit, conversion of grain diameter to grain settling velocity is problematic because the grains are dominantly coral fragments, which are quite non-spherical and are encased in a carbonate matrix from which they cannot be removed. Additionally, the density of carbonate grains is difficult to determine because of the high and variable porosity of biogenic carbonate fragments and post-depositional alteration of the density. To address this problem, modern coral fragments from two locations—the 1996 tsunami deposit from Biak Island, Indonesia, and a beach on the south coast of Molokai—were used to estimate the density and Corey shape factor (CSF) of the Molokai tsunami-deposit corals.

To estimate the Corey shape factor, I measured the long, intermediate, and short (a, b, and c) axes of the modern coral fragments. In both cases, the particles have a wide range of shapes and shape factors (Figure 18), but each shows a clear average. For Irian Jaya, the fragments have an average CSF of 0.55±0.13, whereas the Molokai beach fragments have an average CSF of 0.40±0.11. A t-test of these two populations shows them to be different (the probability that the two samples came from the same population is 0.007%), probably because of species differences in the corals. Because increasing CSF increases settling velocity, which in turn maximizes the estimated size of the wave, I consider two cases; one where wave size is maximized, and one representing best geologic inferences. Here, I keep CSF of 0.55 for the "maximum" case and 0.4 for the

"geologically reasonable" case. The value of 0.55 maximizes settling velocity, hence maximizing wave size, whereas the vaue of 0.4 is probably more appropriate for Molokai because the same coral species are probably represented in the modern and ancient corals.

To estimate the sediment density of the carbonate grains in the Molokai tsunami deposit, I measured directly the density of the coral fragments from Indonesia and the beach at Molokai using a balance and a graduated cylinder. The density estimate of the Indonesian corals (2.21 g/cm^3) is higher than the estimate for the Hawaii corals (2.05 g/cm^3). Because increased sediment density increases settling velocity, I consider the maximum case to have a density of 2.21 g/cm^3, and the geologically reasonable to have a density of 2.05 g/cm^3, again reasoning that the modern and ancient beaches on Molokai probably had similar coral species.

The roundness of the coral fragments in the Molokai tsunami deposit was also estimated from the coral fragments taken from Indonesia and Hawaii. In both cases, the particles are subangular to angular, and are roughened on the surface. Roundness plays a role in settling velocity by altering the wake around the particle, and hence the coefficient of drag. Although not strictly a measure of roundness, in a hydraulic sense increasing surface roughness accomplishes the same effect as increasing angularity—it provides fixed points from which the wake can be generated. Because of this, the coral fragments are assigned a slightly more "angular" Powers index (a measure of roundness) than they might otherwise have received: a Powers index of 2 (corresponding to "angular" sediment).

Taking the reported median intermediate axis from Chapter 1 and the values estimated for sediment density, CSF, and Powers index, I determined the settling velocities of the tsunami deposit coral fragments using an empirical formula derived by Dietrich (1982). These settling velocities (like most settling velocities) are for still water, and do not take into account resuspension. In a tsunami, however, particles may be moved by other waves in the wave train, or be moved down slope by backwash or by streams after the passage of the tsunami, but I have no way of determining these effects. As a result, I consider the still water settling velocity to be the best estimate of settling velocity I have. Still water settling velocities are plotted against advection length to produce graphs of "maximum" and "geologically reasonable" settling velocity change with distance (Figure 19a & b).

ADVECTION LENGTH

To get the true advection distance for the Molokai deposit from the graph of median grain diameter of carbonate particles in the Molokai conglomerate vs. distance from an arbitrary baseline (Figure 6), I need some estimate of where mean sea level was at the time of the wave. In Chapter 1 I estimated the age of the deposit at between 132 and 125 ka. During this interval sea level was no more than about 4 meters above present day, and no more than 10 meters below (Neumann and Hearty, 1996; Hearty and Kindler, 1995). As an absolute maximum, however, sea level has been no lower than 125 meters below present day sea level during the past 400,000 years (Imbrie *et al.*, 1984).

Data from the deposit suggest that the gravel was deposited during high sea level. That is, the lowest elevation sites contain almost exclusively coral debris (Chapter 1). Because the hillsides and submarine flanks of Molokai are composed of basalt, as the wave passes over these areas it would pick up basalt, resulting in a mixed basalt/coral assemblage. Because the low-elevation sites are so coral-rich, it suggests that these sites are not far from the source of coral material. At a maximum, however, advection could not have occurred from farther away than the location of the full-glacial shoreline, at 125 meters below present day sea level. For the maximum case, then, I assume the source of the carbonate material is the full glacial shoreline, and for the geologically reasonable, the modern shoreline.

VALUES OF *a* AND *b*

In Chapter 2 I argue that the value of b in Equation 25 is effectively the ratio of runup to incident bore height, and that it is a function of bore Froude number and slope, and a weak function of friction factor. For a slope of 1:10, corresponding to the subarial flank of Molokai, this value was experimentally determined to be 61.65 ± 0.92. The experimentally derived value is used for both the maximum and geologically reasonable cases.

For the same experiments, the value of a in Equation 25 is a function of how much change in advection length is experienced for a change in settling velocity, for given wave height and velocity. In the extreme, $a=0$ indicates that all particles, regardless of density or diameter, will be carried the same distance, on average, by the same wave

(Figure 15). As a increases, the change in advection length for a change in settling velocity increases. For the experimental setup in Chapter 2, I determined the value of a to be 95.27±2.84. Again, the experimentally derived value is used for both the maximum and most reasonable cases.

STILL WATER DEPTH

The depth of still water in front of a bore determines the ratio of depth-averaged flow velocity, u, to bore height, h (Stoker, 1948). Without an estimate of this parameter, only estimates of the depth-velocity product are possible, because the modeling work from Chapter 2 contains a single function with two unknowns (Figure 14). With a second relationship between bore height and flow velocity, however (through still water depth, h_0), either flow velocity or bore height can be uniquely determined.

The still water depth for the geologically reasonable case is taken as the depth of water over the modern reef (about 3 meters). This value will hold for higher local sea level, because a reef will grow upwards in response to the increased sea level, but will not hold for the significantly reduced sea level of the maximum case. In that case there is no easy way to estimate the still water depth, so the depth is estimated to be 3 meters, assuming that the wave passed over a reef like the one found on Molokai today.

RESULTS

Using Equation 25, I combined every settling velocity - advection length pair in Figure 19a and b with the other parameters estimated (Table I) and used the result to

calculate bore height (Figure 20a and b). The average bore height for the maximum case (Figure 19a) is 75.7 m, with a standard deviation of 4.2 m. For the most geologically reasonable case (Figure 19b), the average height is reduced to 19.3 m, with a standard deviation of 4.2 m. Flow velocity for the maximum case is estimated to be 70.7±4.1 m/s, whereas average velocity for the geologically reasonable case is estimated to be 30.7±7.3 m/s.

In Chapter 1, I estimated u_* for the flow to be about 3.8 m/s, which enables an estimation of friction factor from the relationship:

$$\frac{u}{u_*} = \sqrt{\frac{8}{f}} \qquad (28)$$

Substituting the average values of flow velocity, u, and the calculated values of shear velocity, u_*, into Equation 27 yields a friction factor of 0.14 for the maximum wave estimate and 0.12 for the geologically reasonable. Conversion of these friction factors into Manning's n yields n=0.077 for the maximum and n=0.064 for the geologically reasonable. These values are within the range commonly reported for vegetated flood plains (Morisawa, 1968), which may approximate conditions on the gentle south slope of Molokai.

SENSITIVITY ANALYSIS

Combining the results of scaled lab experiments in Equations 25 and 26 yields:

$$h = \frac{L}{b} + \frac{aw\sqrt{h_0}}{b\sqrt{g}} \qquad (29)$$

which shows that the wave height estimate is the sum of two components, an advection length term and a settling velocity term. In the Molokai case, advection lengths are on the order of thousands of meters, but settling velocities are only on the order of tenths of a meter per second. Even when multiplied by the other factors in Equation 28, the settling velocity term is only about 1% of the advection length term. For the Molokai conglomerate, tsunami height estimates are insensitive to changes in settling velocity or still water depth, and are sensitive to changes in advection length and the value of *b*.

Although the reliance of height estimates on advection length suggests that the longest advection lengths are the most appropriate measures of tsunami size, this is not the case. The experiments in Chapter 2 were reported as average advection lengths; in each case particles were advected significantly farther than the average (Figure 12). As a result, it seems likely that those particles at the farthest inland sites are the result of greater than average advection, rather than average advection by a larger wave.

Advection length estimates are most affected by the estimate of the shoreline location when the tsunami occurred. If the argument that Molokai has been tectonically stable for at least the past 120,000 years is correct, changes in shoreline are due only to changes in global sea level. I have already considered a maximum case corresponding to the lowest global sea levels considered to have occurred in the past 120,000 years; bathymetry off the south coast of Molokai steepens after the 10 meter isobath so that

increasing the advection length further requires an even larger decrease in global sea level.

Factors affecting the value of *b* include friction and slope of the coast, although experiments from Chapter 2 suggest that friction may be less important than slope. The value of *b* used in the tsunami height estimates was determined experimentally for a 1:10 slope, a maximum for the lower slopes of Molokai. Because increasing slope decreases the value of *b* (*b* is the ratio of inundation length to bore height—a flat slope allows a greater inundation length than does a steep slope for the same wave), the height estimates are maximized for slope. Moreover, because of the topography and bathymetry near the shoreline of the south coast of Molokai, the longer the advection length, the flatter the slope, so that increases in advection length are mitigated by decreases in the value of *b*. Friction factors for the experiments in Chapter 2 are approximately 0.03 to 0.04, whereas friction factors for Molokai are probably higher, especially since they include the effects of vegetation and topography. What effect these changes have on the results is currently unknown, but is probably less than that for slope.

SUMMARY

I estimate that the height of a tsunami required to produce a coral-bearing conglomerate on the island of Molokai, Hawaii, is no larger than 75 meters and was probably closer to 20 meters. The maximum figure assumes that sea level was 125 meters below its present level and that particles were advected from that shoreline. It is more likely that if sea level were 125 meters below its present value the coral source would be

an exposed highstand reef, but this scenario cannot be evaluated using the data in Chapter 2.

My model work suggests that the height estimate is the sum of two terms—an advection length term and a settling velocity term. In the Molokai case, advection length is large relative to settling velocity, so that the estimates are dominated by the advection length term. Error in the estimate is due almost entirely to error in estimating the advection length. Increased precision of the estimate will require more precise knowledge of local sea level at the time the deposit was created.

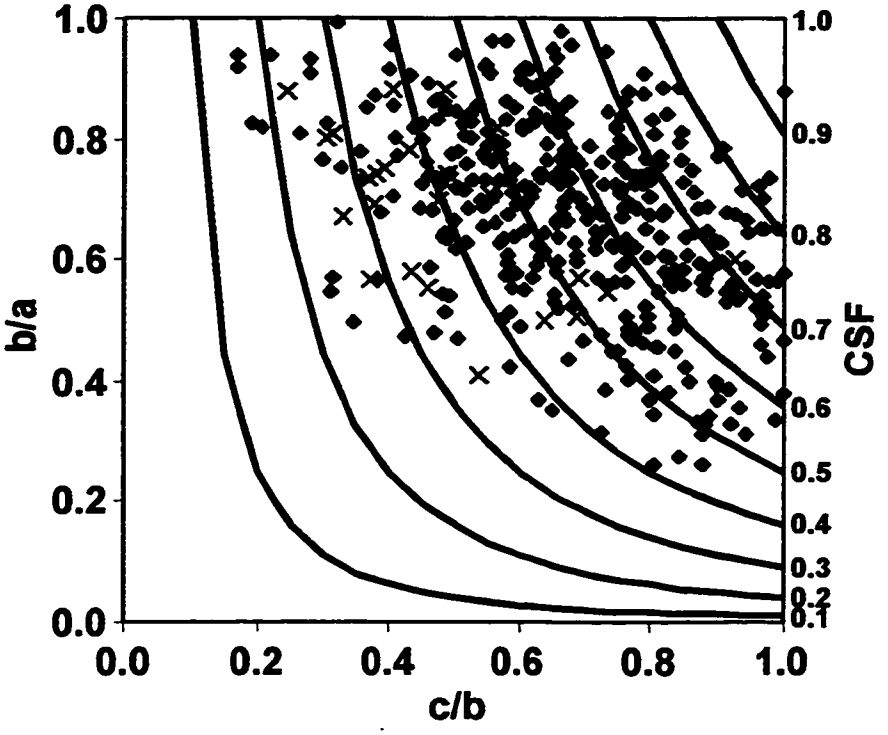

Figure 18. Zingg chart of Irian Jaya coral particles (diamonds) and Hawaii modern beach coral particles (crosses). Horizontal axis represents the ratio of the short axis to intermediate axis of each particle, whereas the vertical axes record the ratio of intermediate to long axes. Dark lines are lines of equal Corey shape factor (CSF), with values for CSF listed on the right side.

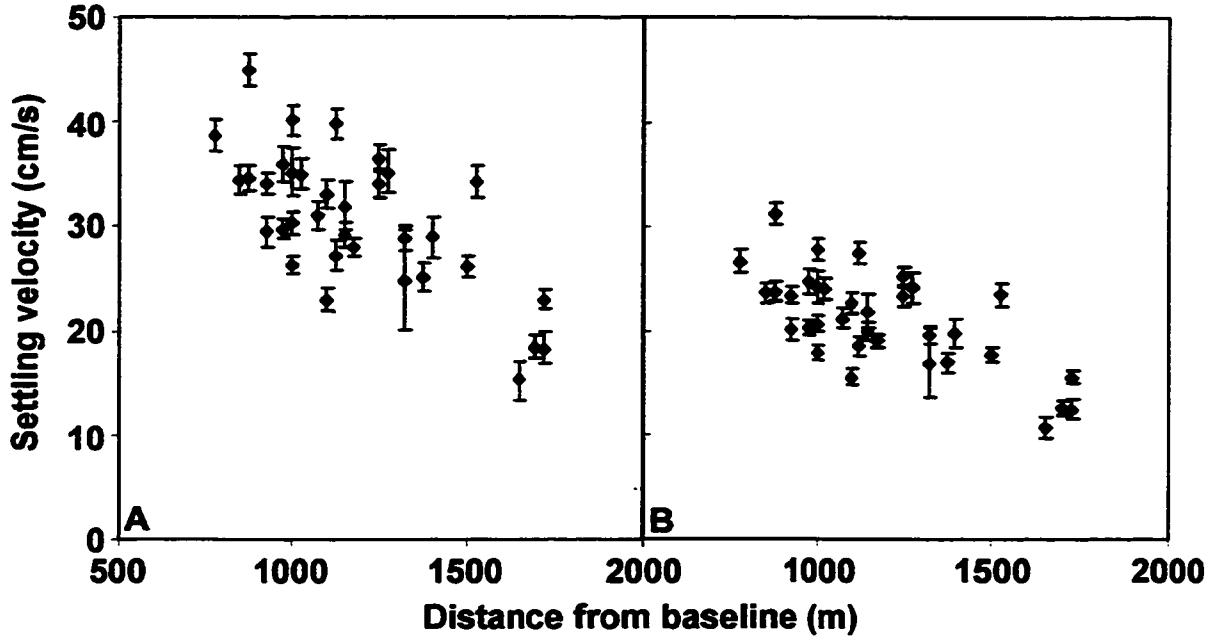

Figure 19. Settling velocity vs. distance from the baseline shown in Figure 1. **a,** Settling velocity computed with "maximum" parameters. **b,** Settling velocity computer with "geologically reasonable" parameters.

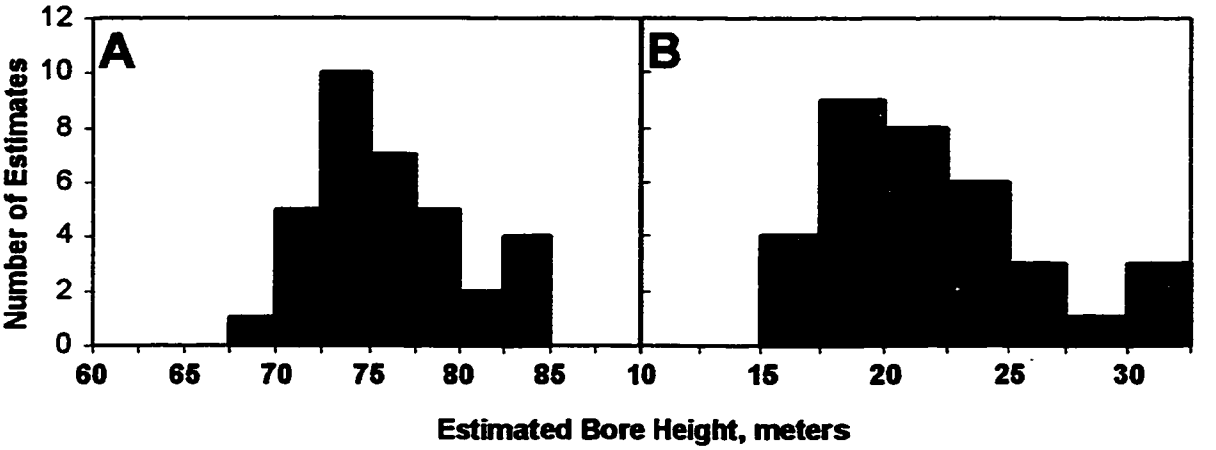

Figure 20. Estimated wave height histograms. **a,** Wave heights estimated from "maximum" parameters. **b,** Wave heights estimated from "geologically reasonable" parameters.

Table I: Parameters used to estimate wave height for each case.

	Maximum wave	Geologically reasonable wave
Corey shape factor (CSF)	0.55	0.4
Sediment density	2.21 g/cm^3	2.05 g/cm^3
Powers index	2	2
Sea level	125 meters below present	present day level
a	95.27	95.27
b	61.91	61.91
still water level (h_0)	3 meters	3 meters

REFERENCES CITED

Abe, Ku., Abe, Ka., Tsuji, Y., Imamura, F., Katao, H., Iio, Y., Satake, K., Bourgeois, J., Noguera, E., and Estrada, F., 1993, Field survey of the Nicaraguan earthquake and tsunami of 2 September 1992, Bulletin of the Earthquake Research Institute, University of Tokyo, v. 68, p. 23-70.

Atwater, B.F., and Moore, A.L., 1992, A tsunami about 1000 years ago in Puget Sound, Washington, Science, v. 258, p. 1614-1617.

Bondevik, S. and Svendsen, J.I., 1993, Palaeotsunamis in the Norwegian Sea and the North Sea, *in* S. Tinti, ed., Genesis and impact of tsunamis on the European coasts. GITEC, p. 7.2-7.27.

Bourgeois, J., Hansen, T.A., Wiberg, P.L., and Kauffman, E.G., 1988, A tsunami deposit at the Cretaceous-Tertiary boundary in Texas, Science, v. 241, p. 567-70.

Bourgeois, J., and Reinhart, M.A., 1989, Onshore erosion and deposition by the 1960 tsunami at the Rio Lingue estuary, south-central Chile [abstract], Eos, Transactions of the American Geophysical Union, v. 70, p. 1331.

Brownlie, W.R., 1981, Re-examination of Nikuradse roughness data, Proceedings of the American Society of Civil Engineers, Journal of the Hydraulics Division, v. 107, p. 115-118.

Clague, D.A., Dao-gong, C., Murnane, R., Beeson, M.H., Lanphere, M.A., Dalrymple, G.B., Friesen, W., and Holcomb, R.T., 1982, Age and petrology of the Kalaupapa Basalt, Molokai, Hawaii: Pacific Geology, v. 36, n. 4, p. 411-420.

Dawson, A.G., Foster, I.D.L., Shi, S., Smith, D.E., and Long, D., 1990, The identification of tsunami deposits in coastal sediment sequences, Science of Tsunami Hazards, v. 8, p. 73-82.

Dietrich, W.E., 1982, Settling velocity of natural particles, Water Resources Research, v. 18, p. 1615-1626.

Folk, R.L., 1974, Petrology of sedimentary rocks, Hemphill, 187 p.

Grigg, R.W., and Jones, A.T., 1997, Uplift caused by lithospheric flexure in the Hawaiian Archipelago as revealed by elevated coral deposits: Marine Geology, v. 141, p. 11-25.

Hasegawa, H.S. and Kanamori, H., 1987, Source mechanism of the magnitude 7.2 Grand Banks earthquake of November 1929: double couple or submarine landslide, Bulletin of the Seismological Society of America, v. 77, p. 1984-2004.

Hearty, P.J., and Kindler, P., 1995, Sea-level highstand chronology from stable carbonate platforms (Bermuda and the Bahamas), Journal of Coastal Research, v. 11, p. 675-689.

Holcomb, R., and Searle, R., 1991, Large landslides from oceanic volcanoes, Marine Geotechnology, v. 10, p. 19-32.

Imamura, F., Subandono, D., Watson, G., Moore, A., Takahashi, T., Matsutomi, H., and Hidayat, R., 1997, Irian Jaya earthquake and tsunami cause serious damage, EOS, Transactions of the American Geophysical Union, v. 78, p. 197, 201.

Imbrie, J., Hays, J.D., Martinson, D.G., McIntyre, A., Mix, A.C., Morley, J.J., Pisias, N.G., Prell, W.L., and Shackleton, N.J., 1984, The orbital theory of Pleistocene climate: support from a revised chronology of the marine $\delta^{18}O$ record. in Berger, A.L., Imbrie, J., Hays, J.D., Kukla, G., and Saltzman, B., eds., Milankovitch and climate, part L. Dordrecht, p. 269-305.

Jiang, L., and LeBlond, P.H., 1992, The coupling of a submarine slide and the surface waves which it generates, Journal of Geophysical Research, v. 97, p. 12731-12744.

Jiang, L., and LeBlond, P.H., 1993, Numerical modeling of an underwater Bingham plastic mudslide and the waves which it generates, Journal of Geophysical Research, v. 98, p. 10303- 10317.

Jiang, L., and LeBlond, P.H., 1994, Three-dimensional modeling of tsunami generation due to a submarine landslide, Journal of Physical Oceanography, v. 24, p. 559-572.

Johnson, C., and Mader, C.L., 1994, Modeling the 105 ka Lanai tsunami, Science of Tsunami Hazards, v. 12, p. 33-38.

Jones, A.T., 1993, Review of the chronology of marine terraces in the Hawaiian Archipelago: Quaternary Science Reviews, v. 12, p. 811-823.

Kellerhals, R., and Bray, D.I., 1971, Sampling procedures for coarse fluvial sediments: Journal of the Hydraulics Division, Proceedings of the American Society of Civil Engineers, v. HY8, p. 1165-1180.

Kellerhals, R., Shaw, J., and Arora, V.K., 1975, On grain size from thin sections: Journal of Geology, v. 83, p. 79-96.

Latter, J.H., 1981, Tsunamis of volcanic origin: Summary of causes, with particular reference to Krakatoa, 1883, Bulletin of Volcanology, v. 44, p. 467-490.

Leatherman, S.P., Williams, A.T., and Fisher, J.S., 1977, Overwash sedimentation associated with a large-scale northeaster, Marine Geology, v. 24, p. 109-121.

LeBlond, P.H., and Jones, A.T., 1995, Underwater landslides ineffective at tsunami generation, Science of Tsunami Hazards, v. 5, p. 6

Long, D., Smith, D.E., and Dawson, A.G., 1989, A Holocene tsunami deposit in eastern Scotland, Journal of Quaternary Science, v. 4, p. 61-66.

Lum, D., 1972, Pleistocene (?) 208-foot emerged shoreline on Molokai, Hawaii [abstract]: Geological Society of America Abstracts with Programs, v. 4, p. 192.

Macdonald, G.A., Abbott, A.T., and Peterson, F.L., 1990, Volcanoes in the sea, 2nd ed., University of Hawaii Press, 517 p.

Makino, K., 1981, Meiwa tsunami in Yaeyama [in Japanese], Jyono Press, 462 p.

McDougall, I., 1964, Potassium-argon ages from lavas of the Hawaiian Islands: Geological Society of America Bulletin, v. 75, p. 107-128.

Miller, D.J., 1960, Giant waves in Lituya Bay, Alaska, USGS Professional Paper 354-C.

Miller, R.L., 1968, Experimental determination of undular and fully developed bores, Journal of Geophysical Research, v. 73, p. 4497-4510.

Minoura, K., Imamura, F., Takahashi, T., and Shuto, N., 1997, Sequence of sedimentation processes caused by the 1992 Flores tsunami: evidence from Babi Island: Geology, v. 25, p. 523-526.

Moore, A.L., 1997, Landward fining in a tsunami-deposited gravel on Molokai, Hawaii [abstract], GSA Abstracts with Programs, v. 29, n. 5, p. 53.

Moore, A.L., 1994, Evidence for a tsunami in Puget Sound about 1000 years ago, unpublished University of Washington Department of Geological Sciences M.S. Project, 38 p.

Moore, A.L., Imamura, F., and Takahashi, T., 1996, No landward fining in a tsunami deposit from Biak, Indonesia [abstract], EOS, Transactions of the American Geophysical Union, v. 77, p. 573.

Moore, A.L., and Mohrig, D.C., 1994, Size estimate of a 1000-year-old Puget Sound tsunami [abstract], GSA Abstracts with Programs, v. 26, p. 522.

Moore, G.W., and Moore, J.G., 1988, Large-scale bedforms in boulder gravel produced by giant waves in Hawaii, Geological Society of America Special Paper 229, p. 101-110.

Moore, J.G., 1987, Subsidence of the Hawaiian Ridge, *in* Decker, R.W., Wright, T.L., and Stauffer, P.H., eds., Volcanism in Hawaii, United States Geological Survey Professional Paper 1350, p. 85-100.

Moore, J.G., Bryan, W.B., and Ludwig, K.R., 1994, Chaotic deposition by a giant wave, Molokai, Hawaii: Geological Society of America Bulletin, v. 106, p. 962-967.

Moore, J., Bryan, W., Moore, G., Moore, A., and Keating, B., 1997, Giant wave deposits, Lanai and Molokai, in Batiza, R., Lee, P., McCoy, F., eds., Field trip guide accompanying the 93rd Annual Cordilleran Section meeting, Geological Society of America, May 21-23, 1997.

Moore, J.G., and Campbell, J.F., 1987, Age of tilted reefs, Hawaii: Journal of Geophysical Research, v. 92, p. 2641-2646.

Moore, J.G., Clague, D.A., Holcomb, R.T., Lipman, P.W., Normark, W.R., and Torresan, M.E., 1989, Prodigious submarine landslides on the Hawaiian Ridge, Journal of Geophysical Research, v. 94, p. 17465-17484.

Moore, J.G., and Moore, G.W., 1984, Deposit from a giant wave on the island of Lanai, Hawaii, Science, v. 226, p. 1312-1315.

Morisawa, M., 1968, Streams: their dynamics and morphology, McGraw Hill, 175 p.

Nakata, T., and Kawana, T., 1985, Historical and prehistorical large tsunamis in the southern Ryukyus, Japan, Proceedings of the IUGG/IOC International Tsunami Symposium, p. 297-307.

Naughton, J.J., Macdonald, G.A., and Greenberg, V.A., 1980, Some additional potassium-argon ages of Hawaiian rocks: the Maui volcanic complex of Molokai, Maui, Lanai, and Kahoolawe: Journal of Volcanology and Geothermal Research, v. 7, p. 339-355.

Neumann, A.C., and Hearty, P.J., 1996, Rapid sea-level changes at the close of the last interglacial (substage 5e) recorded in Bahamian island geology, Geology, v. 24, p. 775-778.

Neumann Van Padang, M. 1930, Het Vulkaaneiland Paloeweh en de uitbarsting van den Rokatinda in 1928, Vulkanologie en Seismologie Med., v. 11, p. 1-92.

Nishimura, Y., and Miyaji, N., 1995, Tsunami deposits from the 1993 Southwest Hokkaido earthquake and the 1640 Hokkaido Komagatake eruption, Northern Japan: *in* Satake, K. and F. Imamura, eds., Tsunamis: 1992-1994, their generation, dynamics, and hazard, Birkhauser, p. 719-734.

Noji, M., Imamura, F., and Shuto, N., 1985, Numerical simulation of movement of large rocks transported by tsunamis, Proceedings of the IUGG/IOC International Tsunami Symposium, p. 189-197.

O'Brien, M.P., and Morison, J.R., 1952, The forces exerted by waves on objects, Transactions of the American Geophysical Union, v. 33, p. 32-38.

Omori, F., 1907, Note on the eruptions of the Unsendake in the 4th year of Kansei (1792), Bulletin of the Imperial Earthquake Invitational Committee, v. 1, p. 142-144.

Pararas-Carayannis, G., 1979, Tsunamis in Indonesia, Tsunami Newsletter, v. 12, p. 32.

Pinegina, T., and Bourgeois, J., 1998, Tsunami deposits and paleo-tsunami history on Peninsula Kamchatskiy (56-57°N), Kamchatka region (Bering Sea), Russia: preliminary report [abstract], EOS, Transactions of the American Geophysical Union, v. 79, p. 612.

Ramsden, J.D., 1993, Tsunamis: Forces acting on a vertical wall caused by long waves, bores, and surges on a dry bed, Report KH-R-54, California Institute of Technology, Pasadena, California, 251 p.

Reinhart, M.A., 1991, Sedimentological analysis of postulated tsunami-generated deposits from Cascadia great-subduction earthquakes along southern coastal Washington, unpublished University of Washington Department of Geological Sciences M.S. Project, 75 p.

Satake, K., Bourgeois, J., Abe, Ku., Abe, Ka., Tsuji, Y., Imamura, F., Iio, Y., Katao, H., Noguera, E., and Estrada, F., 1993, Tsunami field survey of the 1992 Nicaragua earthquake, EOS, Transactions of the American Geophysical Union, v. 74, p. 156-57.

Shackleton, N.J., and Opdyke, N.D., 1973, Oxygen isotope and palaeomagnetic stratigraphy of equatorial Pacific core V28-238: oxygen isotope temperatures and ice volumes on a 106 year scale, Quaternary Research, v. 3, p. 39-55.

Shen, M.C., and Meyer, R.E., 1963, Climb of a bore on a beach. Part 3. Run-up, Journal of Fluid Mechanics, v. 16, p. 113-125.

Shi, S., Dawson, A.G., and Smith, D.E., 1995, Coastal sedimentation associated with the December 12th, 1992 tsunami in Flores, Indonesia: *in* Satake, K., and Imamura, F., eds., Tsunamis: 1992-1994, their generation, dynamics, and hazard, Birkhauser, p. 525-536.

Shields, A., 1936, Anwendung der Aehnlichkeits-Mechanik und der Turbulenzforshung auf die Geschiebebewegung, Preussische Versuchsanstalt fur Wasserbau und Schiffbau, Heft 26.

Simkin, T., and Fiske, R.S., 1983, Krakatau 1883: the volcanic eruption and its effects, Smithsonian Press, 464 p.

Stearns, H.T., 1978, Quaternary shorelines in the Hawaiian Islands: Bernice P. Bishop Museum Bulletin 237, 57 p.

Stoker, J.J., 1948, The formation of breakers and bores, Communications on Applied Mathematics, v. 1, p. 1-87.

Watts, A.B., and ten Brink, U.S., 1989, Crustal structure, flexure, and subsidence history of the Hawaiian Islands, Journal of Geophysical Research, v. 94, p. 10473-10500.

Wiberg, P.L., and Smith, J.D., 1987, Calculations of the critical shear stress for motion of uniform and heterogeneous sediments, Water Resources Research, v. 23, p. 1471-1480.

Yamashita, B., 1995, The great Meiwa Sanriku tsunami [in Japanese], NHK, 45 p.

Yeh, H.H., Ghazali, A., and Marton, I., 1989, Experimental study of bore run-up, Journal of Fluid Mechanics, v. 206, p. 563-578.

Yeh, H.H., 1991, Tsunami bore runup, Natural Hazards, v. 4, p. 209-220.

Yeh, H., Imamura, F., Synolakis, C., Tsuji, Y., Liu, P., and Shi, S., 1993, The Flores Island tsunamis, EOS, Transactions of the American Geophysical Union, v. 74, p. 371-373.

APPENDIX A: GRAIN SIZE DATA FROM MOLOKAI, HAWAII

Grain size data from 34 sites were collected using a 5 cm by 5 cm grid. At each grid intersection I recorded the apparent long (A) and short (B) axes of the particle under the intersection, and the type of grain, either basalt or carbonate. Grains under multiple intersections were recorded multiple times, and no grain smaller than 2 mm on the long axis was recorded.

This appendix is a listing of all grain measurements recorded for Molokai: the measurements are organized by site, and labeled according to the key in Figure B-1. Each site's measurements are divided into basalt and carbonate, and arranged in descending length of A axis.

Table II: Grain size measurements from station AC.

AC				AC (Cont.)			
Carbonate		**Basalt**		**Carbonate**		**Basalt**	
A(mm)	B(mm)	A(mm)	B(mm)	A(mm)	B(mm)	A(mm)	B(mm)
80	65	218	75			22	15
52	34	194	78			22	12
49	38	192	86			20	18
45	16	192	86			19	6
42	13	140	55			18	16
34	21	113	54			18	7
30	13	104	45			17	14
30	10	100	71			17	6
28	16	82	44			16	14
25	11	75	55			16	14
23	7	73	45			16	8
18	10	73	43			15	15
16	9	72	50			15	12
15	8	64	55			15	8
14	9	58	27			13	9
13	9	57	5			12	7
12	7	45	27			10	5
11	7	41	35			9	7
10	9	35	30			8	7
10	8	35	29			7	3
10	4	35	28			5	3
9	7	35	26			5	3
9	7	35	24			3	2
7	5	35	10			3	2
7	3	32	24				
6	3	30	12				
		27	20				
		26	25				
		26	20				
		25	12				
		25	6				
		24	13				
		22	20				

Table III: Grain size measurements from station AD.

AD				AD (Cont.)			
Limestone		**Basalt**		**Limestone**		**Basalt**	
A(mm)	B(mm)	A(mm)	B(mm)	A(mm)	B(mm)	A(mm)	B(mm)
186	64	280	185	50	21		
186	64	258	107	49	33		
145	25	242	36	49	22		
138	79	237	107	48	15		
134	75	227	212	47	22		
123	86	212	140	46	14		
116	34	170	131	44	39		
109	64	119	55	44	21		
97	53	106	72	41	32		
91	29	97	76	41	24		
82	42	96	53	40	18		
80	63	76	38	40	4		
75	62	75	70	39	25		
75	62	70	67	39	9		
73	39	69	64	38	21		
70	38	67	44	38	14		
65	25	65	24	37	20		
62	20	60	45	36	18		
62	14	59	29	36	7		
60	27	56	35	35	26		
59	55	52	26	34	17		
58	26	32	11	32	17		
57	27	4	2	30	17		
56	38			30	15		
56	29			29	17		
54	50			29	16		
54	28			27	22		
53	45			27	17		
53	38			27	16		
52	28			26	17		
52	23			25	25		
50	43			25	20		
50	34			25	15		

Table III (continued)

AD (Cont.)				AD (Cont.)			
Limestone		**Basalt**		**Limestone**		**Basalt**	
A(mm)	B(mm)	A(mm)	B(mm)	A(mm)	B(mm)	A(mm)	B(mm)
24	19			9	7		
24	16			9	7		
24	14			9	4		
24	11			9	3		
23	11			7	7		
21	16			7	6		
21	12			7	6		
21	12			6	5		
20	8			6	4		
19	16			6	2		
19	10			6	2		
18	18			5	2		
17	16			4	3		
17	11			4	3		
16	11			4	2		
16	9			4	2		
16	6			3	3		
15	11			3	3		
15	7			3	2		
15	6			2	2		
14	9			2	2		
14	7						
13	11						
13	11						
12	12						
12	8						
12	4						
11	9						
11	5						
10	4						
9	8						
9	8						
9	8						

Table IV: Grain size measurements from station BA.

BA				BA (Cont.)			
Limestone		**Basalt**		**Limestone**		**Basalt**	
A(mm)	B(mm)	A(mm)	B(mm)	A(mm)	B(mm)	A(mm)	B(mm)
85	75	209	80	4	4	55	44
77	47	209	80	4	3	55	32
55	17	199	158	4	2	51	41
50	24	199	158	2	2	50	31
40	30	185	104	2	1	49	20
39	11	185	104			47	34
36	25	185	104			46	39
34	21	174	79			42	26
33	12	174	79			33	7
31	20	164	111			32	29
22	19	164	111			31	26
22	17	140	100			29	29
21	14	139	59			29	28
18	12	135	110			29	14
17	15	119	105			29	12
12	4	116	54			27	18
11	9	116	47			25	15
10	7	107	55			20	7
9	8	97	84			20	6
9	7	94	81			19	15
9	6	85	65			17	7
9	5	81	62			13	3
8	5	79	40			11	5
8	5	74	62			8	4
8	4	72	49			4	4
8	4	71	42			3	3
7	6	70	63			3	2
7	4	68	25			3	2
6	4	67	47				
6	4	66	64				
5	4	60	54				
5	3	59	44				
5	3	56	23				

Table V: Grain size measurements from station BB.

BB				BB (Cont.)			
Limestone		**Basalt**		**Limestone**		**Basalt**	
A(mm)	B(mm)	A(mm)	B(mm)	A(mm)	B(mm)	A(mm)	B(mm)
142	82	250	176	20	9	157	70
100	41	250	176	19	7	156	90
73	33	250	176	17	16	155	130
72	43	250	176	17	14	155	125
70	65	249	105	17	12	154	119
65	37	236	196	17	3	154	119
59	40	220	60	16	16	154	119
54	45	220	60	16	6	154	109
54	32	206	152	15	9	154	109
53	30	206	152	15	3	153	75
51	19	195	109	14	8	150	109
49	34	195	50	13	12	150	106
49	24	191	132	13	11	150	50
48	35	191	132	13	4	145	65
41	33	191	132	12	10	140	75
39	16	179	95	12	5	138	110
36	14	177	135	10	9	134	100
35	34	177	135	10	6	130	110
35	30	176	126	10	4	130	95
34	25	176	126	10	4	130	95
34	20	176	95	9	8	130	77
30	15	174	140	9	5	128	96
29	22	170	120	9	4	127	50
27	21	169	108	7	7	126	104
27	11	169	70	7	5	126	104
26	21	168	165	7	5	126	98
25	25	168	165	7	4	126	84
25	22	164	95	7	4	125	107
22	19	163	100	7	3	125	85
22	5	162	64	7	2	125	65
21	15	160	116	6	4	124	70
21	9	159	88	6	4	121	72
20	14	157	70	5	5	120	36

Table V (continued)

BB (Cont.)				BB (Cont.)			
Limestone		**Basalt**		**Limestone**		**Basalt**	
A(mm)	B(mm)	A(mm)	B(mm)	A(mm)	B(mm)	A(mm)	B(mm)
5	5	119	89			85	72
5	5	119	70			85	72
5	5	116	72			85	60
5	4	116	44			85	54
5	2	115	81			85	50
4	4	115	52			85	35
4	3	114	98			84	83
4	2	112	96			84	60
4	2	112	45			83	35
4	2	110	109			80	46
4	2	110	67			80	21
4	2	109	61			79	46
4	1	106	50			78	48
3	3	106	46			77	75
3	3	105	84			77	35
3	2	103	83			76	58
2	2	100	74			76	41
2	2	99	55			75	40
2	2	99	54			74	69
		96	75			74	55
		96	54			74	33
		95	90			73	30
		95	80			72	70
		94	63			72	56
		93	83			72	42
		90	90			72	25
		90	80			71	45
		90	74			70	36
		90	72			68	21
		89	80			67	66
		89	42			67	44
		88	50			66	44
		88	42			65	60

Table V (continued)

BB (Cont.)				BB (Cont.)			
Limestone		**Basalt**		**Limestone**		**Basalt**	
A(mm)	B(mm)	A(mm)	B(mm)	A(mm)	B(mm)	A(mm)	B(mm)
		65	37			52	50
		64	60			50	45
		64	36			50	33
		64	35			50	32
		64	33			50	29
		63	30			50	20
		62	42			50	18
		62	26			49	49
		61	27			49	27
		60	59			49	22
		60	50			49	17
		60	50			49	15
		60	35			47	36
		60	30			47	30
		60	19			47	24
		59	50			46	34
		59	25			45	38
		58	47			45	36
		58	41			45	30
		57	53			45	28
		56	45			42	39
		56	35			42	35
		56	34			42	30
		55	54			42	18
		55	49			41	18
		55	30			40	39
		54	49			40	31
		54	47			40	19
		54	40			39	33
		54	26			38	25
		54	21			38	24
		53	49			37	27
		52	50			37	27

Table V (continued)

BB (Cont.)				BB (Cont.)			
Limestone		**Basalt**		**Limestone**		**Basalt**	
A(mm)	B(mm)	A(mm)	B(mm)	A(mm)	B(mm)	A(mm)	B(mm)
		36	15			25	14
		35	30			25	13
		35	27			25	10
		35	25			25	9
		35	22			25	9
		35	4			25	7
		34	32			24	19
		34	25			24	18
		34	22			24	5
		34	15			22	22
		34	12			22	18
		33	29			22	15
		33	15			22	10
		33	12			22	9
		32	30			21	19
		32	12			20	18
		30	22			19	14
		29	18			18	15
		29	17			18	6
		29	16			17	14
		29	14			17	14
		29	12			17	10
		28	20			16	9
		28	15			16	4
		27	15			15	12
		26	41			15	10
		26	24			15	9
		26	19			15	6
		26	15			14	14
		25	19			14	13
		25	16			14	8
		25	15			14	7
		25	14			13	7

Table V (continued)

BB (Cont.)				BB (Cont.)			
Limestone		**Basalt**		**Limestone**		**Basalt**	
A(mm)	B(mm)	A(mm)	B(mm)	A(mm)	B(mm)	A(mm)	B(mm)
		12	9			3	3
		11	9			3	3
		10	10			2	2
		10	10				
		10	6				
		10	5				
		9	9				
		9	8				
		8	7				
		8	7				
		8	4				
		8	4				
		7	7				
		7	4				
		7	4				
		7	3				
		6	5				
		6	4				
		6	4				
		6	2				
		5	5				
		5	5				
		5	5				
		5	4				
		4	4				
		4	4				
		4	4				
		4	3				
		4	3				
		4	3				
		4	3				
		4	2				
		3	3				

Table VI: Grain size measurements from station BC.

BC				BC (Cont.)			
Carbonate		**Basalt**		**Carbonate**		**Basalt**	
A(mm)	B(mm)	A(mm)	B(mm)	A(mm)	B(mm)	A(mm)	B(mm)
19	7	510	260			270	180
4	2	510	260			270	180
4	3	510	260			264	205
4	2	510	260			264	205
2	2	510	260			254	220
2	2	510	260			250	227
2	2	510	260			250	227
2	2	494	320			250	227
2	1	494	320			250	227
		494	320			212	174
		494	320			212	174
		494	320			192	146
		494	320			192	146
		494	320			192	146
		494	320			192	146
		494	320			192	146
		494	320			179	110
		494	320			170	109
		494	320			170	109
		345	170			167	92
		345	170			167	92
		345	170			154	86
		345	170			140	124
		345	170			140	52
		345	170			128	82
		330	250			120	90
		330	250			116	86
		330	250			111	64
		275	164			106	69
		275	164			104	88
		275	164			99	60
		270	94			91	46
		270	94			80	42

Table VI (continued)

BC (Cont.)				BC (Cont.)			
Carbonate		**Basalt**		**Carbonate**		**Basalt**	
A(mm)	B(mm)	A(mm)	B(mm)	A(mm)	B(mm)	A(mm)	B(mm)
		68	40				
		59	27				
		58	47				
		58	27				
		54	28				
		52	34				
		49	17				
		44	22				
		42	9				
		40	29				
		40	5				
		28	25				
		24	18				
		22	12				
		18	9				
		13	8				
		13	7				

Table VII: Grain size measurements from station BD.

BD				BD (Cont.)			
Carbonate		**Basalt**		**Carbonate**		**Basalt**	
A(mm)	B(mm)	A(mm)	B(mm)	A(mm)	B(mm)	A(mm)	B(mm)
220	69	426	269	16	8	59	32
220	69	426	269	13	7	52	6
220	69	268	169	10	8	49	36
116	86	268	169	10	6	45	42
76	38	268	169	9	5	44	23
57	46	268	169	9	3	43	18
54	38	257	168	8	4	42	30
54	36	257	168	8	4	41	22
54	34	179	80	7	7	38	34
54	10	168	90	7	4	37	31
53	48	168	90	6	5	36	25
53	15	154	132	6	4	36	24
50	35	154	132	6	3	36	22
49	26	145	139	6	1	35	18
46	35	143	143	5	4	30	26
44	15	142	71	5	2	27	17
37	24	138	78	5	2	24	5
35	22	128	62	5	1	22	13
34	9	121	67	4	3	17	15
34	6	121	67	4	3	15	13
33	29	118	99	4	2	12	11
32	9	116	100	4	2	12	11
31	18	114	54	4	2	10	7
30	19	113	47	4	2	7	6
30	15	93	79	4	2		
24	18	90	66	3	3		
23	17	85	47	3	3		
23	17	83	32	3	3		
19	10	74	29	3	2		
19	9	74	29	3	2		
18	16	72	35	3	2		
18	15	71	41	3	2		
16	10	59	46	3	1		

Table VII (continued)

BD (Cont.)				BD (Cont.)			
Carbonate		**Basalt**		**Carbonate**		**Basalt**	
A(mm)	B(mm)	A(mm)	B(mm)	A(mm)	B(mm)	A(mm)	B(mm)
2	2						
2	1						

Table VIII: Grain size measurements from station BE.

BE				BE (Cont.)			
Carbonate		**Basalt**		**Carbonate**		**Basalt**	
A(mm)	B(mm)	A(mm)	B(mm)	A(mm)	B(mm)	A(mm)	B(mm)
152	120	710	305	19	19	165	96
152	120	710	305	19	10	165	84
116	103	385	155	19	9	162	135
92	81	385	155	19	8	162	114
76	29	385	155	18	14	149	87
75	34	385	155	18	8	146	62
70	51	340	65	17	11	145	62
58	47	300	194	15	10	135	125
57	36	300	194	14	7	135	80
44	17	290	198	14	7	135	37
43	22	290	198	14	6	128	52
40	32	290	198	14	4	124	94
40	23	290	105	13	4	123	106
40	17	280	145	12	10	114	105
38	32	280	145	12	6	110	98
36	20	280	145	12	6	110	60
33	25	230	138	11	8	106	99
33	8	230	138	10	7	105	85
30	25	230	138	10	7	104	63
29	11	230	137	10	6	99	95
25	24	219	154	10	3	99	52
25	18	219	154	9	9	96	55
25	15	205	170	9	8	95	85
24	8	205	170	9	7	95	84
24	5	179	122	9	4	90	63
23	14	176	104	9	4	87	60
23	14	176	104	8	4	87	45
22	20	175	115	7	6	85	72
22	8	175	115	7	5	84	53
21	14	175	115	7	4	84	26
21	12	170	145	6	4	82	44
20	20	170	145	6	4	80	50
20	11	166	90	6	3	78	43

Table VIII (continued)

BE (Cont.)				BE (Cont.)			
Carbonate		Basalt		Carbonate		Basalt	
A(mm)	B(mm)	A(mm)	B(mm)	A(mm)	B(mm)	A(mm)	B(mm)
5	2	76	50			35	33
4	4	75	70			34	11
4	2	74	47			34	7
4	2	74	39			30	24
3	1	74	37			28	8
3	1	73	65			26	18
3	1	71	49			25	20
3	1	70	55			24	24
2	2	70	54			24	10
2	1	70	38			22	15
		67	48			19	13
		64	43			18	12
		64	29			17	14
		62	55			14	13
		62	50			13	6
		60	38			8	7
		60	27			8	6
		60	25			8	4
		55	27			7	5
		49	30			7	5
		49	29			3	2
		48	48				
		46	20				
		45	35				
		44	35				
		44	15				
		43	27				
		42	33				
		42	27				
		40	27				
		40	17				
		37	31				
		37	25				

Table IX: Grain size measurements from station BF.

BF				BF (Cont.)			
Carbonate		**Basalt**		**Carbonate**		**Basalt**	
A(mm)	B(mm)	A(mm)	B(mm)	A(mm)	B(mm)	A(mm)	B(mm)
110	96	627	234	7	3	151	92
97	83	627	234	6	4	151	92
63	62	558	228	6	3	150	43
62	24	513	387	5	4	147	49
49	26	513	387	4	3	146	88
49	24	513	387	4	3	134	68
48	20	513	387	4	3	132	37
46	29	363	138	4	2	131	89
42	36	363	138	3	2	130	72
39	32	356	123	3	2	130	72
35	24	356	123	3	1	126	80
33	28	314	126	3	1	125	108
32	31	314	126	2	2	125	61
32	9	244	69	2	2	125	61
31	15	240	157	2	2	122	98
29	9	240	157	2	2	115	85
27	15	240	157	2	2	112	94
26	26	238	118	2	2	112	94
25	6	238	118	2	2	110	102
23	22	198	82			106	90
17	6	191	75			105	65
17	5	191	75			100	61
15	9	191	52			92	54
13	7	178	70			92	54
13	6	178	70			89	61
12	6	171	104			88	22
12	5	171	104			87	56
12	2	169	149			83	52
11	11	168	78			82	76
11	4	166	49			76	24
11	2	157	96			76	16
10	10	157	96			75	54
7	4	154	110			74	69

Table IX (continued)

BF (Cont.)				BF (Cont.)			
Carbonate		Basalt		Carbonate		Basalt	
A(mm)	B(mm)	A(mm)	B(mm)	A(mm)	B(mm)	A(mm)	B(mm)
		72	53			24	14
		68	39			23	22
		67	36			23	17
		65	29			21	23
		63	54			21	13
		59	31			21	10
		58	29			20	19
		58	21			20	15
		56	39			18	15
		56	29			17	9
		55	32			16	7
		51	24			13	6
		48	25			12	11
		43	19			12	9
		42	12			12	7
		41	30			11	5
		41	16			9	4
		39	39			9	4
		39	27			8	5
		38	29			8	3
		38	28			7	7
		38	26			6	4
		38	16			5	3
		37	16			5	2
		35	24			3	2
		34	28			3	1
		34	17				
		33	28				
		32	31				
		32	27				
		31	24				
		29	9				
		25	10				

Table X: Grain size measurements from station BG.

BG				BG (Cont.)			
Carbonate		**Basalt**		**Carbonate**		**Basalt**	
A(mm)	B(mm)	A(mm)	B(mm)	A(mm)	B(mm)	A(mm)	B(mm)
78	53	322	256	7	3	39	21
56	34	322	256	7	3	35	17
54	41	322	256	6	5	32	27
44	12	322	256	6	4	32	19
35	22	322	256	6	4	30	30
29	9	219	93	6	3	30	27
24	19	219	93	6	3	27	17
22	12	194	168	6	2	20	10
19	11	194	168	5	4	19	17
17	12	183	69	5	3	18	12
17	6	182	142	5	3	14	7
16	12	164	72	5	3	12	9
16	7	160	158	5	2	12	7
16	5	146	127	5	2	10	7
15	4	144	72	5	2	10	7
15	3	124	35	4	4	7	4
14	6	111	109	4	3	7	3
12	8	86	72	4	3		
12	4	66	24	4	3		
11	7	64	33	4	2		
11	3	56	34	4	2		
9	8	54	33	4	2		
9	6	54	14	3	2		
9	5	53	29	3	2		
9	5	46	24	3	2		
9	5	45	44	3	2		
9	3	44	25	2	2		
8	7	42	27	2	2		
8	6	41	22	2	2		
8	3	39	27	2	1		
7	5	39	27	2	1		
7	3	39	27				
7	3	39	23				

Table XI: Grain size measurements from station BH.

BH				BH (Cont.)			
Carbonate		Basalt		Carbonate		Basalt	
A(mm)	B(mm)	A(mm)	B(mm)	A(mm)	B(mm)	A(mm)	B(mm)
97	54	18	9	25	17		
93	30			25	7		
84	47			25	7		
81	69			24	10		
81	42			23	22		
80	11			23	19		
76	19			23	4		
72	45			22	14		
70	40			22	12		
63	24			22	9		
57	40			21	18		
53	17			21	17		
50	35			20	13		
49	21			20	8		
49	20			19	18		
47	21			19	12		
45	33			19	10		
43	16			19	6		
42	37			18	9		
42	19			17	11		
41	22			16	12		
41	15			15	9		
40	26			15	9		
38	27			15	5		
38	20			14	12		
37	35			14	12		
33	9			14	9		
32	20			14	9		
31	23			14	6		
28	14			13	12		
27	23			13	11		
27	7			13	9		
26	16			13	7		

Table XI (continued)

BH (Cont.)				BH (Cont.)			
Carbonate		Basalt		Carbonate		Basalt	
A(mm)	B(mm)	A(mm)	B(mm)	A(mm)	B(mm)	A(mm)	B(mm)
13	6			4	2		
13	4			4	2		
13	4			4	2		
12	11			4	2		
12	9			4	1		
12	7			3	3		
12	3			3	2		
12	3			3	2		
11	9			3	1		
11	4			2	2		
11	4			2	2		
10	9			2	2		
10	6			2	2		
10	6			2	2		
9	3			2	1		
8	5						
8	4						
8	3						
7	6						
7	6						
7	4						
7	4						
7	4						
7	3						
6	5						
6	3						
6	3						
5	4						
5	4						
5	3						
5	2						
4	3						
4	3						

Table XII: Grain size measurements from station BI.

BI				BI (Cont.)			
Carbonate		Basalt		Carbonate		Basalt	
A(mm)	B(mm)	A(mm)	B(mm)	A(mm)	B(mm)	A(mm)	B(mm)
66	25	78	60	22	12		
65	37	64	55	22	12		
65	37	43	30	22	11		
64	30	42	29	22	10		
62	55	40	24	22	8		
59	32	26	17	22	5		
52	23	24	22	21	10		
48	35	20	13	20	16		
46	25	19	11	20	10		
44	20	17	9	20	9		
42	24	17	6	20	8		
38	25	14	8	19	13		
37	28	11	6	19	13		
34	22	5	5	18	9		
34	20			18	7		
34	8			17	15		
33	24			17	14		
33	22			17	9		
33	14			16	15		
32	25			16	12		
29	12			16	10		
27	18			16	9		
27	17			16	9		
27	6			16	6		
25	9			16	6		
24	16			16	6		
24	12			15	14		
24	11			15	10		
24	10			15	10		
23	16			15	8		
22	17			14	11		
22	15			14	8		
22	12			14	6		

Table XII (continued)

BI (Cont.)				BI (Cont.)			
Carbonate		**Basalt**		**Carbonate**		**Basalt**	
A(mm)	B(mm)	A(mm)	B(mm)	A(mm)	B(mm)	A(mm)	B(mm)
14	5			7	3		
14	4			6	5		
13	11			6	4		
13	9			6	4		
13	9			6	4		
13	8			5	5		
12	9			5	4		
12	7			5	4		
12	6			5	4		
12	4			5	3		
11	7			5	3		
11	5			5	3		
11	4			5	3		
10	9			5	2		
10	6			4	2		
10	4			4	2		
9	6			4	2		
9	6			4	2		
9	5			4	2		
9	5			4	2		
9	4			4	2		
9	4			3	2		
8	5			3	1		
8	5			3	1		
8	3			2	1		
8	3			2	1		
7	6						
7	6						
7	6						
7	5						
7	4						
7	4						
7	3						

Table XIII: Grain size measurements from station BJ.

BJ				BJ (Cont.)			
Carbonate		**Basalt**		**Carbonate**		**Basalt**	
A(mm)	B(mm)	A(mm)	B(mm)	A(mm)	B(mm)	A(mm)	B(mm)
112	10	298	60	23	16	53	22
64	32	298	60	23	11	51	34
63	46	234	86	22	19	47	38
62	32	234	86	22	14	46	30
57	34	231	110	22	12	46	30
56	36	181	88	21	9	46	24
55	20	169	95	20	6	46	22
49	22	169	95	19	15	44	23
48	24	150	84	19	14	44	13
48	16	140	106	19	13	42	15
47	11	132	32	19	7	35	30
45	19	129	57	19	6	35	25
44	15	115	50	18	16	32	16
43	22	115	50	18	6	31	22
42	28	110	58	17	13	21	11
41	24	106	44	17	12	17	7
40	27	104	26	17	3	15	11
39	29	97	58	16	10	12	5
38	22	88	45	16	4	11	8
36	25	85	43	14	9	11	8
36	24	83	53	14	7	11	7
31	26	82	54	14	7	9	5
31	21	76	39	14	6	7	5
31	16	74	72	13	12	7	5
30	28	71	54	13	8	6	2
30	20	69	65	12	8	2	2
29	22	65	23	12	8		
29	16	64	62	12	7		
27	26	62	36	12	7		
27	19	62	27	12	6		
27	12	59	35	12	5		
26	23	57	40	12	4		
25	24	57	37	11	9		

Table XIII (continued)

BJ (Cont.)				BJ (Cont.)			
Carbonate		Basalt		Carbonate		Basalt	
A(mm)	B(mm)	A(mm)	B(mm)	A(mm)	B(mm)	A(mm)	B(mm)
11	6			2	2		
11	4			2	2		
11	2			2	2		
9	7			2	2		
9	4			2	2		
9	3			2	2		
8	5						
8	5						
8	5						
8	5						
7	5						
7	4						
6	5						
6	5						
6	4						
6	4						
5	5						
5	3						
5	2						
5	1						
5	1						
4	3						
4	2						
4	2						
4	2						
4	2						
4	1						
3	3						
3	2						
3	2						
3	2						
3	2						
3	1						

Table XIV: Grain size measurements from station BK.

BK				BK (Cont.)			
Carbonate		**Basalt**		**Carbonate**		**Basalt**	
A(mm)	B(mm)	A(mm)	B(mm)	A(mm)	B(mm)	A(mm)	B(mm)
84	57	622	349	13	7	92	92
34	25	622	349	12	12	90	35
33	33	418	310	12	12	85	64
29	14	364	165	12	11	81	75
28	20	364	165	12	8	81	49
27	27	276	104	12	6	79	23
26	26	249	178	12	5	68	15
26	18	249	178	11	9	67	41
25	20	249	178	11	6	66	40
23	9	228	127	11	5	65	32
21	13	228	127	11	3	63	38
20	17	203	101	11	1	62	37
19	12	185	69	10	10	60	52
19	5	184	55	10	9	57	48
19	4	184	55	10	7	56	38
19	3	184	55	10	7	47	31
18	15	178	117	10	6	47	25
18	9	178	117	10	4	46	42
18	9	172	97	9	8	42	41
17	16	172	97	9	6	38	13
17	14	168	127	9	6	36	21
17	7	166	48	9	6	35	15
16	12	156	40	9	5	33	17
15	15	144	67	9	4	32	32
15	9	136	97	9	3	32	30
15	8	136	74	8	8	31	8
15	6	132	79	8	8	30	22
15	2	128	105	8	6	30	20
14	14	126	67	8	6	28	9
14	14	126	67	8	5	27	18
14	8	123	59	8	5	27	15
13	10	114	72	7	7	24	23
13	7	100	92	7	5	22	12

Table XIV (continued)

BK (Cont.)				BK (Cont.)			
Carbonate		Basalt		Carbonate		Basalt	
A(mm)	B(mm)	A(mm)	B(mm)	A(mm)	B(mm)	A(mm)	B(mm)
7	5	15	7	3	2		
7	4	14	13	3	2		
7	3	12	5	3	2		
7	3	10	10	3	2		
6	6	9	7	3	1		
6	5	6	3	2	2		
6	4						
6	4						
6	4						
6	4						
6	4						
6	3						
6	3						
5	5						
5	5						
5	5						
5	5						
5	3						
5	3						
5	2						
5	1						
4	4						
4	3						
4	3						
4	3						
4	2						
4	2						
4	2						
4	1						
3	3						
3	3						
3	2						
3	2						

Table XV: Grain size measurements from station BL.

BL				BL (Cont.)			
Carbonate		Basalt		Carbonate		Basalt	
A(mm)	B(mm)	A(mm)	B(mm)	A(mm)	B(mm)	A(mm)	B(mm)
85	34	423	240	16	14	131	77
71	39	423	240	16	13	130	81
66	15	386	331	16	9	124	88
63	48	386	331	16	6	124	67
55	43	313	200	16	5	123	103
55	36	313	200	15	11	119	83
55	22	295	102	15	6	116	94
52	38	295	102	15	5	115	100
50	36	295	102	14	4	115	73
43	17	272	54	13	7	114	82
35	15	272	54	12	12	112	77
33	28	207	123	12	7	110	41
32	12	192	81	12	6	109	59
32	4	192	81	12	4	109	39
29	14	190	98	11	4	104	84
29	14	176	42	11	3	102	22
29	13	175	51	11	2	101	25
28	18	174	153	10	6	99	65
24	20	174	153	10	6	97	83
24	10	172	50	9	7	95	70
23	22	172	50	9	7	86	54
23	12	171	83	9	7	85	80
22	9	171	83	9	4	82	57
21	10	166	129	9	4	80	45
21	10	166	129	9	3	79	64
20	16	165	164	8	6	79	49
19	14	165	164	8	2	73	68
18	14	160	100	8	1	68	50
18	12	158	110	7	6	67	64
18	7	155	48	7	5	65	52
17	6	154	95	7	5	65	52
17	4	154	95	7	5	65	36
16	16	147	89	7	4	63	40

Table XV (continued)

BL (Cont.)				BL (Cont.)			
Carbonate		Basalt		Carbonate		Basalt	
A(mm)	B(mm)	A(mm)	B(mm)	A(mm)	B(mm)	A(mm)	B(mm)
7	4	62	57	2	2	14	7
7	4	60	52	2	1	12	10
7	4	57	44	2	1	12	10
7	1	54	30	2	1	12	9
6	5	52	35			11	4
6	5	49	21			10	8
6	4	49	11			10	5
6	4	47	30			9	6
6	4	46	24			6	5
6	4	44	20				
5	4	40	24				
5	4	39	29				
5	3	37	24				
5	2	35	22				
5	2	33	18				
5	2	33	15				
5	2	33	10				
4	3	29	20				
4	3	27	16				
4	3	26	14				
4	2	24	17				
4	2	24	15				
4	2	22	18				
4	1	20	20				
3	3	20	16				
3	2	19	15				
3	2	18	18				
3	1	18	18				
3	1	18	7				
3	1	17	10				
2	2	15	8				
2	2	15	7				
2	2	15	7				

Table XVI: Grain size measurements from station BM.

BM				BM (Cont.)			
Carbonate		**Basalt**		**Carbonate**		**Basalt**	
A(mm)	B(mm)	A(mm)	B(mm)	A(mm)	B(mm)	A(mm)	B(mm)
38	17	182	169	10	7	44	26
32	24	182	169	10	6	42	12
30	27	154	94	10	6	42	10
28	14	135	111	10	5	38	16
26	17	130	52	10	5	37	24
24	8	124	78	10	5	36	12
22	20	114	96	10	5	34	34
21	14	101	60	10	4	32	14
19	17	96	80	10	2	31	15
19	4	92	41	9	7	30	27
18	7	86	74	9	6	30	25
17	14	76	49	9	5	29	15
17	10	75	21	9	4	28	20
17	4	72	61	9	2	28	15
15	15	72	44	9	2	27	12
15	11	71	20	9	1	26	20
15	10	70	34	8	7	24	12
15	8	64	38	8	5	20	14
15	8	62	45	8	2	20	13
14	12	62	42	7	7	20	12
14	12	58	46	7	5	19	16
14	10	56	32	7	5	19	16
14	9	54	45	7	5	19	11
14	8	54	44	7	5	19	10
14	4	50	42	7	3	19	9
13	10	50	36	7	2	17	15
13	7	50	23	7	2	16	13
12	8	49	38	7	1	16	12
12	7	49	30	7	1	16	11
12	6	48	33	6	6	16	7
12	5	48	26	6	5	15	14
11	9	48	24	6	3	15	10
11	8	44	36	6	2	15	9

Table XVI (continued)

BM (Cont.)				BM (Cont.)			
Carbonate		Basalt		Carbonate		Basalt	
A(mm)	B(mm)	A(mm)	B(mm)	A(mm)	B(mm)	A(mm)	B(mm)
6	2	15	8	1	1		
6	1	15	7	1	1		
6	1	14	9				
6	1	14	8				
5	4	14	5				
5	4	13	12				
5	3	13	10				
5	3	9	6				
5	3	9	4				
5	3	5	3				
5	2	5	3				
5	2	4	3				
5	2	4	2				
5	2						
4	4						
4	4						
4	3						
4	3						
4	3						
4	3						
3	3						
3	2						
3	2						
2	2						
2	2						
2	2						
2	1						
2	1						
2	1						
2	1						
2	1						
2	1						
1	1						

Table XVII: Grain size measurements from station BN.

BN				BN (Cont.)			
Carbonate		**Basalt**		**Carbonate**		**Basalt**	
A(mm)	B(mm)	A(mm)	B(mm)	A(mm)	B(mm)	A(mm)	B(mm)
24	15	234	175			24	20
23	16	234	175			24	19
12	6	234	175			24	14
11	4	135	116			22	12
10	9	135	116			20	6
10	6	135	57			18	12
7	6	93	65			17	12
6	2	90	68			16	9
6	1	82	44			14	6
5	4	77	59			12	10
5	3	76	54			11	5
5	2	75	68			11	4
5	2	74	72			10	9
5	1	69	37			8	6
4	3	64	17			7	7
4	3	62	51			7	4
4	2	61	46			7	3
3	3	58	44			6	5
3	3	52	14			6	4
3	3	51	36			5	3
3	2	50	44			4	3
3	1	47	40				
2	2	47	34				
2	2	44	29				
2	2	40	30				
2	2	39	23				
2	2	34	34				
2	2	28	18				
2	1	27	6				
2	1	26	20				
2	1	26	19				
2	1	25	22				
2	1	25	10				

Table XVIII: Grain size measurements from station BO.

BO				BO (Cont.)			
Carbonate		Basalt		Carbonate		Basalt	
A(mm)	B(mm)	A(mm)	B(mm)	A(mm)	B(mm)	A(mm)	B(mm)
66	42	185	136	22	3		
66	13	100	72	21	9		
61	42	92	73	21	8		
59	33	87	62	20	16		
58	29	84	52	20	9		
57	34	76	56	20	9		
57	28	54	45	20	8		
55	44	50	26	20	5		
51	36	48	27	19	14		
48	28	44	44	19	12		
47	15	39	25	19	12		
44	42	22	15	19	11		
42	21	22	14	18	14		
42	11	18	13	18	9		
40	10	16	15	18	9		
39	13	16	9	18	5		
38	12	10	7	16	7		
37	25	8	6	16	7		
36	24	7	5	16	7		
35	14	6	5	16	5		
32	20	2	2	16	4		
29	9			15	10		
28	23			15	5		
27	17			14	12		
27	11			14	10		
26	10			14	9		
25	20			13	12		
25	10			13	8		
25	9			13	5		
24	17			13	3		
23	9			11	6		
22	14			11	5		
22	7			11	5		

Table XVIII (continued)

BO (Cont.)				BO (Cont.)			
Carbonate		Basalt		Carbonate		Basalt	
A(mm)	B(mm)	A(mm)	B(mm)	A(mm)	B(mm)	A(mm)	B(mm)
11	4			4	3		
11	3			4	2		
11	2			4	2		
10	7			3	2		
10	6			3	2		
10	6			3	1		
10	5			2	2		
10	5			2	2		
10	4			2	2		
9	7			2	2		
9	6			1	1		
9	6						
9	6						
9	3						
8	7						
8	5						
8	4						
8	4						
8	1						
7	5						
7	5						
7	4						
7	4						
6	5						
6	4						
6	3						
6	2						
5	4						
5	4						
5	3						
5	3						
5	3						
5	3						

Table XIX: Grain size measurements from station BP.

BP				BP (Cont.)			
Carbonate		**Basalt**		**Carbonate**		**Basalt**	
A(mm)	B(mm)	A(mm)	B(mm)	A(mm)	B(mm)	A(mm)	B(mm)
84	35	162	84	16	11		
80	24	162	84	16	9		
80	15	142	105	16	6		
72	15	111	68	15	6		
63	39	95	83	15	2		
51	38	87	85	14	14		
50	32	67	40	14	12		
45	17	50	27	14	7		
40	18	44	34	13	9		
38	34	43	30	13	5		
38	20	35	26	13	4		
38	6	34	16	13	4		
37	21	33	25	12	10		
34	16	22	15	12	4		
32	19	16	12	11	6		
31	6	16	11	11	6		
27	14	8	8	11	5		
27	11	8	5	11	4		
27	10	5	3	11	3		
26	14	4	2	11	2		
25	15	3	2	10	8		
25	9	3	2	9	8		
24	18	2	2	9	7		
22	18			9	5		
22	14			9	4		
22	8			9	3		
20	12			8	7		
19	18			8	4		
19	16			8	3		
18	11			8	3		
17	9			7	6		
17	5			7	5		
16	14			7	1		

Table XIX (continued)

BP (Cont.)				BP (Cont.)			
Carbonate		Basalt		Carbonate		Basalt	
A(mm)	B(mm)	A(mm)	B(mm)	A(mm)	B(mm)	A(mm)	B(mm)
6	4			2	1		
6	4						
5	4						
5	3						
5	2						
5	1						
4	3						
4	2						
4	2						
4	2						
4	2						
4	1						
4	1						
3	3						
3	3						
3	2						
3	2						
3	2						
3	2						
3	2						
3	2						
3	1						
2	2						
2	2						
2	2						
2	2						
2	1						
2	1						
2	1						
2	1						
2	1						
2	1						
2	1						

Table XX: Grain size measurements from station BR.

BR				BR (Cont.)			
Carbonate		Basalt		Carbonate		Basalt	
A(mm)	B(mm)	A(mm)	B(mm)	A(mm)	B(mm)	A(mm)	B(mm)
101	20	259	184	19	8	51	44
93	34	259	184	19	4	43	37
64	18	259	184	18	10	40	16
60	17	259	184	17	11	38	32
45	8	243	160	16	16	34	24
44	24	243	160	16	14	32	26
42	26	243	160	16	9	32	25
38	30	243	160	16	7	32	20
36	27	243	160	14	13	30	24
36	18	243	160	14	8	30	12
34	7	225	135	14	5	29	27
32	23	179	100	12	9	28	21
32	9	179	100	12	8	27	12
31	20	158	47	12	4	26	12
31	18	131	85	11	7	26	9
31	11	131	85	11	6	25	12
30	17	122	119	10	7	24	13
30	16	122	43	10	2	23	16
30	9	116	83	9	9	22	11
28	18	103	66	9	8	21	17
28	15	102	68	9	6	21	6
27	17	94	72	9	6	19	18
26	24	94	62	9	4	18	10
26	13	93	45	9	4	17	9
23	19	87	60	9	4	16	7
23	11	79	51	9	3	15	15
22	9	70	48	8	7	15	4
22	8	70	40	8	5	14	7
20	9	65	41	7	7	12	7
19	12	62	51	7	6	11	8
19	10	62	45	7	5	11	8
19	9	59	20	7	5	9	6
19	8	52	27	7	4	7	6

Table XX (continued)

BR (Cont.)				BR (Cont.)			
Carbonate		Basalt		Carbonate		Basalt	
A(mm)	B(mm)	A(mm)	B(mm)	A(mm)	B(mm)	A(mm)	B(mm)
7	3	4	3	2	1		
7	3			2	1		
7	3						
7	3						
6	5						
6	4						
6	4						
6	3						
6	3						
6	3						
6	2						
6	2						
6	2						
5	4						
5	3						
5	3						
5	2						
5	2						
4	3						
4	3						
4	3						
4	3						
4	2						
4	2						
3	2						
3	2						
3	2						
3	1						
3	1						
2	2						
2	2						
2	2						
2	1						

Table XXI: Grain size measurements from station BS.

BS				BS (Cont.)			
Carbonate		**Basalt**		**Carbonate**		**Basalt**	
A(mm)	B(mm)	A(mm)	B(mm)	A(mm)	B(mm)	A(mm)	B(mm)
116	34	436	405	22	14	32	11
83	50	221	125	21	5	28	13
65	40	213	132	18	17	21	15
61	24	213	132	17	12	14	10
55	19	206	125	17	11	14	7
54	41	159	82	16	11	12	11
54	40	152	131	16	10	12	9
53	24	139	119	16	8	9	4
52	12	137	95	16	7	4	2
51	32	136	99	15	13		
49	23	129	90	15	4		
44	32	119	110	14	14		
42	31	119	110	14	13		
41	33	114	73	14	9		
36	17	102	60	14	4		
36	16	99	57	13	13		
36	9	89	49	13	3		
35	22	85	44	12	11		
35	12	81	23	12	9		
31	17	79	70	12	8		
30	14	77	43	12	6		
29	22	72	57	12	3		
29	13	67	54	11	5		
28	21	66	56	11	5		
25	25	65	50	10	7		
25	23	58	35	10	6		
25	14	57	26	10	5		
25	13	55	25	10	5		
24	19	52	32	10	4		
24	14	52	32	10	4		
24	10	41	35	9	5		
23	15	35	35	9	4		
22	20	35	21	8	8		

Table XXI (continued)

BS (Cont.)				BS (Cont.)			
Carbonate		**Basalt**		**Carbonate**		**Basalt**	
A(mm)	B(mm)	A(mm)	B(mm)	A(mm)	B(mm)	A(mm)	B(mm)
8	4			2	2		
7	6			2	2		
7	6			2	2		
7	4			2	1		
7	4			2	1		
7	3			2	1		
7	3			2	1		
7	2						
6	6						
6	5						
6	4						
6	4						
6	3						
6	2						
5	4						
5	3						
5	3						
5	2						
5	2						
5	2						
5	1						
5	1						
4	4						
4	2						
4	2						
4	2						
4	2						
3	3						
3	3						
3	2						
3	2						
3	2						
3	1						

Table XXII: Grain size measurements from station BT.

BT				BT (Cont.)			
Carbonate		**Basalt**		**Carbonate**		**Basalt**	
A(mm)	B(mm)	A(mm)	B(mm)	A(mm)	B(mm)	A(mm)	B(mm)
88	60	354	129	19	7		
51	25	66	55	18	6		
48	17	24	16	18	6		
42	33	20	15	18	4		
41	24	18	10	17	14		
40	21	11	9	17	11		
36	22	9	3	16	16		
35	13	8	5	16	7		
34	14	8	3	16	6		
34	10	6	4	16	4		
33	18	6	3	15	9		
32	13	4	3	15	7		
31	12	3	2	14	8		
29	17			12	11		
28	13			12	8		
27	13			12	7		
26	13			12	5		
26	12			11	10		
24	16			11	8		
24	15			11	6		
21	15			11	5		
21	14			10	8		
21	8			10	6		
20	12			10	5		
20	8			10	4		
20	8			10	3		
19	16			9	7		
19	14			8	6		
19	12			8	4		
19	11			8	1		
19	9			7	7		
19	7			7	6		
19	7			7	4		

Table XXII (continued)

BT (Cont.)				BT (Cont.)			
Carbonate		**Basalt**		**Carbonate**		**Basalt**	
A(mm)	B(mm)	A(mm)	B(mm)	A(mm)	B(mm)	A(mm)	B(mm)
7	4			1	1		
7	3						
7	3						
7	3						
7	1						
6	5						
6	4						
6	4						
6	4						
6	3						
5	5						
5	3						
5	3						
5	3						
5	3						
5	2						
5	2						
5	2						
5	1						
4	3						
4	2						
4	2						
4	2						
4	2						
4	2						
4	1						
3	2						
3	2						
3	1						
2	2						
2	2						
2	1						
2	1						

Table XXIII: Grain size measurements from station BU.

BU				BU (Cont.)			
Carbonate		**Basalt**		**Carbonate**		**Basalt**	
A(mm)	B(mm)	A(mm)	B(mm)	A(mm)	B(mm)	A(mm)	B(mm)
96	46	125	68	24	13		
87	37	58	38	24	7		
55	33	45	33	22	13		
52	22	36	22	22	12		
51	31	31	29	22	8		
47	21	27	12	21	18		
47	14	23	16	20	11		
46	27	18	5	20	9		
44	10	14	9	19	10		
39	25	14	8	19	8		
39	17	13	7	18	8		
37	20	10	8	17	15		
35	17	6	6	17	12		
35	10	6	4	17	6		
34	26	6	4	16	9		
34	13	5	4	14	7		
34	10	3	2	14	6		
33	17	3	2	13	12		
31	20	2	2	13	11		
31	20			13	7		
30	26			12	4		
30	26			11	8		
30	16			11	5		
30	12			11	4		
29	22			11	4		
29	21			10	5		
27	14			10	5		
27	10			9	6		
26	25			9	6		
26	16			9	5		
26	16			9	4		
25	21			9	3		
25	21			8	7		

Table XXIII (continued)

BU (Cont.)				BU (Cont.)			
Carbonate		Basalt		Carbonate		Basalt	
A(mm)	B(mm)	A(mm)	B(mm)	A(mm)	B(mm)	A(mm)	B(mm)
8	6			2	2		
8	6			2	1		
8	4						
8	4						
7	5						
7	4						
7	2						
6	6						
6	5						
6	5						
6	3						
6	1						
5	4						
5	4						
5	4						
5	3						
5	2						
5	2						
4	4						
4	3						
4	3						
4	3						
4	2						
4	1						
3	3						
3	3						
3	1						
3	1						
2	2						
2	2						
2	2						
2	2						
2	2						

Table XXIV: Grain size measurements from station BV.

BV				BV (Cont.)			
Carbonate		**Basalt**		**Carbonate**		**Basalt**	
A(mm)	B(mm)	A(mm)	B(mm)	A(mm)	B(mm)	A(mm)	B(mm)
50	30	64	26	15	3		
31	22	55	27	14	13		
28	4	42	28	14	7		
27	19	22	14	12	10		
27	10	20	12	11	5		
26	22			11	3		
26	12			10	5		
25	12			10	5		
24	19			10	3		
24	15			10	2		
24	9			9	6		
24	5			9	6		
23	8			9	5		
23	5			9	5		
21	13			9	5		
21	11			9	4		
20	5			9	3		
19	16			8	5		
19	6			8	5		
19	3			8	5		
18	10			8	5		
18	5			8	4		
17	14			7	5		
17	14			7	4		
17	12			7	4		
17	12			7	4		
17	9			7	3		
17	7			7	3		
16	12			7	3		
15	9			7	3		
15	9			7	2		
15	5			6	5		
15	5			6	4		

Table XXIV (continued)

BV (Cont.)				BV (Cont.)			
Carbonate		Basalt		Carbonate		Basalt	
A(mm)	B(mm)	A(mm)	B(mm)	A(mm)	B(mm)	A(mm)	B(mm)
6	4			2	2		
6	4			2	2		
6	4			2	1		
6	4			2	1		
6	3			2	1		
6	3			1	1		
6	3			1	1		
6	2						
6	2						
5	5						
5	5						
5	4						
5	3						
5	3						
5	3						
5	3						
5	3						
5	2						
5	2						
5	2						
5	2						
5	2						
5	1						
4	4						
4	2						
4	2						
4	2						
4	2						
3	2						
3	2						
3	2						
3	2						
2	2						

Table XXV: Grain size measurements from station BW.

BW				BW (Cont.)			
Carbonate		**Basalt**		**Carbonate**		**Basalt**	
A(mm)	B(mm)	A(mm)	B(mm)	A(mm)	B(mm)	A(mm)	B(mm)
71	25	256	119	15	4		
54	24	256	119	14	6		
54	18	256	119	13	10		
50	29	129	98	13	9		
39	15	91	89	13	8		
35	17	82	50	13	6		
32	21	79	47	13	5		
32	17	68	37	12	8		
32	14	65	45	12	8		
30	19	61	48	12	8		
30	15	58	46	12	7		
26	16	55	42	12	6		
25	15	43	20	12	6		
25	14	32	31	12	5		
21	19	24	11	12	4		
21	10	20	12	11	6		
21	5	17	11	11	6		
20	17	14	4	10	10		
20	11	11	6	10	9		
20	5	10	7	10	8		
20	1	7	6	10	7		
18	15	5	2	10	5		
18	12			10	2		
18	8			9	7		
17	14			9	5		
17	13			9	5		
17	12			9	5		
17	2			9	4		
16	15			8	7		
16	12			8	6		
16	8			8	5		
16	5			8	4		
15	14			8	4		

Table XXV (continued)

BW (Cont.)				BW (Cont.)			
Carbonate		Basalt		Carbonate		Basalt	
A(mm)	B(mm)	A(mm)	B(mm)	A(mm)	B(mm)	A(mm)	B(mm)
8	3			2	2		
8	3			2	2		
8	2						
7	6						
7	5						
7	4						
7	3						
6	5						
6	5						
6	4						
6	4						
6	4						
6	3						
6	3						
6	3						
5	5						
5	4						
5	4						
5	4						
5	4						
5	4						
5	3						
5	3						
5	3						
5	3						
5	2						
5	2						
4	3						
4	3						
4	2						
4	2						
3	2						
3	2						

Table XXVI: Grain size measurements from station BX.

BX				BX (Cont.)			
Carbonate		**Basalt**		**Carbonate**		**Basalt**	
A(mm)	B(mm)	A(mm)	B(mm)	A(mm)	B(mm)	A(mm)	B(mm)
103	34	428	302	22	13		
91	38	428	302	21	16		
70	55	428	302	16	2		
63	26	342	190	15	11		
61	26	342	190	15	7		
60	20	342	190	14	9		
57	42	342	190	14	5		
53	29	342	190	13	3		
52	26	268	88	11	10		
49	18	268	88	11	7		
41	16	249	138	11	5		
40	33	249	138	10	4		
36	26	176	128	10	3		
36	22	176	128	9	7		
36	12	176	126	9	6		
35	20	149	67	9	6		
34	12	147	68	9	5		
32	16	98	67	9	4		
30	27	95	56	9	4		
30	13	68	46	8	6		
29	29	48	42	8	3		
29	18	47	23	8	3		
28	26	39	37	7	4		
27	12	36	15	7	4		
26	26	27	16	7	4		
26	20	25	16	6	4		
26	10	25	16	6	3		
24	10	11	7	6	2		
24	10	11	7	5	4		
24	8	10	9	5	3		
23	17	8	3	5	3		
23	15	4	1	5	3		
23	12	3	1	5	3		

Table XXVI (continued)

BX (Cont.)				BX (Cont.)			
Carbonate		**Basalt**		**Carbonate**		**Basalt**	
A(mm)	B(mm)	A(mm)	B(mm)	A(mm)	B(mm)	A(mm)	B(mm)
5	2			2	1		
5	2			2	1		
5	2						
4	3						
4	3						
4	3						
4	3						
4	2						
4	2						
4	2						
4	2						
4	2						
4	1						
4	1						
4	1						
4	1						
3	3						
3	2						
3	2						
3	2						
3	2						
3	2						
3	1						
3	1						
2	2						
2	2						
2	2						
2	1						
2	1						
2	1						
2	1						
2	1						
2	1						

Table XXVII: Grain size measurements from station BY.

BY				BY (Cont.)			
Carbonate		Basalt		Carbonate		Basalt	
A(mm)	B(mm)	A(mm)	B(mm)	A(mm)	B(mm)	A(mm)	B(mm)
81	64	445	215	27	12	153	142
77	35	285	232	26	12	153	50
72	65	285	232	25	20	152	138
70	64	285	232	25	15	152	138
69	23	281	195	25	7	148	96
65	22	281	195	24	15	145	66
63	34	281	195	24	15	135	118
60	18	281	195	24	14	134	95
55	24	248	181	24	12	120	84
52	49	248	181	24	4	100	95
51	34	248	181	23	12	92	86
49	23	240	232	22	20	90	44
45	33	240	232	22	8	85	74
45	25	240	232	21	17	85	44
44	30	240	232	21	12	78	53
44	22	232	184	21	5	75	68
40	21	232	184	20	14	65	35
39	33	232	184	20	12	62	30
36	17	232	184	20	9	56	43
36	4	230	175	20	6	49	39
35	30	221	160	19	15	46	38
35	20	221	160	19	11	44	26
35	20	221	160	16	15	44	25
35	14	201	157	16	7	36	25
34	33	201	157	15	15	35	22
33	17	201	157	15	10	34	22
32	16	166	142	15	6	26	8
30	15	166	142	14	10	20	20
30	10	166	142	14	8	19	10
29	29	166	98	13	10	16	3
29	22	164	90	13	7	14	5
28	12	161	119	13	5	4	2
27	16	160	156	12	11	3	2

Table XXVII (continued)

BY (Cont.)				BY (Cont.)			
Carbonate		Basalt		Carbonate		Basalt	
A(mm)	B(mm)	A(mm)	B(mm)	A(mm)	B(mm)	A(mm)	B(mm)
12	10			5	3		
12	9			5	2		
12	7			4	2		
12	5			4	2		
12	4			4	2		
11	8			3	2		
10	9			2	2		
10	6			1	1		
10	6						
10	5						
10	3						
10	3						
10	2						
10	2						
9	8						
9	6						
9	5						
9	3						
9	3						
8	8						
8	6						
8	5						
8	4						
7	4						
7	2						
7	2						
6	4						
6	3						
6	3						
6	2						
5	4						
5	4						
5	4						

Table XXVIII: Grain size measurements from station BZ.

BZ				BZ (Cont.)			
Carbonate		Basalt		Carbonate		Basalt	
A(mm)	B(mm)	A(mm)	B(mm)	A(mm)	B(mm)	A(mm)	B(mm)
140	48	634	374	31	9	240	66
111	47	634	374	29	16	202	85
87	32	634	374	28	23	202	85
78	40	634	374	28	10	174	82
73	46	372	184	27	24	160	113
72	52	372	184	27	15	159	124
71	34	372	184	27	14	159	124
68	15	364	290	27	10	156	92
65	60	364	290	26	14	156	92
59	58	364	290	26	7	134	103
55	34	364	290	25	15	130	104
55	24	364	290	25	15	116	108
54	49	364	290	25	7	115	78
54	24	364	290	24	17	115	73
52	45	364	290	24	15	108	98
51	30	364	290	24	14	101	71
49	31	364	290	24	14	98	48
47	23	364	290	22	19	98	33
46	32	285	197	22	19	84	60
45	32	285	197	22	9	77	68
44	22	285	197	21	12	77	58
42	28	285	197	21	8	72	50
41	17	285	197	20	17	61	42
41	16	281	144	20	15	56	55
40	31	281	144	20	14	36	17
38	29	278	183	20	14	26	18
37	23	278	183	20	11	24	21
37	15	278	183	20	5	24	15
36	30	278	183	19	10	24	12
36	28	248	151	19	10	23	14
36	25	248	151	19	8	15	8
33	20	248	151	18	17	10	7
32	29	240	66	17	6	8	6

Table XXVIII (continued)

BZ (Cont.)				BZ (Cont.)			
Carbonate		**Basalt**		**Carbonate**		**Basalt**	
A(mm)	B(mm)	A(mm)	B(mm)	A(mm)	B(mm)	A(mm)	B(mm)
16	6	6	4	2	2		
15	13	6	3	2	1		
14	5	2	2	2	1		
13	12						
13	10						
13	4						
13	3						
12	7						
11	11						
11	8						
11	7						
11	7						
11	7						
10	9						
10	9						
10	8						
9	7						
9	4						
9	2						
8	4						
8	3						
7	4						
7	4						
7	2						
7	2						
6	4						
6	3						
5	5						
4	2						
4	2						
3	2						
3	1						
2	2						

Table XXIX: Grain size measurements from station Bα.

Bα				Bα (Cont.)			
Carbonate		**Basalt**		**Carbonate**		**Basalt**	
A(mm)	B(mm)	A(mm)	B(mm)	A(mm)	B(mm)	A(mm)	B(mm)
95	44	222	97	24	15		
88	56	165	123	24	14		
78	29	94	67	23	14		
76	45	85	75	22	16		
74	57	77	66	22	6		
70	40	76	35	21	20		
60	30	65	61	21	8		
58	14	58	39	20	11		
57	28	46	30	20	10		
54	30	34	7	18	9		
54	22	27	15	17	14		
52	19	26	11	17	12		
52	14	23	19	17	10		
50	36	17	16	16	14		
49	22	6	5	16	6		
44	9	5	3	15	13		
42	17			15	11		
41	32			15	11		
41	32			15	7		
39	34			15	5		
36	14			14	14		
34	2			14	14		
32	10			14	10		
31	22			14	4		
31	15			13	12		
29	7			13	11		
28	20			13	7		
28	11			12	7		
26	20			12	6		
25	18			11	6		
25	2			10	7		
24	19			10	3		
24	17			9	5		

Table XXIX (continued)

Bα (Cont.)				Bα (Cont.)			
Carbonate		**Basalt**		**Carbonate**		**Basalt**	
A(mm)	B(mm)	A(mm)	B(mm)	A(mm)	B(mm)	A(mm)	B(mm)
8	5						
8	4						
8	4						
7	5						
7	4						
6	4						
6	3						
6	2						
5	4						
5	4						
3	2						
2	1						
2	1						
1	1						

Table XXX: Grain size measurements from station Bβ.

Bβ				Bβ (Cont.)			
Carbonate		**Basalt**		**Carbonate**		**Basalt**	
A(mm)	B(mm)	A(mm)	B(mm)	A(mm)	B(mm)	A(mm)	B(mm)
47	12	512	321	8	4	114	61
43	16	512	321	8	4	113	89
41	18	417	297	8	3	113	89
37	29	417	297	8	3	112	98
28	12	281	230	8	3	112	76
27	12	259	238	7	6	112	76
26	10	243	139	7	5	110	85
24	16	243	139	7	4	110	48
21	12	237	214	7	4	108	68
19	6	237	214	7	4	107	65
18	10	237	214	7	4	104	82
17	3	237	214	7	4	104	23
16	5	221	146	7	4	99	92
15	7	205	43	7	4	98	70
14	5	198	96	7	3	97	29
13	8	198	96	7	3	94	53
13	6	179	116	7	3	93	82
12	11	172	88	7	2	93	58
12	10	160	116	7	2	92	38
11	4	160	116	6	4	90	82
11	2	160	116	6	4	90	29
10	6	157	100	6	2	87	72
10	4	152	50	6	1	86	84
9	6	134	90	5	4	86	64
9	3	133	98	5	4	84	52
8	8	133	49	5	3	81	46
8	7	132	102	5	3	81	38
8	6	132	62	5	3	80	33
8	6	132	62	5	3	79	41
8	5	126	61	5	2	76	54
8	4	125	85	5	1	75	65
8	4	120	105	5	1	75	60
8	4	117	76	4	3	72	37

Table XXX (continued)

Bβ (Cont.)				Bβ (Cont.)			
Carbonate		**Basalt**		**Carbonate**		**Basalt**	
A(mm)	B(mm)	A(mm)	B(mm)	A(mm)	B(mm)	A(mm)	B(mm)
4	2	70	65	1	1	34	7
4	2	70	55			33	24
4	2	67	63			32	22
4	2	66	26			32	5
4	2	62	53			29	25
4	1	61	26			27	25
4	1	60	44			27	24
3	3	59	19			27	22
3	3	58	58			27	14
3	3	58	44			27	12
3	3	56	40			27	12
3	2	56	37			27	11
3	2	56	34			26	10
3	2	56	22			24	18
3	1	55	32			23	16
3	1	55	25			22	15
2	2	51	43			21	12
2	2	51	26			20	14
2	2	50	24			19	12
2	2	49	36			19	10
2	2	49	14			17	12
2	2	49	1			17	6
2	2	48	16			16	14
2	1	47	26			16	10
2	1	47	22			16	10
2	1	45	26			15	12
2	1	44	22			15	6
2	1	39	32			12	12
2	1	38	28			10	7
2	1	38	28			10	7
2	1	38	14			10	6
2	1	37	21			7	4
1	1	36	18			5	3

Table XXX (continued)

Bβ (Cont.)				Bβ (Cont.)			
Carbonate		**Basalt**		**Carbonate**		**Basalt**	
A(mm)	B(mm)	A(mm)	B(mm)	A(mm)	B(mm)	A(mm)	B(mm)
		5	2				
		4	3				
		2	1				

Table XXXI: Grain size measurements from station CA.

CA				CA (Cont.)			
Carbonate		**Basalt**		**Carbonate**		**Basalt**	
A(mm)	B(mm)	A(mm)	B(mm)	A(mm)	B(mm)	A(mm)	B(mm)
22	10	236	96	1	1	110	55
17	8	236	96	1	1	106	100
15	9	192	173	1	1	105	92
11	5	192	173	1	1	104	55
10	4	184	109	1	1	94	66
9	3	168	129	1	1	94	57
8	4	168	129	1	1	92	80
7	3	168	129			92	21
7	3	166	62			89	62
7	3	164	147			89	51
7	2	164	147			86	50
6	4	161	116			85	39
6	3	159	105			84	58
5	3	156	150			83	42
5	3	156	150			82	64
5	2	154	96			80	67
4	2	147	114			80	55
4	2	147	114			80	43
3	2	147	101			80	38
3	1	144	83			79	32
2	2	144	83			77	34
2	2	135	56			75	52
2	2	130	55			74	40
2	2	129	127			73	72
2	1	129	77			73	29
2	1	128	49			71	57
2	1	125	114			68	29
2	1	121	75			68	28
2	1	120	55			68	21
1	1	117	81			67	59
1	1	117	81			67	44
1	1	115	77			67	32
1	1	112	72			66	34

Table XXXI (continued)

CA (Cont.)				CA (Cont.)			
Carbonate		**Basalt**		**Carbonate**		**Basalt**	
A(mm)	B(mm)	A(mm)	B(mm)	A(mm)	B(mm)	A(mm)	B(mm)
		65	23			25	18
		64	26			25	17
		63	32			25	4
		60	24			24	17
		57	40			23	19
		57	30			23	18
		54	43			22	8
		53	50			21	17
		52	27			20	18
		51	34			20	13
		50	49			17	16
		49	40			17	16
		49	35			16	12
		46	32			16	8
		42	40			15	9
		42	36			12	8
		42	31			12	4
		42	30			2	2
		42	30				
		42	26				
		41	26				
		40	22				
		40	10				
		37	30				
		35	28				
		35	25				
		35	19				
		30	19				
		29	11				
		29	8				
		27	15				
		27	11				
		25	19				

Table XXXII: Grain size measurements from station CB.

CB				CB (Cont.)			
Carbonate		**Basalt**		**Carbonate**		**Basalt**	
A(mm)	B(mm)	A(mm)	B(mm)	A(mm)	B(mm)	A(mm)	B(mm)
38	25	181	105				
31	20	152	72				
30	14	102	86				
18	8	97	90				
16	7	74	45				
11	9	72	45				
11	5	65	12				
6	5	64	60				
6	4	61	15				
5	4	51	24				
3	3	34	29				
2	1	22	21				
1	1	19	16				
1	1	10	6				
1	1						

Table XXXIII: Grain size measurements from station CC.

CC				CC (Cont.)			
Carbonate		**Basalt**		**Carbonate**		**Basalt**	
A(mm)	B(mm)	A(mm)	B(mm)	A(mm)	B(mm)	A(mm)	B(mm)
120	56	109	52	29	24		
103	59	85	67	29	17		
88	37	52	43	26	16		
87	25	50	44	26	11		
81	66	46	40	25	24		
79	35	44	32	25	11		
74	48	44	20	25	11		
73	52	38	29	24	11		
66	46	29	21	23	8		
64	32	28	17	23	7		
59	34	24	9	22	21		
57	52	23	17	22	20		
57	50	20	13	22	19		
52	46	20	13	22	8		
50	41	18	12	21	16		
47	11	14	10	21	16		
47	11	14	7	21	12		
44	28	12	7	19	17		
44	26	8	7	19	16		
43	35	3	3	19	14		
42	18			19	12		
41	23			18	11		
38	28			18	9		
38	27			17	16		
38	18			17	16		
37	21			17	10		
36	34			16	7		
36	14			16	6		
36	14			15	9		
35	29			14	8		
34	26			14	8		
32	19			13	8		
31	28			13	8		

Table XXXIII (continued)

CC (Cont.)				CC (Cont.)			
Carbonate		**Basalt**		**Carbonate**		**Basalt**	
A(mm)	B(mm)	A(mm)	B(mm)	A(mm)	B(mm)	A(mm)	B(mm)
13	7						
12	9						
12	7						
12	7						
12	6						
11	4						
11	3						
10	10						
10	5						
9	9						
9	7						
9	6						
9	6						
9	4						
8	5						
8	4						
7	4						
7	4						
6	4						
6	3						
3	2						
2	2						
2	2						
2	1						

Table XXXIV: Grain size measurements from station CD.

CD				CD (Cont.)			
Carbonate		Basalt		Carbonate		Basalt	
A(mm)	B(mm)	A(mm)	B(mm)	A(mm)	B(mm)	A(mm)	B(mm)
67	39	237	174	19	11		
57	33	226	158	19	8		
53	50	175	76	17	14		
46	32	113	69	17	12		
41	22	69	37	15	9		
41	19	60	30	13	10		
40	19	56	34	13	9		
39	15	33	31	12	9		
38	33	33	20	12	9		
36	27	31	14	12	5		
36	18	30	24	12	4		
35	34	27	17	11	8		
33	24	13	8	11	5		
31	12	12	9	9	7		
28	24	4	2	9	6		
28	12			9	4		
27	19			9	2		
27	17			8	7		
26	15			8	6		
26	7			8	5		
25	6			8	4		
24	18			8	3		
24	12			8	2		
24	11			7	5		
23	22			7	5		
22	16			7	5		
22	14			7	4		
22	12			7	4		
22	12			7	4		
22	9			7	3		
22	8			6	3		
20	18			6	2		
20	9			5	5		

Table XXXIV (continued)

CD (Cont.)				CD (Cont.)			
Carbonate		**Basalt**		**Carbonate**		**Basalt**	
A(mm)	B(mm)	A(mm)	B(mm)	A(mm)	B(mm)	A(mm)	B(mm)
5	4						
5	2						
5	2						
4	3						
4	3						
3	2						
3	2						
3	2						
2	2						
2	1						
2	1						

Table XXXV: Grain size measurements from station CE.

CE				CE (Cont.)			
Carbonate		**Basalt**		**Carbonate**		**Basalt**	
A(mm)	B(mm)	A(mm)	B(mm)	A(mm)	B(mm)	A(mm)	B(mm)
16	8	23	14				
16	4	12	9				
13	6	11	6				
11	8	8	7				
11	5	8	6				
10	5	8	6				
10	4	8	2				
10	1	7	5				
8	4	6	4				
8	3	6	4				
7	4	6	4				
7	3	6	4				
6	6	6	3				
6	4	2	1				
6	3						
6	2						
6	2						
5	3						
5	2						
5	2						
4	4						
4	3						
4	2						
4	2						
4	2						
3	2						
3	1						
3	1						
2	2						
2	1						

APPENDIX B: ADVECTION DATA FROM WAVE TANK EXPERIMENTS

Advection data were measured for 5 different cube sizes (side lengths of 8 mm, 12 mm, 16 mm, 20 mm, and 24 mm) in aluminum (specific gravity = 2.71) and 3 different specific gravities (1.78, 1.28, and 1.12) with side length of 16 mm. For each cube, bore height and velocity were varied by changing the amount of water impounded behind the dam-break gate; impoundments were varied in 2.5 cm increments from a minumum of 25 cm to a maximum of 42.5 cm or until the particles no longer came to rest on the beach. For all experiments, 2 cm of still water was left in front of the gate, and the particles were placed at the waterline.

In the following tables, advection lengths are reported as the total distance traveled, in centimeters, by each cube. Each table contains data on a different cube type, with each column containing data on a different impoundment, reported in centimeters. The first table contains data on translating the impoundment to bore height and flow velocity.

Table XXXVI: Bore heights and flow velocities created for each impoundment.

Impoundment (cm)	Velocity (cm/s)	Bore height (cm)
25	110	4.6
27.5	120	4.9
30	130	5.3
32.5	140	5.7
35	155	6.5
37.5	165	6.7
40	175	6.8
42.5	185	6.9

Table XXXVII: Advection lengths (in cm) for 8mm aluminum cubes (S.G. = 2.71).

Impoundment (cm)				
25	27.5	30	32.5	35
155	156	184	207	204
165	174	188	210	229
165	179	191	214	232
165	188	200	216	240
167	191	203	218	247
167	195	213	231	248
168	200	213	237	257
173	204	213	237	258
173	204	214	240	260
173	205	230	242	264
174	205	231	243	267
174	206	232	243	268
178	206	233	244	277
180	207	236	245	278
183	207	236	247	280
184	211	236	247	285
185	213	239	253	288
186	213	240	267	289
191	214	242	269	294
193	214	249	270	299
194	215	251	270	301
195	216	254	274	307
196	216	255	277	309
197	223	257	278	318
205	228	271	278	319
207	229		282	319
207	230		286	320
209	235		290	336
224	237		297	340
230	245		306	360

Table XXXVIII: Advection lengths (in cm) for 12 mm aluminum cubes (S.G. = 2.71).

Impoundment (cm)					
25	27.5	30	32.5	35	37.5
129	146	181	188	219	228
133	151	182	191	220	250
134	160	183	196	223	251
135	162	184	211	244	260
140	163	186	217	246	260
141	165	190	220	247	262
146	167	194	223	248	274
147	171	195	228	254	275
149	177	200	230	257	275
150	178	203	230	257	279
153	181	203	233	258	279
155	184	204	235	262	282
156	184	205	237	263	283
157	185	205	238	277	284
158	185	217	240	283	286
159	186	219	244	286	290
161	187	220	246	289	292
164	188	223	246	290	292
165	190	224	248	290	293
166	191	226	248	302	295
166	194	228	250	302	295
167	196	228	253	310	296
175	203	229	255	315	302
178	203	233	257	316	302
180	203	233	259	319	308
181	209	236	259		312
184	212	238	261		312
187	212	238	262		322
194	220	238	267		327
196	225	270	269		339

Table XXXIX: Advection lengths (in cm) for 16 mm aluminum cubes (S.G. = 2.71).

Impoundment (cm)						
25	27.5	30	32.5	35	37.5	40
128	127	166	183	194	193	250
132	128	169	185	212	208	265
135	145	172	195	214	220	265
135	152	176	199	217	231	267
135	153	177	200	220	233	268
138	154	177	203	222	236	269
140	159	179	206	224	237	274
140	159	182	206	228	239	274
142	159	182	208	230	239	278
144	162	182	208	230	243	278
145	164	182	209	231	245	280
146	165	183	215	232	253	283
148	165	184	216	235	255	285
148	166	185	216	236	257	285
148	167	192	218	238	260	285
150	169	194	220	240	265	288
151	169	197	221	247	265	288
153	170	197	223	248	268	295
154	171	198	227	248	278	297
155	173	201	228	249	279	304
155	174	202	230	257	281	305
157	174	203	231	257	282	307
158	175	205	235	258	282	307
158	180	207	237	260	283	310
159	181	216	242	267	289	312
162	183	217	243	273	290	316
163	183	219	250	275	299	316
167	185	224	251	275	308	321
168	187	228	254	287	309	324
192	198	234	258	288	314	360

Table XL: Advection lengths for 20 mm aluminum cubes (S.G. = 2.71).

Impoundment (cm)							
25	27.5	30	32.5	35	37.5	40	42.5
93	126	130	160	188	200	239	280
108	135	141	169	199	218	248	282
117	139	153	177	205	219	251	287
119	139	154	180	207	220	251	288
119	143	161	182	218	230	251	288
120	144	162	184	219	231	259	290
121	144	163	192	224	232	259	293
122	144	166	192	224	232	260	294
122	146	167	194	229	238	260	294
122	147	173	194	229	238	263	296
123	147	173	194	232	244	265	302
123	149	174	194	235	244	265	308
125	150	175	194	237	247	270	308
125	150	177	197	244	247	271	309
128	152	178	198	252	249	274	311
133	153	180	198		250	274	313
133	153	182	200		253	275	314
134	153	184	202		255	277	315
135	153	184	204		257	284	315
136	154	185	205		258	284	316
137	154	187	207		260	286	317
138	155	188	209		263	290	321
139	157	189	209		263	293	322
140	164	190	215		267	295	332
143	169	191	215		268	302	334
147	171	194	215		268	304	341
149	172	194	218		274	305	
150	178	196	220		274	308	
158	181	196	225		278	316	
170	191	207	232		282	320	

Table XLI: Advection lengths (in cm) for 24 mm aluminum cubes (S.G. = 2.71).

Impoundment (cm)							
25	27.5	30	32.5	35	37.5	40	42.5
82	95	121	129	165	193	209	253
88	103	123	130	173	195	209	254
94	107	124	148	173	201	209	260
95	122	128	156	174	203	211	265
97	123	129	156	183	205	214	266
98	126	137	159	185	209	217	282
99	129	140	159	185	211	219	282
102	131	141	159	186	213	220	288
105	132	143	163	187	213	222	290
105	133	147	163	189	217	224	293
109	135	148	163	190	217	226	294
110	135	154	164	193	218	228	295
110	135	155	168	193	221	229	299
114	137	157	169	195	228	233	307
114	137	158	171	196	228	234	310
114	138	159	171	197	230	239	310
114	138	160	177	199	230	240	312
117	139	162	177	200	232	246	312
118	140	163	178	203	234	247	313
119	141	165	178	204	235	257	330
120	142	165	180	204	236	257	
120	143	165	180	205	237	265	
123	143	166	182	206	240	267	
123	143	167	184	208	240	271	
125	148	175	187	212	242	274	
126	157	175	203	215	243	274	
126	157	179	214	216	244	281	
129	157	182	215	222	245	282	
131	160	183	215	226	247	298	
138	164	187	223	227	249	299	

Table XLII: Advection lengths (in cm) for 16 mm magnesium cubes (S.G. = 1.78).

Impoundment (cm)				
25	27.5	30	32.5	35
170	188	233	249	270
174	200	233	254	277
177	200	237	255	278
178	203	240	257	278
181	205	241	261	282
183	209	242	261	283
183	210	243	262	290
184	211	243	266	290
186	213	244	268	292
189	214	246	268	294
189	222	249	269	295
189	223	253	270	295
192	225	254	273	296
192	225	255	275	297
193	225	256	277	298
193	226	257	277	299
194	226	258	278	303
195	228	260	279	303
197	229	263	280	306
197	231	263	281	308
198	231	264	282	308
200	231	266	284	312
202	232	266	285	313
203	232	267	286	314
203	233	269	287	315
204	234	278	294	322
205	236	282	298	328
210	237	283	299	329
217	245	284	302	332
220	249	285	307	345

Table XLIII: Advection lengths for 16 mm lignum vitae cubes (S.G. = 1.28).

Impoundment (cm)			
25	27.5	30	32.5
215	227	263	283
221	242	270	295
222	250	271	297
223	252	280	298
224	253	282	299
225	253	283	299
227	254	284	302
227	255	284	306
227	256	286	307
229	256	288	309
231	257	288	309
231	259	289	314
232	259	294	316
233	260	296	317
234	261	296	319
235	262	297	320
235	263	298	321
235	264	298	322
236	265	298	323
237	266	298	323
237	266	299	323
238	267	300	324
238	267	301	324
238	269	301	325
239	270	301	329
239	270	301	331
239	271	302	333
240	272	304	334
241	273	305	336
251	273	309	337

Table XLIV: Advection lengths (in cm) for 16 mm acrylic cubes (S.G. = 1.12).

Impoundment (cm)		
25	27.5	30
206	241	271
220	269	271
228	269	280
234	269	286
238	270	291
239	271	293
239	271	294
240	272	296
241	272	297
241	273	298
242	274	299
242	275	299
242	276	300
243	276	300
243	277	300
243	277	300
244	278	300
246	278	300
246	278	300
247	278	301
247	279	301
248	279	303
248	279	304
249	279	304
249	281	304
250	281	305
251	282	308
252	284	309
253	284	311
253	285	

APPENDIX C: MODERN TSUNAMI PARAMETER ESTIMATES

The particles listed in the following table were used for comparing the experimental results from Chapter 2 to modern tsunamis.

Table XLV. Particle advection data used in comparing experimental results to modern tsunami deposits.

Particle Type	Advection Distance (m)	Median Grain Size (mm)	Particle Density (g/cm^3)	Estimated Flow Depth (m)	Froude Number	Estimated Flow Velocity (m/s)
Irian Jaya						
coral	126	23	2.21	1.55	1	3.9
coral	130	20	2.21	1.55	1	3.9
coral	135	22	2.21	1.55	1	3.9
coral	140	19	2.21	1.55	1	3.9
Nicaragua						
beach rock	147	130	2.9	2.2	1	4.65
brick	88	400	1.9	2.2	1	4.65
beach rock	150	140	2.9	2.2	1	4.65
brick	182	220	1.9	2.2	1	4.65
PNG						
coral	100	750	2.0	3.4	1	5.77
coral	110	500	2.0	3.4	1	5.77

VITA

Andrew Lathrop Moore

University of Washington

1999

M.S., 1994, Department of Geological Sciences, University of Washington, "Evidence for a tsunami in Puget Sound about 1000 years ago"

B.A., 1990, Department of Geology, Carleton College.

IMAGE EVALUATION
TEST TARGET (QA-3)

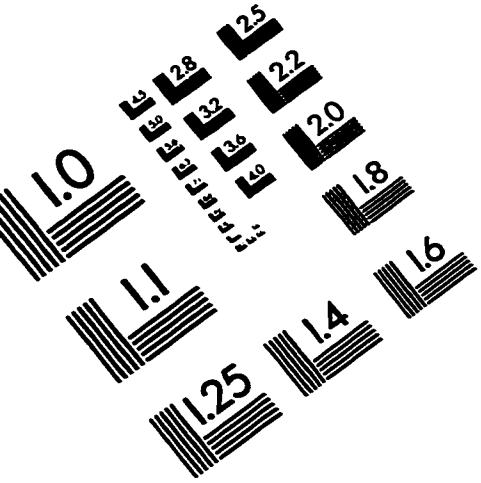

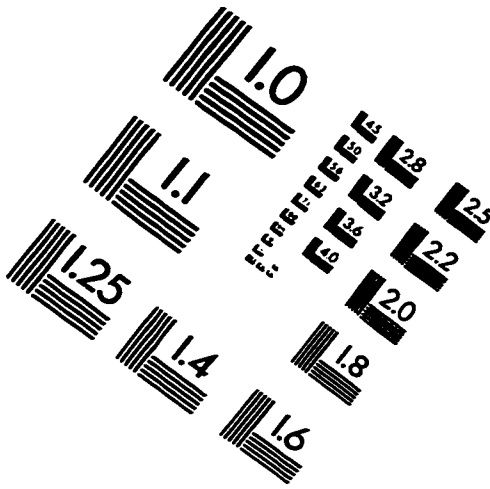

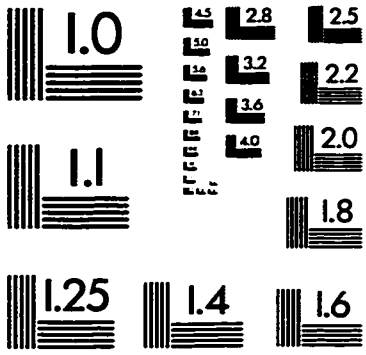

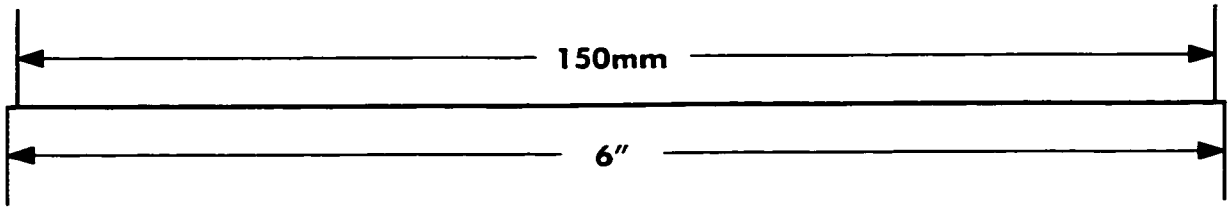

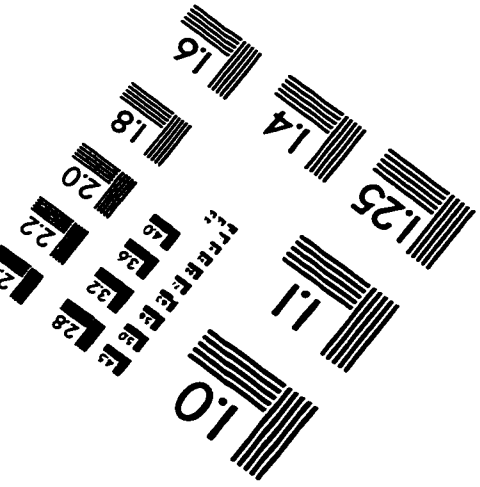

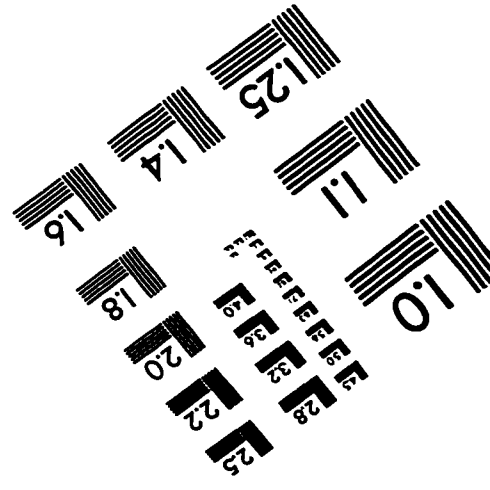

APPLIED IMAGE . Inc
1653 East Main Street
Rochester, NY 14609 USA
Phone: 716/482-0300
Fax: 716/288-5989